UC Santa Cruz

UC Santa Cruz Electronic Theses and Dissertations

Title

TRANSITION METAL BASED ELECTROCATALYSTS FOR WATER SPLITTING

Permalink

https://escholarship.org/uc/item/98w4h8bn

Author

Kou, Tianyi

Publication Date

2019

Peer reviewed|Thesis/dissertation

eScholarship.org Powered by the California Digital Library
University of California

UNIVERSITY OF CALIFORNIA
SANTA CRUZ

TRANSITION METAL BASED ELECTROCATALYSTS FOR WATER SPLITTING

A dissertation submitted in partial satisfaction
of the requirement for the degree of

DOCTOR OF PHILOSOPHY

in

CHEMISTRY

by

Tianyi Kou

September 2019

The Dissertation of Tianyi Kou is approved:

_____
Professor Yat Li, chair

_____
Professor Jin Zhong Zhang

_____
Professor Ilan Benjamin

_____
Quentin Williams
Acting Vice Provost and Dean of Graduate Studies

Copyright © by

Tianyi Kou

2019

Table of Contents

List of Figures

Chapter 1

Chapter 2

Figure 2.6 (a) Surface energy of possible termination of the (100) surface as a function of S chemical potential $\Delta\mu_S$. (b, c) Side and top views of the most stable termination of the (100) facet of Ni_3S_2 (grey sphere represents Ni and yellow sphere represents S), respectively.

Figure 2.7 (a) HER polarization curves of the pristine (black) and N doped Ni_3S_2/NF (red) collected in 1 M KOH at a scan rate of 5 mV s^{-1} (dashed lines highlight the potential at 10 mA cm^{-2}). (b) Difference of anodic current and cathodic current is plotted as a function of scan rate. (c) Tafel plots of the pristine and N doped Ni_3S_2/NF. (d) Mass activity (normalized to Ni_3S_2 mass loading) and (e) Turnover frequency of the pristine and N doped Ni_3S_2/NF are plotted as a function of applied potential. (f) Electrochemical impedance spectra collected at -0.159 V vs. RHE with frequencies from 100 kHz to 1 Hz and amplitude of 5 mV. Dots and lines represent the experimental and simulated results, respectively.

Figure 2.8 (a) XRD patterns of the NH_3 treated Ni_3S_2/NF. (b) Magnified spectrum highlighted by the dashed box in (a).

Figure 2.9. Core level (a) Ni 2p, (b) S 2p and (c) N 1s XPS spectra collected for N doped Ni_3S_2/NF. The black solid curves are the experimental results, which can be deconvoluted into synthetic peaks (dashed lines). The red solid curves are the summation of the synthetic peaks.

Figure 2.10 (a) TEM image collected from a N doped Ni_3S_2 nanosheet. Scale bar is 20 nm. Inset: selected area electron diffraction pattern. (b) HAADF-STEM image of a N doped Ni_3S_2 nanosheet and corresponding elemental mapping of Ni (L-edge), S (L-edge) and N (K-edge). Scale bar is 100 nm. (c, d) TEM images and corresponding Fast

Fourier Transform (FFT) images created from the regions highlighted by the dashed boxes of a N doped Ni_3S_2 nanosheet.

Figure 2.11 (a) Surface energy of possible terminations of the (-111) surface as a function of S chemical potential $\Delta\mu_S$. (b, c) Side and top views of the most stable termination of the (-111) facet of Ni_3S_2 (grey sphere represents Ni and yellow sphere represents S), respectively.

Figure 2.12 HER polarization curves collected from three different N doped Ni_3S_2 samples in 1 M KOH at a scan rate of 5 mV s^{-1}. Dashed lines highlight the potential at 10 mA/cm^2.

Figure 2.13 Polarization curves of Ni_3S_2 samples treated in different conditions collected in 1.0 M KOH at the scan rate of 5 mV s^{-1}.

Figure 2.14 (a) HER polarization curves collected from two different bare Ni foams in 1 M KOH with a scan rate of 5 mV s^{-1}. (b) HER polarization curves of a pristine and N doped Ni foam collected in 1 M KOH with a scan rate of 5 mV s^{-1} (dashed lines highlight the potential at 10 mA/cm^2).

Figure 2.15 The HER polarization curves collected from pristine and N doped Ni_3S_2 samples in 1 M KOH with a scan rate of 5 mV s^{-1} (dashed lines highlight the potential at 10 mA/cm^2). The currents are normalized to the electrochemical surface area.

Figure 2.16 Polarization curves of Ni_3S_2/NF and N doped Ni_3S_2/NF before and after 10000 cyclic voltammetry scans at 100 mV s^{-1}.

Figure 2.17 Current-time curve of N doped Ni_3S_2/NF collected at -0.28 V vs. RHE. The arrow highlights the time of replacing electrolyte.

HR-TEM image collected at the edge of the nanoparticle in (f). (h) High-angle annular dark field (HAADF)-TEM image of a Ni core/NiO shell particle and the corresponding EELS elemental mapping of Ni, O and C (scale bars are 20 nm).

Figure 3.3 SEM images of $NiC_2O_4 \cdot 2H_2O$ grown on NF. **c**, XRD pattern of $NiC_2O_4 \cdot 2H_2O$ powder.

Figure 3.4 (a) Thermogravimetric analysis of the $NiC_2O_4 \cdot 2H_2O$ in argon atmosphere with a ramping rate of 10 ^oC/min. (b) XRD pattern obtained from the C-$Ni_{1-x}O$ powder.

Figure 3.5 (a) Ni 2p, O 1s, and C 1s XPS spectra collected from C-$Ni_{1-x}O$ particles. The black curves are the experimental data. The red curves are the summation of the deconvoluted peaks (shaded regions). (b) O K-edge and C K-edge XANES spectra of C-$Ni_{1-x}O$ grown on NF (red curve) and NF (grey curve).

Figure 3.6 (a-b) Ni 2p and C 1s XPS of the annealed $NiC_2O_4 \cdot 2H_2O$ after argon plasma etching.

Figure 3.7 The structure of (100) surface of NiO. The vacuum's direction is given in the figure. The bottom layer is fixed (the color coding for different atoms is consistent for the whole paper).

Figure 3.8 Ni terminated (111) surface of NiO. The vacuum's direction is given in the figure.

Figure 3.9 The surface phase diagram for (111) surface of NiO.

Figure 3.10 (a-b) o-surface and C-surface structures with numbers labeling different Ni sites. (c-d) PDOS plots of the Ni 3d and O 2p orbitals of the first three layers from the o-surface and C-surface. (e-f) PDOS plots of the 3d orbitals of Ni on o-surface (Ni

#1) and C-surface (Ni #1'), respectively. (g) charge density mappings of the top layer Ni (#1 and 1') on o-surface (upper) and C-surface (bottom).

Figure 3.11 Correlation between Bader charge, number of Ni that H binds to and Gibbs free energy change of H adsorption (ΔG_H). The 5 points represent 5 different H adsorption sites on o-surface and C-surface.

Figure 3.12 (a) HER polarization curves obtained from NF, C-$Ni_{1-x}O$ and Pt/C in 1.0 M KOH saturated with nitrogen at a scan rate of 1 mV/s. (b) Polarization curves of NF and C-$Ni_{1-x}O$ with current normalized to ECSA. (c) Tafel plots of the NF, C-$Ni_{1-x}O$ and Pt/C. (d) Electrochemical impedance spectra of the NF and C-$Ni_{1-x}O$ measured at the potential of -0.15 V vs RHE, with frequency ranging from 100 kHz to 1 Hz and an amplitude of 5 mV. Dots and solid lines are the experimental data and simulated results based on the equivalent circuit illustrated in the inset, respectively. (e) The comparison of the overpotential at 10 mA/cm^2 and Tafel slopes of C-$Ni_{1-x}O$ with the reported state-of-the-art Ni and NiO based HER catalysts, including NiO/Ni-CNT, Ni nanosheets (NSs), NiO_x@Bamboo-like CNTs (BCNTs), NiOx nanorods (NRs), and Ni/NiO NSs. (f) Polarization curves of the C-$Ni_{1-x}O$ collected before and after 10000 cycles. Inset figure shows the polarization curves with current normalized to ECSA. All of the data here are *iR* corrected.

Figure 3.13 Polarization curves collected from four different C-$Ni_{1-x}O$ samples measured in the same condition at the scan rate of 1 mV/s in nitrogen saturated 1.0 M KOH (*iR* corrected). Inset is the overpotential at the j_{geo}=10 mA/cm^2 of the four samples.

Figure 3.14 The difference of the anodic and cathodic current density difference of C-$Ni_{1-x}O$ and NF versus scan rate.

Figure 4.4 (a) Ni K-edge XANES spectra of Ni-Fe-2 and Ni foil. (b) Fe K-edge XANES spectra of Ni-Fe-2 and Fe foil. (c) Magnitude of the Fourier-transformed Ni K-edge EXAFS spectra.

Figure 4.5 (a) OER polarization curves obtained from Ni-Fe-0, Ni-Fe-1, Ni-Fe-2, Ni-Fe-3 and Ni foam in 1.0 M KOH solution at a scan rate of 1 mV/s. Dashed line corresponding to 10 mA/cm^2. (b) Tafel plots of the samples. The values are the slope of each curves. (c) Plots of difference of anodic and cathodic current density as a function of scan rate. (d) Electrochemical impedance spectra of the samples collected at the overpotential of 291 mV, with frequency from 100 kHz to 1 Hz and amplitude of 5 mV. Dots and lines represent the experimental and simulated data, respectively. (e) Polarization curves of the samples with current density normalized to ECSA. (f) 3D histogram compares the ECSA current densities and overpotentials at 10 mA/cm^2 of Fe-doped β-$Ni(OH)_2$ samples with other state-of-the-art OER catalysts including $NiCoO_2$, $NiFeO_x$, $CoFe_2O_4$, $Na_{0.08}Ni_{0.9}Fe_{0.1}O_2$, RuO_2.

Figure 4.6 Polarization curves collected for four different Ni-Fe-2 samples at the scan rate of 1 mV/s in O_2 saturated 1.0 M KOH (*iR* corrected).

Figure 4.7 Polarization curves of Ni-Fe-2 samples obtained before and after testing for 10000 cycles at the scan rate of 1 mV/s in O_2 saturated 1.0 M KOH (*iR* corrected).

List of Tables

Chapter 2

Abstract

Transition Metal Based Electrocatalysts for Water Splitting

by

Tianyi Kou

Electrochemical water splitting is a catalytic process in which water molecule can be catalytically reduced to dihydrogen in cathode and oxidized to oxygen molecule in anode. The electrical energy that is used for water splitting can be renewable when the energy source is sunlight, geothermal heat, tide, etc., and the hydrogen gas can thus be generated sustainably. Nonetheless, the hydrogen produced through electrochemical water splitting is less than 10% of the total amount.

The top limitation of its wide applications is the low activity of catalysts in both cathodic reaction (hydrogen evolution reaction, HER) and anodic reaction (oxygen evolution reaction, OER). The dissertation covers heteroatoms doping strategy in activating HER and OER catalysts that I have developed in my PhD study. For instance, N doping has been found to create new facets and active sites of Ni_3S_2 that are able to improve the hydrogen adsorption. As a result, the overpotential of Ni_3S_2 can be decreased from 240 mV to 155 mV at 10 mA/cm^2, while the TOF of N doped Ni_3S_2 can be increased as much as 2 times of the pristine Ni_3S_2. A carbon doping strategy was adopted to activate NiO water-alkali HER catalyst. Combined our experimental and theoreticality study, carbon doping has created under-coordinated Ni sites that are favorable for hydrogen adsorption. Meanwhile, the carbon dopant also serves as the "hot-spot" in water dissociation that contributes to the improved kinetics of HER. The carbon doped NiO showed an ultralow overpotential of 29 mV at 10 mA/cm^2, even

comparable with the benchmark Pt/C catalysts. On the other hand, Fe-doped β-$Ni(OH)_2$ nanosheets supported on Ni foam were developed for OER and able to achieve a low overpotential of 219 mV at geometric area current density of 10 mA cm^{-2}, and a high electrochemical surface area current density of 6.25 mA cm^{-2} at the overpotential of 300 mV. This high intrinsic catalytic activity should be due to the strong electron-withdrawing ability of Fe dopant that makes the adjacent Ni active in OER, as well as the unique mixed amorphous/crystalline heterogeneous structure as preferential adsorption sites towards OER intermediates.

Dedication

DEDICATED

TO

MY PARENTS, SISTER AND BROTHER-IN-LAW

Acknowledgements

Many years ago, a famous Chinese entrepreneur who succeeded twice in climbing the Mount Everest in his 50s gave a speech in a TV show about his study experience in Harvard University. He compared his study there in his 60s to another climbing Mount Everest. The only difference between the two is that there is no factual altitude in the former case. Tremendous difficulties were overwhelming at the beginning of my doctoral study and I once questioned myself if I can make it to 'climb' this invisible Mount Everest. At the most difficult time in my doctoral study, my supervisor Professor Yat Li provided his strong and continuous support for my research. His great personality has made me enjoy each project I worked with him. I would like to express my deepest appreciation for Yat 's excellent scientific training, patient instructions, and supportive attitude to me. Without these, it will not be possible for me to complete my doctoral degree. I also would like to show my greatest appreciation to Yat's wife, Dr. Fang Qian. Fang's great professionalism has taught me a lot beyond research. The precious experience will be my lifelong treasure.

I would like to thank my dissertation reading committee members, Professor Ilan Benjamin, and Professor Jin Zhong Zhang who offered their generous help in my study. Their constructive suggestions and instructions have helped me a lot in doing high quality research. I also feel greatly appreciated for the scientist at Livermore national laboratory, Dr. Marcus Andre Worsley, who served as my committee member during my oral qualifying exam and gave me helpful suggestions in my research.

My sincerely appreciation will also be given to Professor Zhonghua Zhang who was my supervisor during my master's degree study in Shandong University. Even though I graduated and left Shandong University five years ago, Professor Zhang has been keeping giving his consistent support for my study and life. His life philosophy encouraged me to overcome difficulties in my doctoral study and keep the most positive attitude towards failures and frustrations. I would also thank Professor Jennifer Lu at University of California, Merced. Her generous help and great personality have made the collaborative project a success. The days I spent in UC Merced is a great experience and I also thank Professor's Lu for offering so many free and delicious meals there.

I greatly enjoyed the fun time with my friends Miguel Nicolas Pinto, Evan Vickers, and Michael Roders. I will not forget the times I spent with Miguel and Evan travelling in Boston, the music events with Miguel in southern California, little adventure of climbing mountains in a middle night at Yosemite with Evan Vickers, and the beer, gin and wine I enjoyed with all of my friends. Thanks to my current and former lab mates and I appreciate all of the help I have got from you all: Professor Gongming Wang, Professor Xihong Lu, Dr. Hanyu Wang, Professor Teng Zhai, Dr. Tianyu Liu, Dr. Yi Yang, Shanwen Wang, Mingpeng Chen, Megan Freyman, Dun Lin, Bin Yao, Dr. Jing Zhang. I also thank the visiting scholars for their instructions in my study and I will cherish the memory with you all: Professor Changjin Tang, Professor Yang Yang, Dr. Yuhang Wang, Dr. Mingyang Li, Dr. Yu Song, Dr. Huarong Peng, Cheng Cheng, Dr. Xiaoli Fan. Thank my other department faculty and friends: Dr. Randa Roland, Professor Yuan Ping, Tyler Smart, Dr. Peiguang Hu, Dr. Limei Chen, Dr. Jesse Lee Hauser, Jeremy Barnett, Dr. Yi Peng, Bingzhang Lu, etc. for your help in my research.

Last but not least, I would thank my parents, sister and brother-in-law who have supported my life and schooling here in United States. My appreciation to you all is beyond my words. Your love and support are always the most important motivations for me to make progress in my research.

The text of this dissertation includes reprints of the following previously published materials:

1. **Kou, T.**; Smart, T.; Yao, B.; Chen, I.; Thota, D.; Ping, Y.; Li, Y. Theoretical and experimental insight into the effect of nitrogen doping on hydrogen evolution activity of Ni_3S_2 in alkaline medium. *Adv. Energy. Mater.,* **2018**, *8*, 1703538

2. **Kou, T.**; Chen, M.; Wu, F.; Smart, T.; Wang, S.; Wu, Y.; Li, S., Lall, S., Zhang, Z.; Liu, Y.; Guo, J.; Wang, G.; Ping, Y.; Li, Y. Carbon Doping Switching on the Hydrogen Adsorption Activity of NiO for Hydrogen Evolution Reaction. *Submitted*

3. **Kou, T.**; Wang, S.; Hauser, J.; Chen, M.; Oliver, S.; Ye. Y.; Guo, J.; Li, Y. Ni foam-supported Fe-doped β-$Ni(OH)_2$ nanosheets show ultralow overpotential for oxygen evolution reaction. *ACS Energy Lett.*, **2019**, *4*, 622.

Chapter 1

Introduction of Electrochemical Water Splitting

Abstract

The high gravimetry energy density and zero-carbon emission have made hydrogen gas one of the most appealing fuel in the field of energy storage and conversion. However, there is no hydrogen gas that naturally exists in the world. Producing hydrogen gas is therefore important. Currently there are two strategies developed for industrial hydrogen generation: conventional natural gas reforming and electrochemical water splitting. Even though the former technology is well developed and dominates the hydrogen generation market, it is fossil fuel dependent and the whole process releases pollutants and greenhouse gases. In contrast, electrochemical water splitting can avoid these environmental issues as its source of hydrogen is only water. In addition, the electrical energy can be converted from renewable energy sources such as solar or wind energy. Because of these merits, it is quite urgent and necessary to study and develop electrochemical water splitting. In this chapter, the fundamentals of the electrochemical water splitting including reaction mechanisms, evaluation methods, overview of the catalysts of both half reaction (i.e. hydrogen evolution reaction, oxygen evolution reaction) are introduced.

1.1 Background

It is well-recognized that fuels are indispensable for the continuing functions and prosperity of human society and civilizations. Conventionally the fuels people refer to are fossil fuels that include coal, petroleum and natural gas. With the worldwide population explosion and economic development in the last century, the increased

energy demand has largely stimulated the exploitation of fossil fuels. It has been estimated in 2010, a huge amount of energy of 12717 million tons of oil equivalent (MTOE) was supplied globally, while 80% of the energy demand was satisfied by fossil fuels.[1] Unfortunately, fossil fuels are regarded as non-renewable as their formation can take up to millions of years. The reserve of fossil fuels in the earth is thus highly limited and unable to sustain the global economy. In addition, the usage of fossil fuels usually generates considerable amount of pollutants and greenhouse gases, which poses a significant threat to the sustainability of human society. In this regard, renewable fuels such as hydrogen gas, have been gained increased attentions due to their low to zero carbon and pollutant emission into the environment, and high energy density.

The most typical characteristics of renewable fuels is their chemical bond energy is converted from renewable energy source such as solar and wind energy, while the conversion pathways can be different. Some of the renewable fuels such as methanol, ethanol, etc., are derived from biological process such as photosynthesis or fermentation in plants by using the solar energy, which is helpful in reducing carbon emission of modern economy.[2] However, the extraction of biofuels from biomass is still not cost-competitive compared to the conventional fossil fuels.[3]

As an alternative strategy, electrocatalysis, a redox catalytic reaction, has provided an important way to generate renewable fuels.[4] Specifically, the electrochemical redox reactions occurring at the interface of electrocatalysts and electrolyte are directly in charge of the harvesting of fuels. The rate of the fuel generation in the electrochemical redox reactions are usually dependent on the quantity of the electrical energy consumed in electrocatalysis. The electrical energy that drives the fuel generation in

electrocatalysis can be obtained from the conversion of solar and wind energy which makes the whole process environmentally friendly and sustainable. There are different kinds of electrocatalysis that can realize the production of renewable fuels such as hydrogen, formic and ethanol. Among them one representative example is electrochemical water splitting that generates hydrogen gas.

1.2 Electrochemical Water Splitting

It has been reported that more than 44.5 million tons of the hydrogen gas is generated annually in the world, while about 90% of the hydrogen gas is produced through a well-developed technology, i.e., natural gas reforming.[5] Specifically, both steam-methane reforming reaction ($CH_4 + H_2O \rightarrow CO + 3H_2$) and water-gas shift reaction ($CO + H_2O \rightarrow CO_2 + H_2$) are involved in this process. It is clear to see from the reaction equations that the production of hydrogen gas through natural gas reforming strategy is largely dependent on the non-renewable fossil fuels, which unavoidably results in the release of air-pollutants and greenhouse gases.

Alternatively, water electrolysis (i.e. electrochemical water splitting) provides a sustainable way to realize hydrogen generation because of the following reasons. The intermittence and uneven spatial distribution of the renewable energy resources such sunlight, wind and geothermal heat restrict their direct applications.[6] Storing renewable energy in the chemical bonds of transportable and high gravimetric energy density carriers, such as hydrogen, is a reasonable and practical strategy to handle this limitation. Driven by the renewable electricity, electrochemical water splitting that generates hydrogen fuels bridges the conversion gap between renewable energy and hydrogen resources. The extra bonus of zero-carbon emission and pollution-free also

makes electrochemical water splitting a particularly promising strategy in hydrogen production. Based on the pH of electrolytes, electrochemical water splitting can be divided into two types: proton exchange membrane (PEM) water splitting and alkaline water splitting. PEM water splitting is a well-developed hydrogen generation method in industry and the advantages such as rich proton environment facilitating hydrogen adsorption and high energy efficiency (>80%) have attracted much attention.[7] However, usually only the noble metals are involved in PEM water splitting as most of the inexpensive transition metals are not stable in acidic media.[8] This largely increases the usage costs of PEM water splitting devices and has been a long-standing limitation. In contrast, alkaline media is milder toward inexpensive transition metals and thus is promising to decrease the costs of the water splitting devices. Albeit the advantages, there are also many challenges in catalysts design to tackle the sluggish water splitting kinetics in alkaline media. In the following sections and chapters, both half reactions of water splitting in alkaline media, and catalysts we developed will be primarily discussed.

1.2.1 Hydrogen Evolution Reaction (HER)

Hydrogen evolution reaction (HER) is one of the critical half reactions in electrochemical water splitting, as hydrogen gas is directly generated in this half reaction. Developing active and robust HER catalysts is necessary to improve hydrogen production kinetics while many challenges are present in creating these desired active centers. In this section, the fundamentals of HER including mechanism, evaluation methods and some advanced HER catalysts will be discussed.

1.2.1.1 The Mechanism of HER

HER is a typical two-electron transfer reaction and the reaction equations can be different based on the media.[5] Specifically, in acid media, it is the reduction of protons in HER ($2H^+ + 2e^- \rightarrow H_2$), while in alkaline media it includes the dissociation of water molecule ($2H_2O + 2e^- \rightarrow 2OH^- + H_2$). Even though three steps (i.e. Volmer, Heyrovsky, and Tafel step) are consistently involved in acid and alkaline media, the corresponding elementary reaction pathways are different. For example, in acid media, the three steps are listed as follows:

$$H^+ + * + e^- \rightarrow H^* \text{ (Volmer step)}$$

$$H^* + H^+ + e^- \rightarrow H_2 + * \text{ (Heyrovsky step)}$$

$$2H^* \rightarrow H_2 + * \text{ (Tafel step)}$$

where * represents the surface (or active center) of the HER catalysts.[9] The protons in acid media can be adsorbed on the surface of the catalysts followed by the single electron transfer reduction (Volmer step). The as-formed hydrogen atom (H*) has the chance to combine with proton that is reduced with one electron, resulting in the generation of one hydrogen molecule (H_2) and a refreshed active center (Heyrovsky step). Alternatively, the H* generated in Volmer step can also combine with each other to produce H_2, with newly refreshed active center (Tafel step). However, due to the low concentration of protons, the reaction shows different pathway profile in alkaline media. The specific elementary reactions are shown below:

$$H_2O + * + e^- \rightarrow H^* + OH^- \text{ (Volmer step)}$$

$$H_2O + H^* + e^- \rightarrow H_2 + OH^- \text{ (Heyrovsky step)}$$

$$2H^* \rightarrow H_2 + * \text{ (Tafel step)}$$

It has to be noted that both Volmer and Heyrovsky step in alkaline media shows a big difference with that in acid.[9] Due to the low availability of protons in alkaline electrolyte, hydrogen atom in H_2 has to be sourced from water molecules which are shown in Volmer and Heyrovsky steps. In detail, the strong covalent bond of H-OH has to be cleaved, which takes extra energy of about 498.7 kJ/mol.[10] The cleavage of H-OH (i.e. dissociation of water molecules) thus makes the HER in alkaline media more sluggish than that in acid electrolyte. Owing to the necessity of developing water-alkali HER, it is critical to further understand the mechanism of HER in this type of electrolyte.

1.2.1.2 Evaluation of HER Electrocatalyst

Under the standard conditions (room temperature of 25 °C, and 1 atm), the Nernst equation corresponding to HER (taking the HER in acid for an example) should be (eq.1.1):

$$E = E^0_{(H^+/H_2)} - \frac{R\,T}{2\,F} \times \ln\left[P_{H_2}/(P^0 \alpha^2_{H^+})\right]$$

$$= -0.059 \times \text{pH V vs. NHE}$$

$$= 0 \text{ V vs. RHE}$$

where E is the Nernstian potential of HER in thermodynamic equilibrium condition, $E^0_{(H^+/H_2)}$ is the standard proton reduction potential with a value of 0, R is the gas constant, T is the temperature of 298 K, n is number of mole of electron transferred when generating 0.5 mole of H_2, F is the faraday constant, α_{H^+} is effective concentration of H^+, and P_{H_2} is the pressure (1 atm in the standard condition).[11] It can be seen from the derivation of the Nernst equation in which the E can change by about

59 mV with each unit change of pH value, when E is normalized to NHE. Apparently, this brings troubles for comparison when measuring the HER in the electrolytes with different pH values. To address this problem, the potential is usually against reversible hydrogen electrode (RHE) which cancels out the dependence of E on pH. In other words, ideally the Nernstian potential of HER at thermodynamic equilibrium condition is always 0 no matter what the pH value is. In reality, the HER is barely started at the potential of 0 vs. RHE, instead a more negative potential is generally applied to drive the initiation of HER. The difference between the potential of HER and 0 V vs. RHE is defined as overpotential (i.e. η).[5] Overpotential represents a low energy efficiency power to gas, and thus is one important parameter to evaluate the performance of HER catalyst. The presence is due to multiple reasons, including the intrinsic HER energy barrier, the electrical resistance (including solution and catalyst intrinsic resistance), and diffusion resistance of the electrolyte.[11] Suppressing the HER energy barrier and decreasing the electrical resistance of the HER catalyst require reasonable catalyst design.

Butler-Volmer equation is generally used to depict the reaction kinetics of HER (eq. 1.2):

$$j=j_0\{-e^{-\frac{\alpha nF\eta}{RT}}+e^{(1-\alpha)nF\eta/RT}\}$$

where j represents the current density, n is the number of electrons transferred during HER with a value of 1, α is the symmetry coefficient, and j_0 is the exchange current density.[12] The exchange current density is another important parameter which usually describes the reaction rate under the equilibrium conditions.

When the overpotential is small enough, the Butler-Volmer equation can be simplified to the equation as follows (eq. 1.3):

$$\eta = \frac{-2.3\ RT}{\alpha nF} \log j_0 + \frac{2.3\ RT}{\alpha nF} \log j = a + b \log j$$

where the equation (9) clearly proves the linear relationship between η and logj. The slope (b) of equation (9) is called Tafel slope, which is used to find out the rate-limiting-step of HER and give the possible mechanism insights. Tafel slope is thus a critical parameter in HER and usually discussed together with overpotential to evaluate the performance of a catalyst. Based on the different elementary step, there are different Tafel slopes accordingly. Taking the HER in acid media as an example, Tafel slope is (eq. 1.4):

$$b = \frac{2.3\ RT}{\alpha F}$$

where α is 0.5. If plugging in all of the constant (at the temperature of 298 K), the Tafel slope for the Volmer step is about 118 mV/dec. When the reaction is limiting by the Heyrovsky step (i.e. the surface coverage by adsorbed hydrogen atom is low), the Tafel slope will become (eq. 1.5):

$$b = \frac{2.3\ RT}{(1+\alpha)F}$$

The corresponding slope for the Heyrovsky step is 39 mV/dec. When the reaction rate is controlled by Tafel slope (i.e. the surface coverage of the adsorbed hydrogen atom is high), the equation of the Tafel slope is (eq. 1.6):

$$b = \frac{2.3\ RT}{2F}$$

and the slope value will be 29 mV/dec. Generally, a smaller Tafel slope indicates a higher performance.

It can be seen from the discussions on the elementary reactions and Tafel slope that the hydrogen adsorption is important in HER. Either too strong or too weak hydrogen adsorption will negatively impact the subsequent hydrogen gas molecule formation. In fact, based on Sabatier principle, the chemisorption of the intermediate on the active site of the catalyst should be optimal in order to obtain a maximum reaction rate. The trending is thus shaped like a volcano and usually called volcano plot. On the basis of earlier Sabatier principle, Parson further developed the volcano plot HER, and he found the maximum value of exchange current density can only be achieved when the corresponding change of Gibbs free energy of hydrogen adsorption is close to 0 (i.e. ΔG).[13] Norskov *et al*. also computed the detailed change of Gibbs free energy over a series of metallic HER catalysts (Figure 1.1).[14] Similarly, they found the exchange current density is also present in the shape of volcano vs. change of Gibbs free energy through their density of functional theory computations. It is thus that the free energy of hydrogen adsorption is used as an important descriptor in HER, especially in acidic media. However, the situation becomes much more complicated in alkaline electrolyte as there is not enough protons available in it. The adsorbed hydrogen atoms in alkaline media are sourced from water molecules which dissociate on the water adsorption site of the HER catalyst. The dissociation of the water molecules take place when enough energy is provided to overcome the strong covalent bond of H-OH. This process has largely affected the HER kinetics in alkaline media. Therefore, the descriptor of HER in alkaline media should not limited to the free energy

of hydrogen adsorption. Instead, the water dissociation kinetics should be considered as well when it comes to the water-alkali HER.

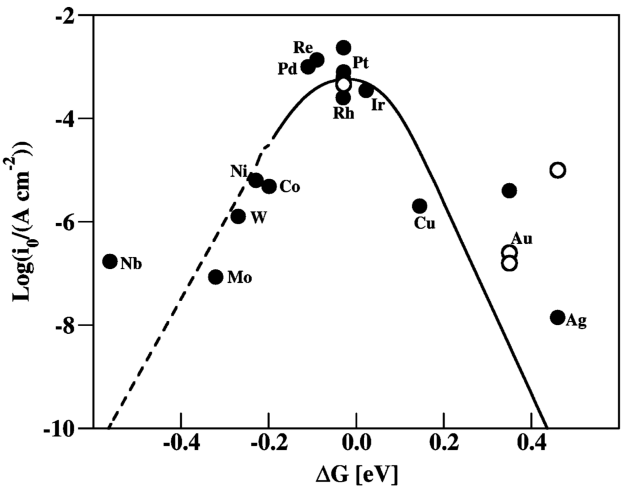

Figure 1.1 The volcano plot showing the trending of different metallic HER catalysts versus the change of free Gibbs energy of H adsorption (filled and open circles data are obtained from (111) facet and polycrystalline, respectively).[14]

1.2.1.3 Platinum vs. Economic HER Electrocatalyst

Platinum group metals (PGMs) have been long time regarded as the benchmark HER catalyst due to their close to thermal neutral H adsorption free energy.[14] Even though the HER kinetics are much slowed down in alkaline electrolyte due to the limitation of the water dissociation, PGMs are still the best HER catalyst. However, the high costs of the PGMs largely restrict the extensive applications of them as water-alkali HER catalysts. Reducing the loading of PGMs or developing inexpensive catalysts should be reasonable to handle this limitation. For example, Tan et al. synthesized single atom Pt on nanoporous $Co_{0.85}Se$ catalysts which exhibited almost an onset overpotential of 0 and a very low Tafel slope of about 35 mV/dec.[15] In addition,

the ultralow loading of the Pt has largely exposed their active sites and increased the utilization efficiency of the Pt atoms. Because of this, their catalysts can even show a high turnover frequency of about 3.93 s^{-1} at 100 mV overpotential in neutral media. Alternatively, alloying Pt with other inexpensive transition metals is also feasible in reducing the loading of Pt and at the same time harvesting higher activity through alloying effect. Lee *et al.* prepared ternary Pt-Ni-Co nanohexapods through etching of Ni and Co of the Pt@Ni@Co core-shell structures.[16] The as-synthesized Pt-Ni-Co was measured in alkaline media for HER and they showed about 10 times higher in specific activity than that of the commercial Pt/C catalysts. On the other hand, non-noble metal-based water-alkali HER catalysts, such as oxides, sulfides, nitride and phosphides, have also been extensively studied, with the purpose of lowering the costs. However, due the substantial energy barriers of the water dissociation, it is still requiring tremendous efforts to develop both intrinsically active and robust water-alkali HER catalysts.

1.2.2 Oxygen Evolution Reaction (OER)

Even though generating oxygen is not as appealing as hydrogen gas, the major role of oxygen evolution reaction (OER), as a half reaction ($4OH^- \rightarrow 2H_2 + 2H_2O + 4e^-$), is to complete the close circuit of electrochemical water splitting. The reaction kinetics of OER is thus critically important. In fact, in addition to the electrochemical water splitting, OER is also one important half reaction of the other fields such as metal-air batteries. However, due to the sluggish reaction kinetics, OER has become one limitations of these chemical cells.[17]

1.2.2.1 The Mechanism of OER

The widely recognized OER elementary reactions in alkaline media are shown as follows:

$$* + OH^- \rightarrow *OH + e^-$$

$$*OH + OH^- \rightarrow *O + H_2O + e^-$$

$$*O + OH^- \rightarrow *OOH + e^-$$

$$*OOH + OH^- \rightarrow * + O_2 + H_2O + e^-$$

Alternatively, two adjacent *O can also form oxygen gas molecule:

$$2*O \rightarrow 2* + O_2$$

where * is the active sites of the OER catalysts. As can be seen from the elementary reactions, the oxygen gas molecules can be formed through two ways.[9] Each of the elementary reaction is up-hill in energy barrier and accumulates tremendous energy barriers, which is the important reason for the sluggish kinetics of OER mentioned in the last section.[18]

1.2.2.2 Evaluation of OER Electrocatalyst

Similar with HER, there is a thermodynamic potential of OER (1.23 V) under the standard conditions (298 K and 1 atm). The overpotential also exists in OER due to the reasons including activation energy barriers, electrical resistance, and diffusion resistance.[17]

Butler-Volmer equation can also be used to describe the OER process. In Butler-Volmer equation, the reaction (i.e. OER in this case) can be regarded as reversible (i.e. anodic and cathodic reaction). However, apparently the OER corresponds to the anodic dominated direction. In this case, Butler-Volmer equation can be approximated to the following equation (eq. 1.7):

$$j=j_0 e^{\alpha_a nF\eta/RT}$$

where α_a is the transfer coefficient, and j_0 is the exchange current density which is also an important parameter to evaluate the activity of OER catalysts.[19] When transferring equation (eq. 1.7) in the logarithm form, we can have the equation of another parameter, Tafel slope (b, eq. 1.8), for OER:

$$b=\frac{2.3\ RT}{\alpha_a F}$$

It can be seen from the equation of Tafel slope that the b value is dependent on the transfer coefficient. The transfer coefficient α_a can be determined by the following equation (eq. 1.9):

$$\alpha_a=\frac{n_b}{\nu}+n_r\beta$$

where n_b is the electron number involved in the transferring process back to the electrode before the rate-determining step, ν represents the total number of rate-determining step before the studied electron transfer step, n_r is the electron numbers involved in the rate-determining step, and β is symmetry factor (0.5 for the single-electron transfer step). If the first electron transfer step is rate-limiting, the value of n_b should be 0, and the n_r is 1. In this case, the transfer coefficient is 0.5 and the Tafel slope in equation 20 is 120 mV/dec. If the rate limiting step is a chemical reaction following the single-electron transfer step, then the both n_b and ν are 1. But n_r will become 0 as the chemical reaction has no electron transfer involved. The transfer coefficient is 1 and related Tafel slope is about 60 mV/dec. When the second electron transfer step becomes rate limiting, n_b and ν should be 1, and n_r is 1. The transfer coefficient α_a is thus 1.5, and corresponding Tafel slope is 40 mV/dec. Similar with

HER, Tafel slope also indicates the possible mechanism of OER and especially the rate-determining step. A smaller Tafel slope reflects that the rate-determining step is approaching the last step of the series of elementary reaction, which is also desirable for an OER catalyst.[9]

Even though OER has multiple elementary reaction steps, the chemisorption of intermediates was found to have linear relationship with respect to their binding energy. For example, the binding energy of intermediate species of HO*, O* and HOO* can be expressed as a function of the binding energy of O*. A volcano plot has also been plotted to describe relationship between the overpotential versus the change of Gibbs free energy of O adatoms. However, it should be noted that the linear scaling of the OER intermediates is only feasible when overpotential is larger than 370 mV.[20]

1.2.2.3 IrO_x and RuO_2 vs. Economic OER Electrocatalyst

Based on the volcano plot developed for OER, IrO_x and RuO_2 are believed to be benchmark OER catalysts.[17] But there are some stability issues of these noble metal catalysts as well. It has been pointed out that these noble metal oxides tend to be dissolved during the OER measurement. In addition, the high costs of them, due to the scarcity, is also a big challenge of the application in OER. Developing inexpensive transition metal-based materials as OER catalysts has been regarded as an effective strategy to deal with this challenge. For example, a series of metal oxide including NiO, NiFeO, CoOx, etc., have been developed so far and show decent activity towards the OER in alkaline media.

References

1. Acar, C.; Dincer, I. *Int. J. Hydrogen Energy* **2014,** *39*, 1-12.

2. Hassan, M. H.; Kalam, M. A. *Procedia Eng*. **2013,** *56*, 39-53.

3. Winchester, N.; Reilly, J. M. *Energy Econ.* **2015,** *51*, 188-203.

4. Stamenkovic V. R.; Strmcnik D.; Lopes P. P.; Markovic N. M. *Nat. Mater*. **2016,** *16*, 57-69.

5. Zou, X.; Zhang, Y. *Chem. Soc. Rev.* **2015,** *44*, 5148-5180.

6. Gong, M.; Wang, D.-Y.; Chen, C.-C.; Hwang, B.-J.; Dai, H. *Nano Res*. **2016,** *9*, 28-46.

7. Zeng, K.; Zhang, D. *Prog. Energy. Combust. Sci*. **2010,** *36*, 307-326.

8. Mahmood, N.; Yao, Y.; Zhang, J.-W.; Pan, L.; Zhang, X.; Zou, J.-J. *Adv. Sci*. **2018,** *5*, 1700464.

9. Shinagawa, T.; Garcia-Esparza, A. T.; Takanabe, K. *Sci. Rep*. **2015,** *5*, 13801.

10. Trout, B. L.; Parrinello, M. *J. Phys. Chem. B* **1999,** *103*, 7340-7345.

11. Zeng, M.; Li, Y. *J.Mater. Chem. A* **2015,** *3*, 14942-14962.

12. Zheng, Y.; Jiao, Y.; Jaroniec, M.; Qiao, S. Z. *Angew. Chem. Int. Ed*. **2015,** *54*, 52-65.

13. Parsons, R. *Trans. Faraday Soc*. **1958,** *54*, 1053-1063.

14. Nørskov, J. K.; Bligaard, T.; Logadottir, A.; Kitchin, J. R.; Chen, J. G.; Pandelov, S.; Stimming, U. *J. Electrochem. Soc*. **2005,** *152*, J23-J26.

15. Jiang, K.; Liu, B.; Luo, M.; Ning, S.; Peng, M.; Zhao, Y.; Lu, Y.-R.; Chan, T.-S.; de Groot, F. M. F.; Tan, Y. *Nat. Commun*. **2019,** *10*, 1743.

16. Oh, A.; Sa, Y. J.; Hwang, H.; Baik, H.; Kim, J.; Kim, B.; Joo, S. H.; Lee, K. *Nanoscale* **2016,** *8*, 16379-16386.

17. Suen, N.-T.; Hung, S.-F.; Quan, Q.; Zhang, N.; Xu, Y.-J.; Chen, H. M. *Chem*. *Soc*. *Rev*. **2017,** *46*, 337-365.

18. Dau, H.; Limberg, C.; Reier, T.; Risch, M.; Roggan, S.; Strasser, P. *ChemCatChem* **2010,** *2*, 724-761.

19. Bard, A. J., *Electrochemical methods : fundamentals and applications/Allen J. Bard, Larry R. Faulkner*. Wiley: New York, 1980.

20. Man, I. C.; Su, H.-Y.; Calle-Vallejo, F.; Hansen, H. A.; Martínez, J. I.; Inoglu, N. G.; Kitchin, J.; Jaramillo, T. F.; Nørskov, J. K.; Rossmeisl, J. *ChemCatChem* **2011,** *3*, 1159-1165.

Chapter 2

Theoretical and Experimental Insight into the Effect of Nitrogen Doping on Hydrogen Evolution Activity of Ni_3S_2 in Alkaline Medium

Abstract

Nickel sulfide (Ni_3S_2) is a promising hydrogen evolution reaction (HER) catalyst by virtue of its metallic electrical conductivity and excellent stability in alkaline medium. However, the reported catalytic activities for Ni_3S_2 are still relatively low. Here we demonstrate an effective strategy to boost the H adsorption capability and HER performance of Ni_3S_2 through nitrogen (N) doping. N doped Ni_3S_2 nanosheets achieve a fairly low overpotential of 155 mV at 10 mA cm^{-2} and an excellent exchange current density of 0.42 mA cm^{-2} in 1.0 M KOH electrolyte. The mass activity of 16.9 mA mg^{-1} and turnover frequency of 2.4 s^{-1} obtained at 155 mV are significantly higher than the values reported for other Ni_3S_2 based HER catalysts, and comparable to the performance of best HER catalysts in alkaline medium. These experimental data together with theoretical analysis suggest that the outstanding catalytic activity of N doped Ni_3S_2 is due to the enriched active sites with favorable H adsorption free energy. The activity in the Ni_3S_2 is highly correlated with the coordination number of the surface S atoms and the charge depletion of neighbor Ni atoms. These new findings provide important guidance for future experimental design and synthesis of optimal HER catalysts.

2.1 Introduction

Among different hydrogen generation methods, water electrolysis, a zero carbon emission process, represents a promising environmentally friendly strategy.[1-3] Water

electrolysis reaction is typically performed in an alkaline medium such as KOH, in which metal electrodes are more durable compared to acid media.[4,5] Platinum group metals are known to be the best hydrogen evolution reaction (HER) catalysts because hydrogen adsorption free energy on these metal surfaces are almost thermally neutral.[6] Nonetheless, the scarcity and high cost of platinum group metals severely restrict their applications as HER catalyst.[7] Design and synthesis of non-noble metal based HER catalysts with high catalytic activity in alkaline media have thus become highly desirable yet challenging.[8,9]

Non-noble metal based chalcogenides such as MoS_2 structures have been demonstrated as excellent HER catalysts that contain active sites with hydrogen adsorption energy close to zero.[10-14] However, the catalytic efficiency of MoS_2 is somewhat hindered by its inferior electrical conductivity.[9,15] Therefore, it is beneficial to have a highly electrically conductive HER catalyst.[16] Ni_3S_2, also called heazlewoodite, is a naturally occurring nickel sulfide mineral, exhibit metallic conductivity due to the presence of Ni-Ni network in its crystal structure. Pristine Ni_3S_2 nanostructures showed decent HER activity in alkaline media.[17-26] For example, Ni_3S_2 nanoparticles achieved an overpotential of 335 mV at the current density of 10 mA cm^{-2}.[21] Ni_3S_2 nanosheets with high-index crystal facets demonstrated an even lower overpotential of 223 mV at the same current density.[19] These pioneering works suggested the promise of Ni_3S_2 nanomaterials as HER catalyst in alkaline media. Unlike two-dimensional MoS_2, the HER activity of Ni_3S_2 has been rarely studied. Specifically, theoretical and experimental studies on pristine Ni_3S_2 surfaces with special concerns on stable facet termination are rarely reported, and theoretical insights on heteroatom

doped Ni_3S_2 HER catalysts have not been given in the research community to the best of our knowledge.[19,27]

We anticipate that enriching the active sites on the highly electrically conducting Ni_3S_2 can effective promote its hydrogen evolution activity. It is known that the difference of electronegativity between N (with an electronegativity of 4.13) and H is larger than that between S (with an electronegativity of 3.21) and H, therefore we believe that the implantation of N in Ni_3S_2 can favor the adsorption of H which is indispensable to vigorous HER. Here we demonstrate ammonia treatment is an effective strategy to simultaneously enrich the active sites on Ni_3S_2 nanosheets and improve its intrinsic catalytic activity towards HER in alkaline electrolyte. N doped Ni_3S_2 achieves a low overpotential of 155 mV at 10 mA cm^{-2}, corresponding to an excellent mass activity of 16.9 mA mg^{-1} and TOF of 2.4 s^{-1} at the same overpotential, and an outstanding exchange current density of 0.42 mA cm^{-2}. DFT calculations show that the H adsorption is highly facilitated in the new active facet after ammonia treatment. Surface chemical bonding environment study also further unveiled the mechanism of activity enhancement through N doping.

2.2 Experimental Section

Preparation of Ni_3S_2 and N-doped Ni_3S_2 nanosheets: Thiourea (1.32 mg) was dissolved in deionized water (12 mL) under vigorous stirring until the solution became homogeneous. A piece of nickel foam after cleaning in acetone and ethanol was transferred into a Teflon-lined stainless autoclave. The autoclave was filled with the thiourea solution and heated in an oven at 150 ^oC for 5 hours. After cooling down the autoclave at room temperature, the sample was taken out, rinsed with deionized water

and ethanol, and dried in vacuum at room temperature. The nickel foam was coated uniformly with a thin layer of Ni_3S_2 nanosheets. To prepare N-doped Ni_3S_2, the as-prepared Ni_3S_2 nanosheets were further annealed in a tube furnace filled with ammonia gas at 350°C for 30 min.

Calculation of the mass loading of the Ni_3S_2 nanosheets: Ni_3S_2 nanosheets were synthesized by the abovementioned hydrothermal method, according to the reaction $3Ni+2S \rightleftharpoons Ni_3S_2$. Ni was in excess in the synthesis of Ni_3S_2. The clean Ni foam was weighed before the growth, and the mass loading of Ni_3S_2 was calculated based on the weight increase of Ni foam after the growth, assuming the increased weight (0.74 mg) is due to the addition of sulfur. Therefore, the mass loading of $Ni_3S_2 = \frac{0.74}{M_S} \times \frac{1}{2} \times M_{Ni3S2}$, where M_S and M_{Ni3S2} are the molar mass of S and Ni_3S_2, respectively. ½ is the molar ratio of Ni_3S_2 to S. The area of the Ni foam is 4.65 cm^2. The areal mass loading of Ni_3S_2 was calculated to be ~0.6 mg cm^{-2}.

Materials Characterization: The phase composition of the samples was characterized by X-ray diffractometer (XRD, Rigaku Americas Miniflex Plus). Field-emission scanning electron microscopy (FE-SEM, Hitachi S-4800 II) and transmission electron microscopy (TEM, JEM 2010-HR) were employed to investigate the crystal structure of the samples. Elemental mapping was performed by electron energy loss spectroscopy (EELS). Surface elemental information was obtained by using X-ray Photoelectron Spectroscopy (XPS, ESCALab 250).

Electrochemical Measurements: The electrochemical measurements were carried out in a three-electrode system with Hg/HgO as the reference electrode and carbon rod as the counter electrode using electrochemical workstation (CHI 660D). The

measurement was performed in KOH (1.0 M) solution and the all of the measured potentials (vs. Hg/HgO) were converted to the potentials vs. the reversible hydrogen electrode (RHE). Linear sweep voltammetry (LSV) with a scan rate of 5 mV s^{-1} was used to measure the performances. Electrochemical impedance spectroscopy was carried out at -0.159 V vs. RHE with frequencies starting from 100 kHz to 1 Hz (amplitude of 5 mV). The electrochemical surface area (ECSA) was characterized according to a reported method. Specifically, cyclic voltammograms were collected in a narrow potential window (0.104 to 0.204 V vs. RHE) where no faradaic reactions occur. A series of scan rates (from 4 mV s^{-1} to 40 mV s^{-1} at an interval of 4 mV s^{-1}; 5 cycles for each scan rate) were collected and a linear relationship was obtained between J_{anodic}-$J_{cathodic}$ (at 0.150 V vs. RHE) and scan rate, in which the slope is proportional to the electrochemical surface area. Hydrogen gas was collected at the overpotential of 300 mV for 60 min using water displacement method. According to the equation that PV=nRT, the moles of hydrogen gas should be: n=PV/RT, where P is 101325 Pa, V is the collected volume of hydrogen gas, R is 8.314 J mol^{-1} K^{-1}, and T is 298 K.

DFT Simulations: Density Functional Theory calculations of Ni_3S_2 were performed using open source Quantum ESPRESSO plane wave codes with norm conserving pseudopotentials. The Ni pseudopotentials includes eight 3S, 3P semicore electrons in the valence partition, whereas all other pseudopotentials (H and O) include valence electrons. We employed the PBE generalized gradient approximation (GGA) to the exchange correlation functional. We compared PBE with PBE+D2 that includes pair potential corrections to account for the long-range London dispersion interactions, and found less than 0.05 eV difference for the hydrogen adsorption energy. We used kinetic

energy cutoffs of 70 Ry for wave functions and 280 Ry for charge density. Because Ni_3S_2 is metallic, a cold smearing width of 10^{-3} Ry was applied for Brillouin zone integration. Total energy was calculated self consistently until a convergence of 10^{-8} Ry was achieved and geometry was optimized until the net force per atom reached a threshold of 10^{-3} Ry/au. Bulk Ni_3S_2 crystal has a 5-atom cubic primitive cell with a computed lattice constant of $a = 4.08$ Å. For surface calculations we cut the bulk structure according to the desired miller index, creating a new unit cell which we expanded to a 331 supercell for the (100) facet and a 221 supercell for the (-111) facet (details of stable termination below). For the N doped surfaces, two doping concentrations are considered: one N per eight/nine S surface atoms at the (-111)/(100) facet, and two N per eight/nine S surface atoms at the (-111)/(100) facet. For the former concentration, the N-N distance is ~12 Å which is far enough to consider no interaction between two N dopants; for the later concentration, we substitute two nearby S atoms (bridged by Ni atoms) by two N atoms (a N-N distance of ~3.1 Å) to represent interacting N atoms at a high doping concentration.

For all slab systems, we implemented a 2x2x1 Monkhorst-Pack k-point mesh with a vacuum separation of 15 Å. Additionally, all slabs had the bottom half of the atoms fixed with bulk geometry while the top half are allowed to relax to simulate the surface. Due to breaking inversion symmetry, we applied a dipole field correction along the vacuum direction. We used a smearing of 0.005 Ry to resolve the Fermi surface of Ni_3S_2 with the Marzari-Vanderbilt cold smearing, because Ni_3S_2 is a metallic system. The solved calculations are performed using the open source DFT code JDFTx, specifically the CANDLE solvation model that has been shown suitable for various

types of surfaces. The phonon vibrational frequencies (used for the entropy and zero point energy calculations) are computed by Density Functional Perturbation Theory (DFPT) for all the molecules and surface atoms. We can determine the most stable termination of facets of Ni_3S_2 by computing the surface energy of each termination by (eq. 2.1).

$$\gamma = \frac{1}{A}\left[E_{slab} - \frac{1}{2}E_{slab}^{unrelaxed} - \frac{1}{2}\sum_i \mu_i N_i\right]$$

Where A is the surface area of the slab, E_{slab} is the electronic energy of the relaxed slab, $E_{slab}^{unrelaxed}$ is the electronic energy of the unrelaxed slab, μ_i is the chemical potential of species i and N_i is the number of species i present in the slab. The unrelaxed term accounts for the cost of fixing half of the slab with the bulk geometry and the rest makes up the surface energy of just the relaxed half. From (eq. 2.1) we have to determine both the chemical potential of Ni and S. Yet, we can fix one of these variables according to (eq. 2.2).

$$3\mu_{Ni} + 2\mu_S = \mu_{Ni_3S_2}$$

Approximating the chemical potential of Ni_3S_2 as the energy of a single bulk Ni_3S_2 unit we have $\mu_{Ni_3S_2} \approx E_{bulk}$. Therefore we eliminate μ_{Ni} in (eq. 1) by rewriting it in terms of μ_S and E_{bulk}. Next we observe that the chemical environment can range between two extremes: (i) S rich where $\mu_S = E_{S,\,bulk}$ and (ii) Ni Rich with $\mu_{Ni} = E_{Ni,\,bulk}$. These conditions along with (eq. 2) provide a range for chemical potential of S (eq. 2.3).

$$\frac{1}{2}E_{bulk} - \frac{3}{2}E_{Ni,bulk} < \mu_S < E_{S,\,bulk}3$$

Lastly inserting eq. 4 into eq. 3 we obtain an explicit equation for the surface energy of our Ni_3S_2 slabs (eq. 2.4).

$$\gamma = \frac{1}{A}\left[E_{slab} - \frac{1}{2}E_{slab}^{unrelaxed} - \frac{1}{2}\left(\frac{N_{Ni}}{3}E_{bulk}\right) + \frac{1}{6}\mu_S(2N_{Ni} - 3N_S)\right]$$

Using (eq. 2.3) and (eq. 2.4) we plotted surface energy of different terminations of the (100) facet of Ni_3S_2 as a function of $\Delta\mu_S = \mu_S - E_{S,bulk}$ (Figure 2.6a). Based on the experimental synthesis process there is an abundance of Nickel foam present in the system and therefore we expect that the terminations with lower surface energy in a Ni rich environment (low μ_S) are more likely realized in experiment. Therefore we choose to use the $(100)_{Ni+1}$ surface for our study since this surface is more stable in a Ni rich environment. The 331 supercell of the $(100)_{Ni+1}$ surface is plotted in (Figure 2.6b and c) containing 90 atoms. Our results for the termination for (100) agree with the results of previous report (although they did not discuss S rich or Ni rich conditions). On the other hand, we are unable to compare our results to some report because they did not discuss the terminations we found to be most stable for the (100) surface. Similarly, we plotted the surface energy for possible terminations of the (-111) surface (Figure 2.11a) and we found that the $(-111)_{Ni+1}$ surface is more stable in a Ni rich environment and is therefore more likely realized in experiment. The 221 supercell of the (-111) facet is shown in (Figure 2.11b and c) containing 76 atoms. Again, we are unable to fully compare our results for this surface to (ref. 5) as they did not discuss the termination $(-111)_{Ni+1}$. It is well established that the H adsorption free energy computed from DFT, ΔG_{H^*}, correlates well with the exchange current density measured in experiment. Specifically, if ΔG_{H^*} is close to 0 (within ~ 0.2 eV) it is indicative of a more active

surface for HER. Therefore, in order to understand the catalytic performance for HER we computed the H adsorption free energy, ΔG_{H^*} (eq. 2.5) at different sites and surfaces of Ni_3S_2 obtained in experiment.

$$\Delta G_{H^*} = \Delta E_{H^*} - T\Delta S + \Delta ZPE + \Delta F_{solvation}$$

From (eq. 2.5) we compute ΔG_{H^*} at different sites on the surface where ΔE_{H^*} is the hydrogen adsorption electronic energy at zero temperature, ΔS is change in entropy, ΔZPE is change in zero point energy and $\Delta F_{solvation}$ is the change of solvation energy of the surfaces by using the implicit solvation model which has been shown to be suitable to apply to various solid surfaces. The results of this calculation are displayed in (Table 2.2).

2.3 Results and Discussions

Ni_3S_2 nanosheets were hydrothermally synthesized on a nickel foam substrate through the sulfidization of nickel by thiourea, followed by annealing in nitrogen at 350 ^oC for 30 min (Figure 2.1a). The sample is denoted as Ni_3S_2/NF. As shown in Figure 2.2a, the Ni foam substrate is uniformly covered by vertically aligned nanosheets, which have an average lateral size of 1-2 microns and thickness of several tens nm. Although the X-ray diffraction signal of Ni_3S_2 is relatively weak compared to the strong Ni substrate signal due to its small loading (Figure 2.3), the chemical environments of Ni and S are confirmed by X-ray photoelectron spectroscopy (Figure 2.4). The core level Ni 2p XPS spectrum shows a pair of spin-orbit doublets and two shake-up satellite peaks (Figure 2.4a), which are consistent with that of Ni 2p characteristic peaks reported for Ni_3S_2.[28,29] In S 2p XPS spectrum, the minor peak located at 161.3 eV and the doublets of $2p_{1/2}$ and $2p_{3/2}$ located at 163.4 and 162.4 eV

(Figure 2.4b) are consistent to the reported S-Ni signals in Ni_3S_2, while the satellite peak centered at 168.6 eV can be ascribed to the sulfate species.[30, 31] Transmission electron microscopy (TEM) studies further revealed that the Ni_3S_2 nanosheets are single crystals with (100) facet as basal plane (Figure 2.5a). The uniform elemental distribution of Ni and S is confirmed by electron energy loss spectroscopy (EELS) mapping (Figure 2.5b). Complementary to the structural characterization, density function theory (DFT) provides deeper understanding on the possible facet terminations which are believed to be closely related to the HER activity. Combined with thermodynamics analysis, the surface energy of the exposed (100) facet termination of Ni_3S_2 was investigated with respect to the elemental chemical potential of S (μ_S, Figure 2.6a). The profiles of the optimized most stable termination are illustrated in Figure 2.6b and c and are found to be consistent with the previous results (optimization methods shown in Supporting Information).[19]

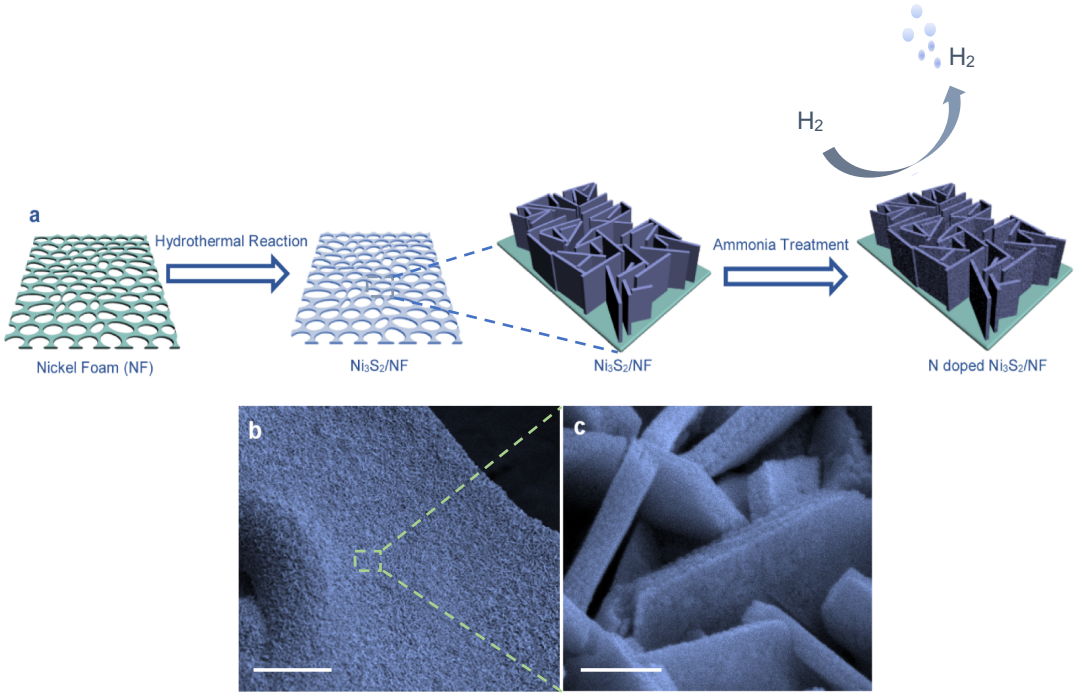

Figure 2.1 (a) Schematic illustration of the synthesis of Ni_3S_2/NF and N doped Ni_3S_2/NF. (b) SEM image of N doped Ni_3S_2 nanosheets grown on the Ni foam. Scale bar is 20 μm. (c) Magnified SEM image of N doped Ni_3S_2 nanosheets highlighted in the dashed box in (b). Scale bar is 300 nm.

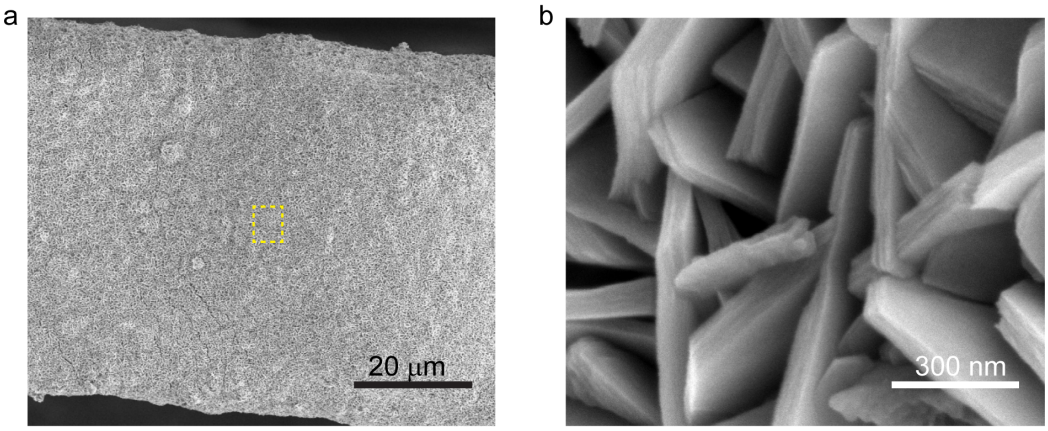

Figure 2.2 (a) SEM image of the Ni_3S_2 nanosheets grown on NF. (b) Magnified SEM image of the region highlighted in dashed box in (a).

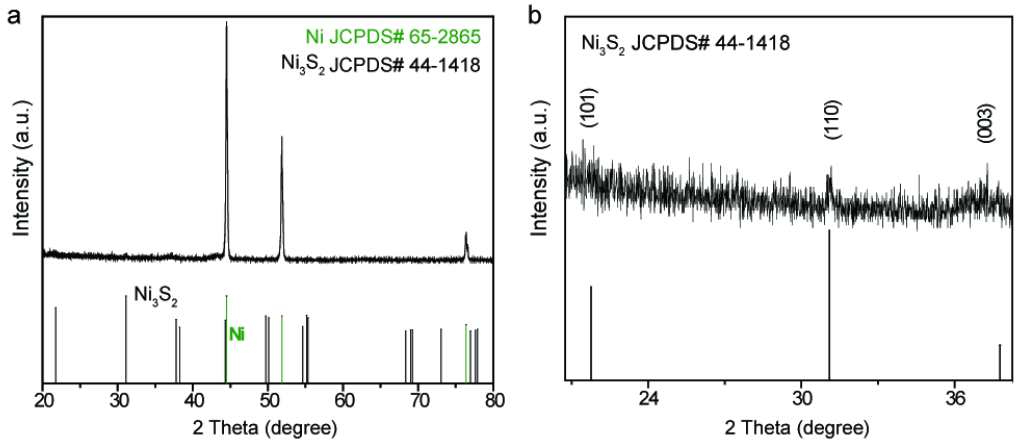

Figure 2.3 (a) XRD spectrum of Ni_3S_2/NF. (b) Magnified XRD spectrum of the region highlighted in dashed box of (a). Diffraction peaks for Ni_3S_2 (JCPDS 44-1418) are labeled with (hkl). The lines at the bottom indicate the diffraction peaks of Ni (JCPDS 65-2865) and Ni_3S_2 (JCPDS 44-1418).

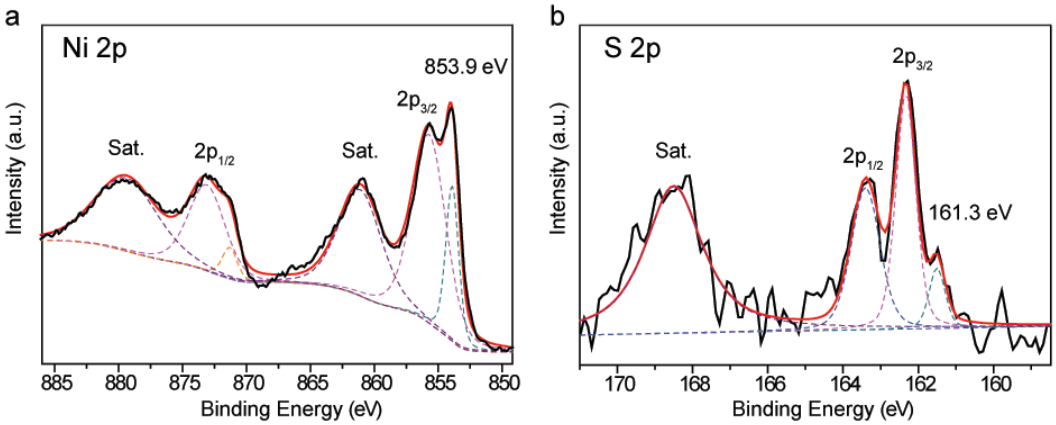

Figure 2.4 Core level (a) Ni 2p and (b) S 2p XPS spectra collected for Ni_3S_2/NF. The black solid curves are the experimental results, which can be deconvoluted into synthetic peaks (dashed lines). The red solid curves are the summation of the synthetic peaks.

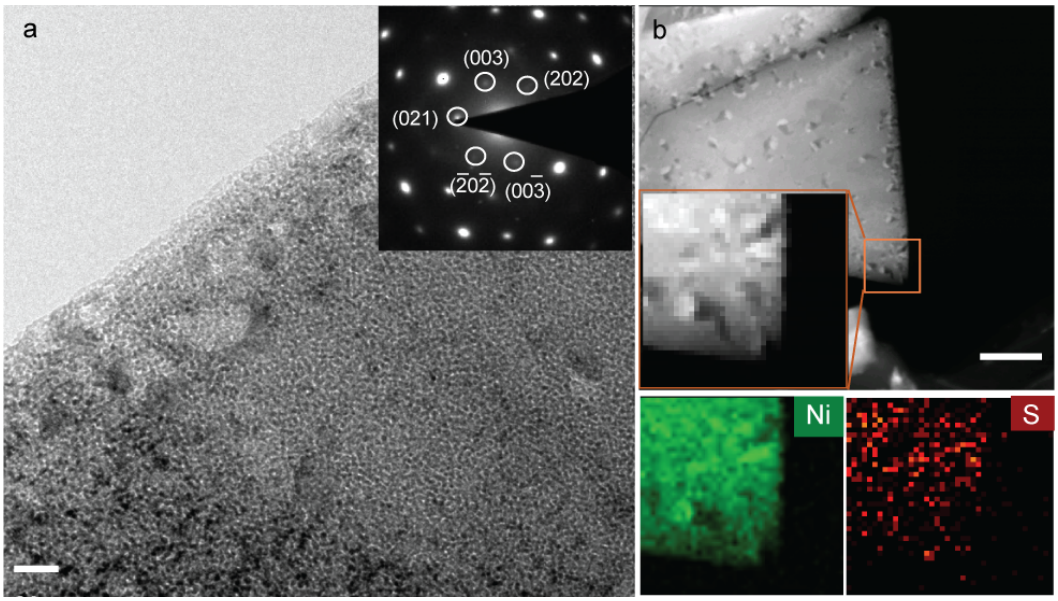

Figure 2.5 (a) TEM image of Ni_3S_2/NF. Inset: selected area electron diffraction. Scale bar is 20 nm (b) HAADF-STEM image and corresponding elemental mapping images, Ni (L-edge, green), and S (L-edge, red). Scale bar is 200 nm.

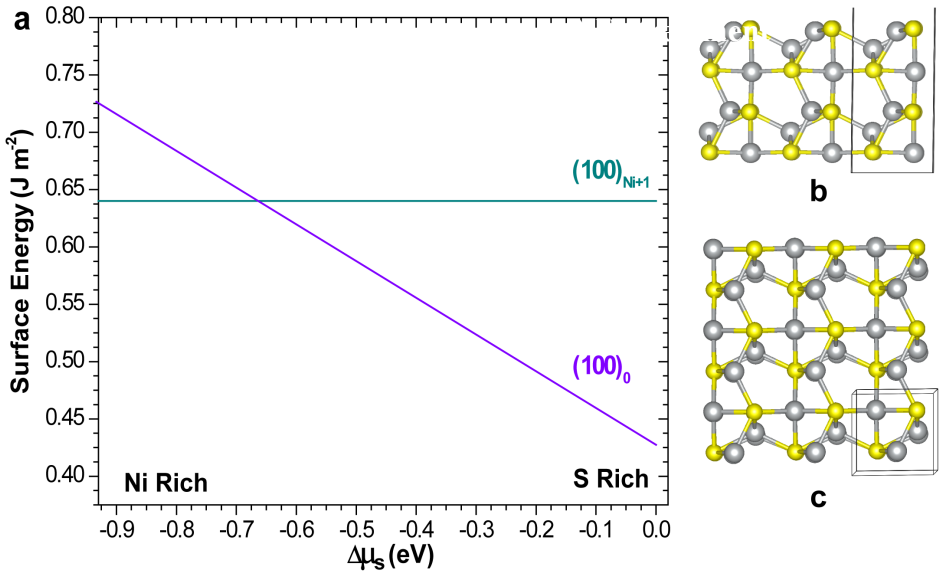

Figure 2.6 (a) Surface energy of possible termination of the (100) surface as a function of S chemical potential $\boldsymbol{\Delta\mu_S}$. (b, c) Side and top views of the most stable termination of the (100) facet of Ni_3S_2 (grey sphere represents Ni and yellow sphere represents S), respectively.

The HER performances of Ni_3S_2/NF were evaluated in 1.0 M KOH solution through a three-electrode system. It shows a decent electrocatalytic activity for hydrogen generation with a current density of 10 mA cm^{-2} achieved at an overpotential of 240 mV (Figure 2.7a). The Ni_3S_2/NF has a Tafel slope of 152 mV dec^{-1} (Figure 2.7c), which is comparable or slightly larger than the values reported for different Ni_3S_2 based HER catalysts, such as Ni_3S_2 film/NF (160 mV dec^{-1}),[26] Ni_3S_2 nanorods array/NF (107 mV dec^{-1}),[24] and NiS_2 nanoparticles (128 mV dec^{-1})[21] obtained in the same 1.0 M KOH electrolyte. The Tafel slope at around 120 mV dec^{-1} or above indicates that the overall HER rate is possibly controlled by Volmer step, in which the H_3O^+ environment in alkaline medium makes the H adsorption (H^*) unfavorable and resulting in lower surface coverage by H.[32,33] The results suggested that Ni_3S_2/NF has relatively large barrier for H adsorption in Volmer step. The H adsorption free energy (ΔG_{H^*}) has been both experimentally and theoretically proved to be an important indicator for the overall HER activity.[9] Either too negative or too positive values of ΔG_{H^*} can result in strong binding or weak binding of H on the facet of catalysts accordingly, representing undesirable surface conditions for HER kinetics.[9] Therefore it has been widely accepted that H adsorption favorable facet should have a ΔG_{H^*} close to zero. On the (100) surface of pristine Ni_3S_2 (denoted as p-(100)), there are two types of sites for possible H adsorption: Ni site (denoted as p-$Ni_{(100)}$) and S site (denoted as p-$S_{(100)}$). Our calculated ΔG_{H^*} of the two kinds of sites are 0.583 eV (p-$Ni_{(100)}$) and 1.086 eV (p-$S_{(100)}$), respectively from first principles, which are close to the reported values of ΔG_{H^*} of Ni (0.747 eV) and S (1.179 eV) site on (100) facet of Ni_3S_2 (the small difference with our results is due to their inclusion of a semi-empirical van der Waals correction).[19] The

adsorption energy results indicate that the H adsorption should be further facilitated (to decrease the absolute value of ΔG_{H^*}) for enhanced HER activity, and building a H adsorption favorable surface with enriched active sites and lowered H adsorption energy is thus desired.

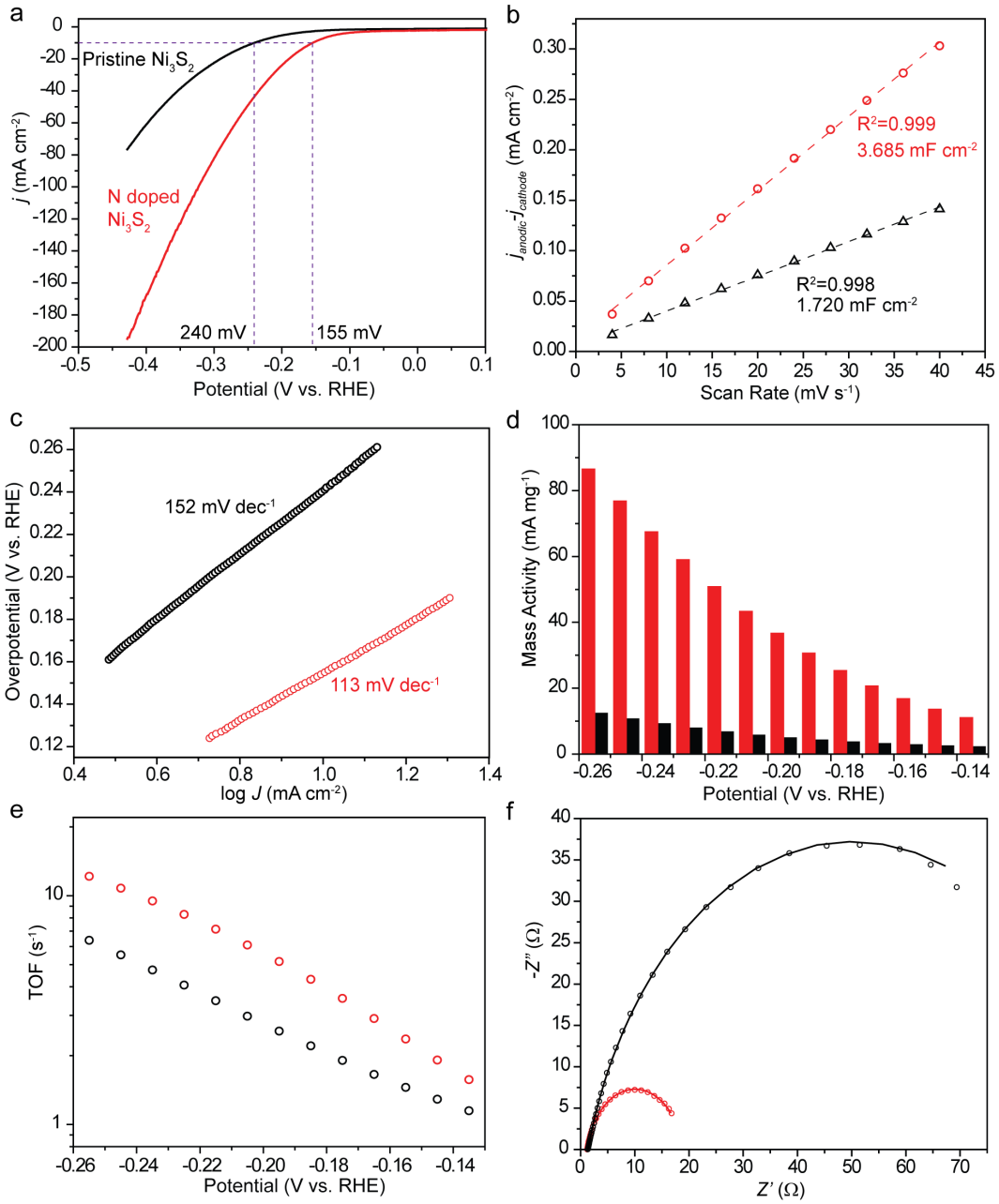

Figure 2.7 (a) HER polarization curves of the pristine (black) and N doped Ni_3S_2/NF (red) collected in 1 M KOH at a scan rate of 5 mV s^{-1} (dashed lines highlight the potential at 10 mA cm^{-2}). (b) Difference of anodic current and cathodic current is plotted as a function of scan rate. (c) Tafel plots of the pristine and N doped Ni_3S_2/NF. (d) Mass activity (normalized to Ni_3S_2 mass loading) and (e) Turnover frequency of the pristine and N doped Ni_3S_2/NF are plotted as a function of applied potential. (f) Electrochemical impedance spectra collected at -0.159 V vs. RHE with frequencies from 100 kHz to 1 Hz and amplitude of 5 mV. Dots and lines represent the experimental and simulated results, respectively.

We aimed to activate the Ni_3S_2 through N doping, with a goal of introducing new active sites for H adsorption. The Ni_3S_2 nanosheets synthesized through hydrothermal reaction were annealed in the ammonia atmosphere at 350 ^oC for 30 min (Figure 2.1). SEM images show that the morphology of Ni_3S_2 nanosheets was retained after ammonia treatment, while the nanosheet surfaces were roughened (Figure 2.1b and c). The ammonia treatment did not lead to phase or compositional transformation, as evidenced by the XRD results shown in Figure 2.8. The Ni 2p XPS spectrum of ammonia treated Ni_3S_2 exhibits a new peak centered at 870.2 eV that can be ascribed to Ni-N (Figure 2.9), confirming successful incorporation of nitrogen in Ni_3S_2.[30,31,34] N 1s spectrum further confirmed the chemical nature of nitrogen in Ni_3S_2, in which the signals at binding energy of 399.6 eV and 398.1 eV have been reported for interstitial and substitutional nitrogen, respectively.[35,36] EELS mapping results revealed that Ni, S and N are homogeneously distributed in the roughened N doped Ni_3S_2 nanosheet (Figure 2.10). The 'diffraction ring' of SAED indicates that the single crystal Ni_3S_2 nanosheets were converted into polycrystalline structure with new crystal planes such as (-111) exposed (Figure 2.10c and d). By varying the elemental chemical potential of S, the corresponding surface energy of (-111) are calculated and the most stable termination of (-111) facet is illustrated in Figure 2.11.

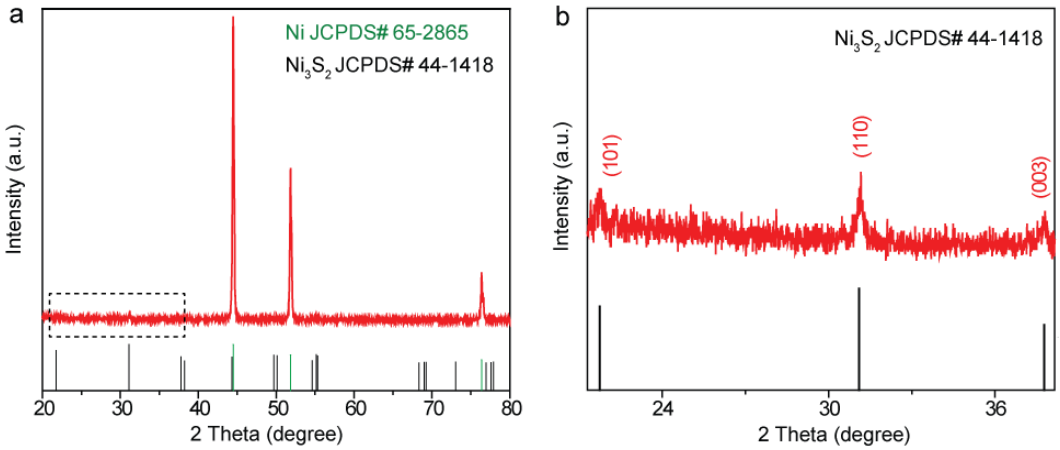

Figure 2.8 (a) XRD patterns of the NH_3 treated Ni_3S_2/NF. (b) Magnified spectrum highlighted by the dashed box in (a).

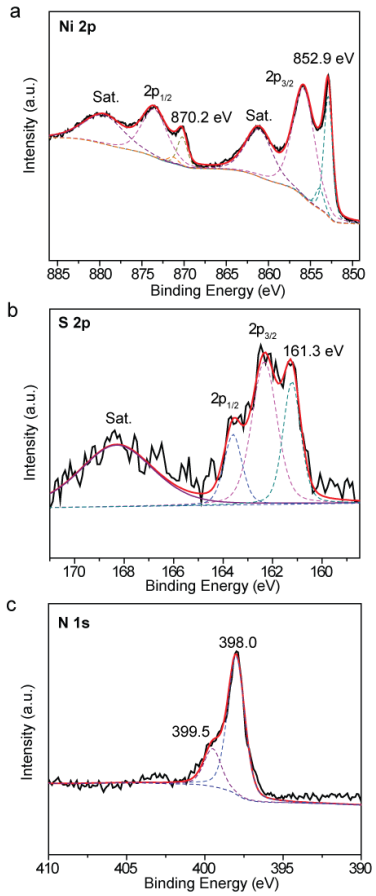

Figure 2.9. Core level (a) Ni 2p, (b) S 2p and (c) N 1s XPS spectra collected for N doped Ni_3S_2/NF. The black solid curves are the experimental results, which can be deconvoluted into synthetic peaks (dashed lines). The red solid curves are the summation of the synthetic peaks.

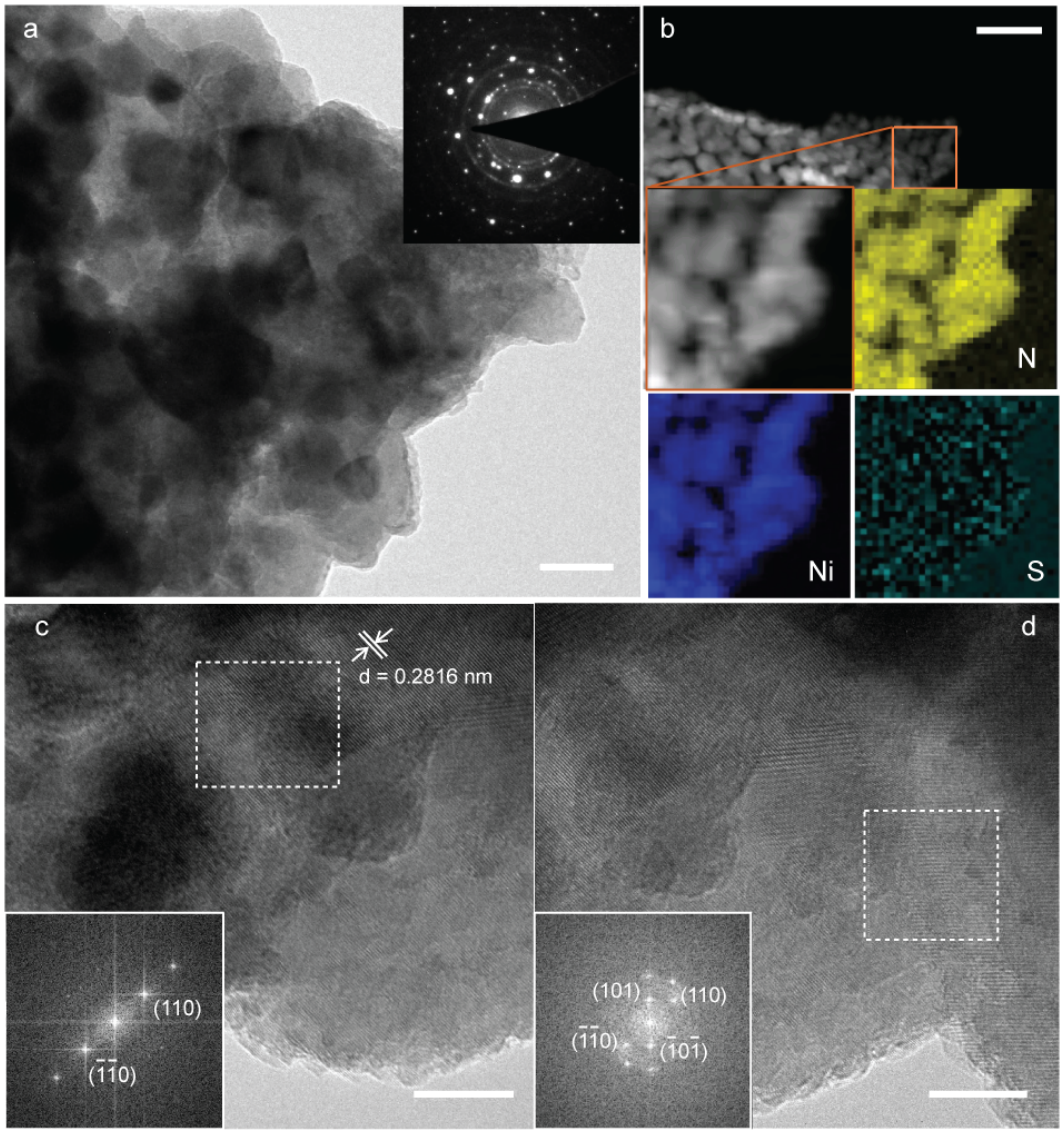

Figure 2.10 (a) TEM image collected from a N doped Ni_3S_2 nanosheet. Scale bar is 20 nm. Inset: selected area electron diffraction pattern. (b) HAADF-STEM image of a N doped Ni_3S_2 nanosheet and corresponding elemental mapping of Ni (L-edge), S (L-edge) and N (K-edge). Scale bar is 100 nm. (c, d) TEM images and corresponding Fast Fourier Transform (FFT) images created from the regions highlighted by the dashed boxes of a N doped Ni_3S_2 nanosheet.

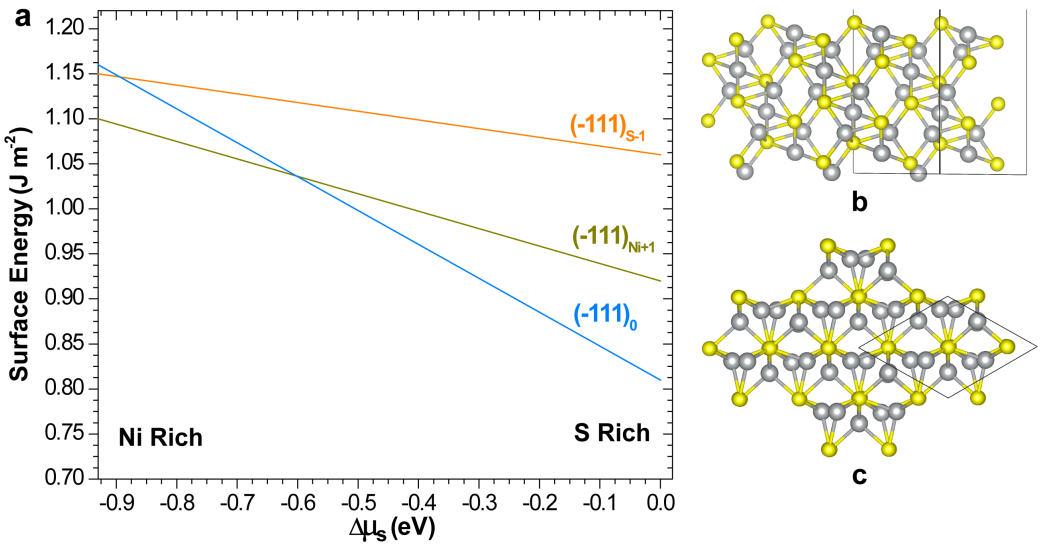

Figure 2.11 (a) Surface energy of possible terminations of the (-111) surface as a function of S chemical potential $\Delta\mu_S$. (b, c) Side and top views of the most stable termination of the (-111) facet of Ni_3S_2 (grey sphere represents Ni and yellow sphere represents S), respectively.

In comparison to pristine Ni_3S_2, the N doped Ni_3S_2 nanosheets obtained at 350 °C for 30 min exhibit significantly lower overpotential about 155 mV at 10 mA cm^{-2} in 1.0 M KOH solution (Figure 2.7a and Figure 2.12). The performance of N doped Ni_3S_2 is getting worse by either decreasing/increasing the annealing temperature or time, as shown in Figure 2.13. To eliminate the influence of Ni foam substrate on the HER activity of Ni_3S_2/NF, the HER performance of two random selected Ni foams were investigated. As shown in Figure 2.14a, they have almost identical polarization curves with an overpotential of 272 mV at 10 mA cm^{-2}. Even though the ammonia treatment can also slightly improve the HER performance of Ni foam, the overpotential of 259 mV obtained at 10 mA cm^{-2} is still much higher than that of N doped Ni_3S_2 (Figure 2.14b). These results confirm that the substrate variation is low and the effect of Ni foam substrate on the overall activity of N doped Ni_3S_2/NF is small. In other words, N

doped Ni_3S_2 nanosheets are indeed the active HER catalyst. That being said, the Ni foam also provides additional advantages for enhancing the HER electrode performance. For example, it serves as a current collector and growth substrate for Ni_3S_2. The high electrical conductivity of Ni, and the strong connection between the Ni substrate and Ni_3S_2 can facilitate electron transfer during HER. Additionally, its porous structure allows efficient diffusion of reactants and evolution of bubbles, which is critical for achieving high HER current. The overpotential of N doped Ni_3S_2/NF is smaller than the values reported for a number of HER catalysts at the same current density of 10 mA cm^{-2}, including Ni_3S_2/NF,[19,24,37] $NiCo_2S_4$/NF (210 mV),[37] $CoSe_2$ (190 mV),[38] Co, CoO_x/N doped carbon (232 mV),[39] and CoP/Carbon Cloth (209 mV)[40]. The greatly enhanced activity of N doped Ni_3S_2/NF can be attributed to the newly exposed crystal planes that offer additional active sites for HER, as the electrochemical surface area (ECSA, derived from the double-layer capacitances, C_{dl}, shown in Figure 2.7b) of Ni_3S_2/NF was increased by two-fold after ammonia treatment. Nevertheless, by normalizing the current of the catalysts to the ECSA (Figure 2.15), the N doped Ni_3S_2 still shows a considerably smaller overpotential (241 mV at 10 mA cm^{-2}) than the pristine Ni_3S_2 (291 mV at 10 mA cm^{-2}). This is a strong evidence that the enhanced HER performance is not only due to the increased ECSA, the new active sites also boost the intrinsic HER activity of Ni_3S_2. The N doped Ni_3S_2 shows a decreased Tafel slope compared to pristine Ni_3S_2 (Figure 2.7c), suggesting that H adsorption in the Volmer step is facilitated. The N doped Ni_3S_2 exhibits an outstanding exchange current density of 0.42 mA cm^{-2}, which is about 1.6 times higher than that of the pristine sample. This value is also significantly higher than the values reported for other HER catalysts

in alkaline medium such as Ni_3S_2/carbon nanotube (0.0075 mA cm^{-2}),[41] $NiMo_3S_4$ (0.039 mA cm^{-2}),[42] Mo_2C (0.0044 mA cm^{-2}),[43] and MoC_x (0.029 mA cm^{-2})[44]. Areal current density can be used to evaluate and compare the performance of HER catalysts only if they have comparable areal mass loading of active catalytic materials. Mass activity and the turnover frequency (TOF) offer important insights in evaluating the intrinsic activity of HER catalysts based on mass loading and surface area, respectively. As shown in Figure 2.7d, the ammonia treatment boosts the mass activity of Ni_3S_2/NF at all potentials we studied. At the current density of 10 mA cm^{-2}, the N doped Ni_3S_2/NF achieves an excellent mass activity of 16.9 mA mg^{-1} (at -155 mV vs. RHE), which is higher than 10 mA mg^{-1} (at -240 mV vs. RHE) of the pristine Ni_3S_2/NF and 6.25 mA mg^{-1} (-223 mV vs. RHE) of Ni_3S_2 catalysts reported previously (Figure 2.7c).[19] The enhanced mass activity is believed to be due to the enriched active sites (increased ECSA). Furthermore, the H_2 TOFs of N doped Ni_3S_2 are 1.4 to 2.0 times higher than the values obtained for pristine Ni_3S_2 at the same overpotential (Figure 2.7e). It is noteworthy that the TOF was calculated by assuming all of the surface sites (including both Ni and S sites) on ECSA are involved in HER, which represents the lower limit of TOF.[45] The increased TOF confirmed that N doping enhances the activity of (100) facet and/or the newly exposed active sites have higher activity than the sites on pristine Ni_3S_2. Furthermore, we also investigate and compare the hydrogen production rate of Ni_3S_2/NF and N doped Ni_3S_2/NF. The N doped Ni_3S_2 generates hydrogen at a rate of 219.2 μmol h^{-1} at the overpotential of 300 mV which is much higher than the rate of 109.6 μmol h^{-1} obtained from Ni_3S_2/NF at the same conditions, further confirming the enhanced activity of N doped Ni_3S_2. Electrochemical impedance spectroscopy (EIS)

measurements showed that ammonia treatment reduced the charge transfer resistance (R_{ct}) of Ni_3S_2/NF from the 195.9 Ω cm^{-2} to 35.2 Ω cm^{-2} (Figure 2.7f and Table 2.1), suggesting HER kinetics on N doped Ni_3S_2/NF surface is enhanced, which is consistent with the results of Tafel plots. We also investigated the stability of Ni_3S_2/NF and N doped Ni_3S_2/NF. As shown in Figure 2.16, we found that the Ni_3S_2/NF shows comparable overpotentials at 10 mA cm^{-2} of 245 mV and 238 mV, before and after 10000 cyclic voltammetry scans at 100 mV s^{-1}. The Ni_3S_2/NF also show similar TOF values of 0.63 s^{-1} and 0.79 s^{-1} at the overpotential of 155 mV before and after the stability test, indicating the active sites are stable. N-Ni_3S_2/NF exhibited a slight decay of overpotentials at 10 mA cm^{-2}, from 157 mV to 174 mV before and after 10000 cycles under the same conditions. The slight decay of current was observed from the current-time curve of N doped Ni_3S_2/NF (Figure 2.17). To understand the reason for this decay, we investigated the change of areal capacitance (which is proportional to the electrochemical surface area) during the stability test and found that a 39% of the areal capacitance was lost (Figure 2.18). The result implies the electrolyte accessible surface area of N doped Ni_3S_2/NF was decreased. The reduced surface area could be due to active material lost as the N doped Ni_3S_2/NF has more loosely packed structure (Figure 2.18). Notably, the TOFs of N doped Ni_3S_2/NF still exhibit comparable values of 2.29 s^{-1} and 2.51 s^{-1} before and after the measurement, indicating the intrinsic activity of active site was retained.

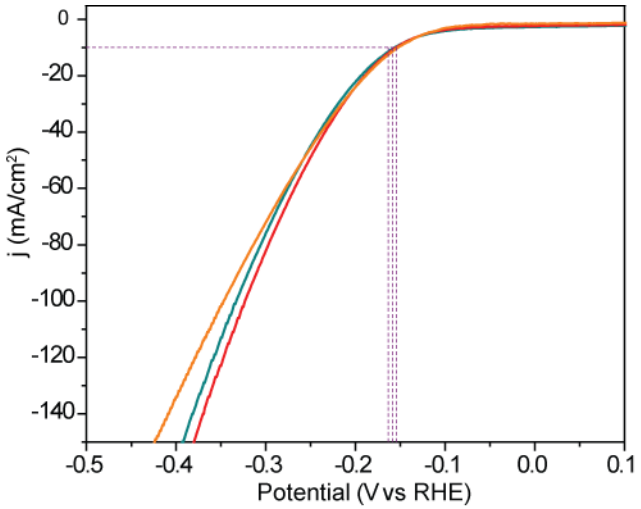

Figure 2.12 HER polarization curves collected from three different N doped Ni_3S_2 samples in 1 M KOH at a scan rate of 5 mV s^{-1}. Dashed lines highlight the potential at 10 mA/cm^2.

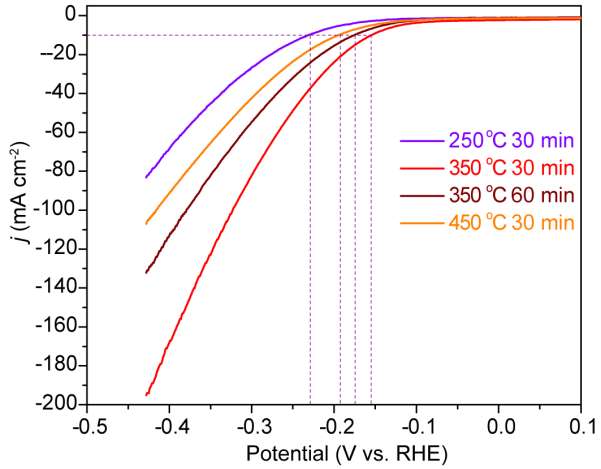

Figure 2.13 Polarization curves of Ni_3S_2 samples treated in different conditions collected in 1.0 M KOH at the scan rate of 5 mV s^{-1}.

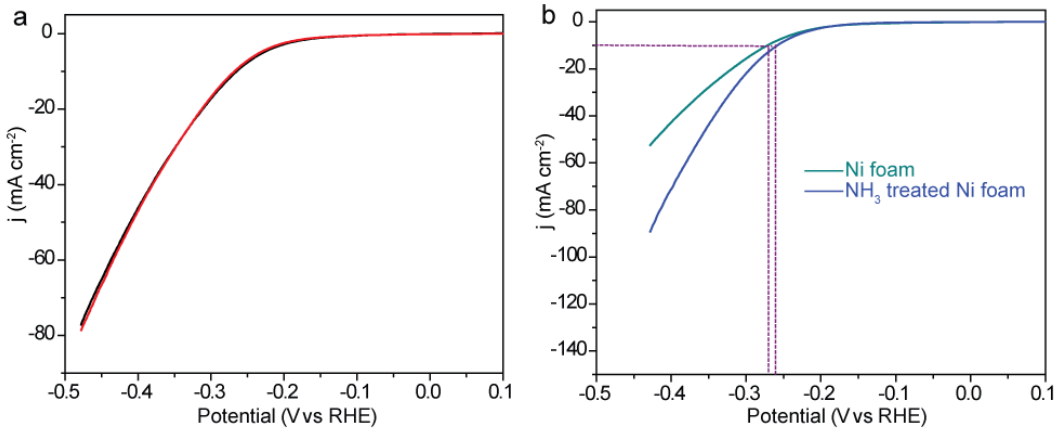

Figure 2.14 (a) HER polarization curves collected from two different bare Ni foams in 1 M KOH with a scan rate of 5 mV s^{-1}. (b) HER polarization curves of a pristine and N doped Ni foam collected in 1 M KOH with a scan rate of 5 mV s^{-1} (dashed lines highlight the potential at 10 mA/cm^2).

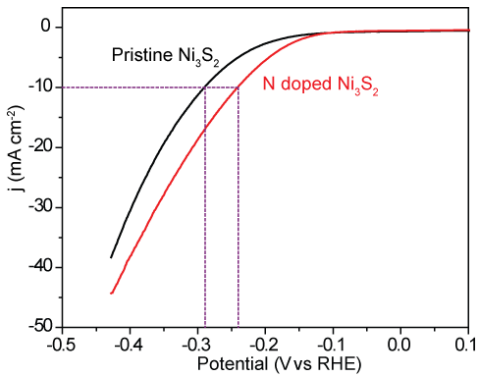

Figure 2.15 The HER polarization curves collected from pristine and N doped Ni_3S_2 samples in 1 M KOH with a scan rate of 5 mV s^{-1} (dashed lines highlight the potential at 10 mA/cm^2). The currents are normalized to the electrochemical surface area.

Table 2.1 The simulated equivalent circuit data of the NH_3 and N_2 treated samples.

Sample	R_s [Ω cm^{-2}]	R_{ct} [Ω cm^{-2}]	CPE-T	CPE-P
N_2	2.702	195.9	1.204×10^{-3}	0.8272
NH_3	2.470	35.24	2.984×10^{-3}	0.8812

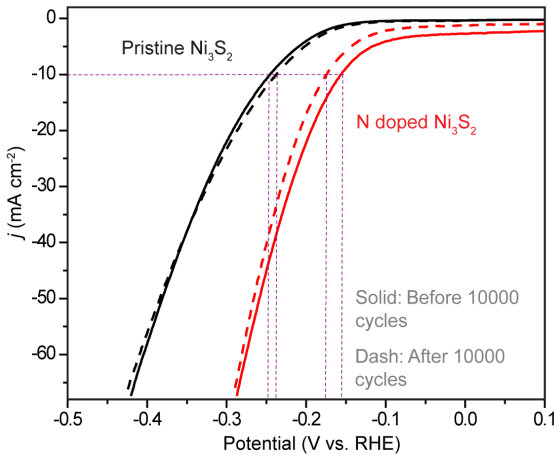

Figure 2.16 Polarization curves of Ni_3S_2/NF and N doped Ni_3S_2/NF before and after 10000 cyclic voltammetry scans at 100 mV s^{-1}.

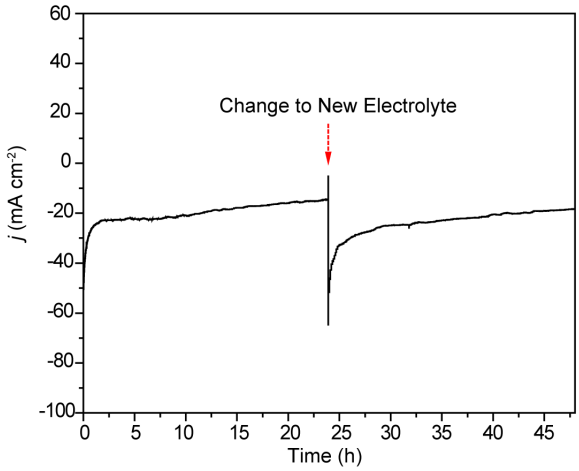

Figure 2.17 Current-time curve of N doped Ni_3S_2/NF collected at -0.28 V vs. RHE. The arrow highlights the time of replacing electrolyte.

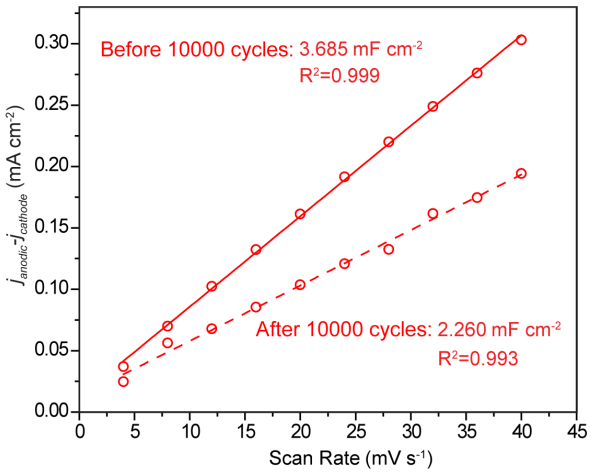

Figure 2.18 Difference of anodic current and cathodic current of N doped Ni_3S_2/NF before and after 10000 cyclic voltammetry scans at 100 mV s^{-1} is plotted as a function of scan rate.

To further investigate the activity enhancement mechanism and provide deeper understanding of the role of N doping, we performed the DFT simulation of the H adsorption on different facets and compare the thermodynamics results such as ΔG_{H^*} with those of the facets before N doping (Figure 2.19 and Table 2.2). According to the Ni-S-O Pourbaix diagram, the stable phases are Ni_3S_2 and Ni, at pH 14 and the potential window we studied (0.1V~ -0.5V vs RHE).[46] We carefully chose the stable terminations based on the computed surface phase diagrams as a function of elemental chemical potentials as shown in the supporting information. We computed the ΔG_{H^*} following the previous work which includes the solvation effect, zero-point energy and entropy contributions explicitly for both free molecules and surfaces.[47] We considered two doping concentrations (both lower and higher N doping level) in our theory study. In the lower concentration case, the N doping concentration in our surface model is one N over every eight surface S atoms at (-111) (or over nine surface S atoms at the (100) facet). The shortest distance between two N atoms is ~12 Å which is far enough to

isolate N dopants. The effect of higher doping concentration on HER activity is discussed later in this article. It has been found that the N doping has generated two types of dopant sites for possible H adsorption on (100) facet: interstitial N and substitutional N, the latter of which has a ΔG_{H^*} value of 0.036 eV, indicating it as a desirable site for HER. Additionally, the implanted substitutional and interstitial N slightly decreased the ΔG_{H^*} values of their neighboring Ni and S sites on the (100) facet, which made them more catalytically active than before. For example, the reduction of ΔG_{H^*} from 0.583 eV to 0.448 eV is confirmed on the neighboring Ni sites of the N substitutional doped (100) facet.

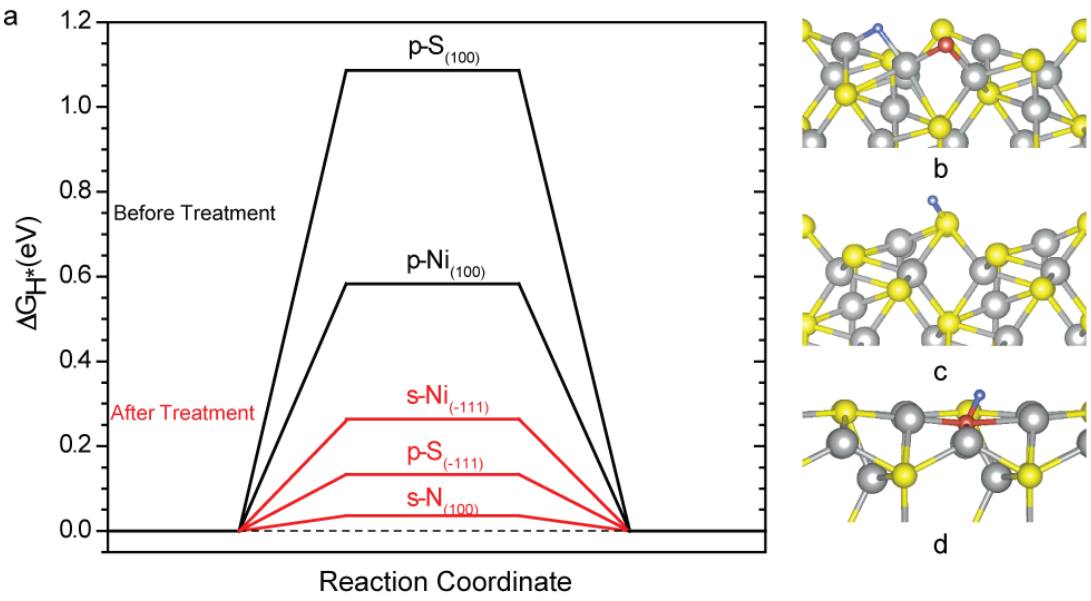

Figure 2.19 (a) Reaction energy of H adsorption, ΔG_{H^*}, displayed for sites present before (black lines) and after treatment (read lines). (b) H binding to two Ni sites (s-$Ni_{(-111)}$) on the s-(-111) surface (grey sphere represents Ni, yellow sphere represents S, blue sphere represents H, while red sphere represents N). (c) H binding to S (p-$S_{(-111)}$) on the p-(-111) surface. (d) H binding to N (s-$N_{(-100)}$) on the s-(100) surface. "p-" denotes pristine surfaces; "s-" denotes N substitutional surfaces. Notably there is a

significant improvement from the treatment with the creation of the more active sites, s-$N_{(100)}$ and p-$S_{(-111)}$.

Table 2.2 Summarized values of vibrational contributions to the free energy F_{vib}, solvation energy F_{solv}, H adsorption energy ΔE_{H^*} and H adsorption free energy ΔG_{H^*} at the room temperature 275 K for all sites present in the six types of surfaces (Surface with N doping considering only N and its nearest neighboring sites). Note that 'p' denotes pristine surfaces, 's' denotes sites near substitutional N and 'i' denotes sites near interstitial N (near implies the site is within 5 Å of doped N site).

Site	F_{vib} [eV]	F_{solv} [eV]	ΔE_{H^*} [eV]	ΔG_{H^*} [eV]
p-$S_{(100)}$	0.219	-0.200	0.910	1.086
p-$Ni_{(100)}$	0.151	-0.155	0.430	0.583
s-$S_{(100)}$	0.219	-0.206	0.807	0.985
s-$Ni_{(100)}$	0.151	-0.161	0.293	0.448
s-$N_{(100)}$	0.293	-0.200	-0.222	0.036
i-$S_{(100)}$	0.219	-0.212	0.586	0.769
i-$Ni_{(100)}$	0.151	-0.180	0.419	0.633
i-$N_{(100)}$	0.293	-0.228	-0.696	-0.455
p-$S_{(-111)}$	0.219	-0.400	-0.125	0.133
p-$S2_{(-111)}$	0.219	-0.413	0.188	0.434
p-$Ni_{(-111)}$	0.151	-0.438	0.228	0.380
s-$S2_{(-111)}$	0.219	-0.429	0.134	0.366
s-$Ni_{(-111)}$	0.151	-0.464	0.134	0.264
s-$N_{(-111)}$	0.293	-0.436	-1.110	-0.812
i-$S_{(-111)}$	0.219	-0.476	0.172	1.034
i-$S2_{(-111)}$	0.219	-0.404	0.857	0.420
i-$Ni_{(-111)}$	0.151	-0.413	0.360	0.532
i-$N_{(-111)}$	0.293	-0.419	-0.819	-0.512

In addition to the (100) facet, ΔG_{H^*} of the newly exposed (-111) facet has also been investigated. The incorporated N in (-111) facet exhibits relatively strong adsorption ability towards H, with negative values of ΔG_{H^*} about -0.812 eV on substitutional N and -0.512 eV on interstitial N. As was seen on N doped (100) surfaces, Ni and S sites neighboring (distance to N smaller than 5 Å) substitutional N on the (-111) facet (denoted as s-(-111)) are found to have smaller values of ΔG_{H^*} compared to the pristine surface p-(-111) and are closer to the target of 0 eV by 0.116 eV and 0.068 eV, respectively. Even for the Ni and S sites that are not neighboring to the doped N, the ΔG_{H^*} values of 0.380 eV for Ni (p-$Ni_{(-111)}$) and 0.133 eV for S (p-$S_{(-111)}$) in the (-111) facet are also much lower than their counterparts in pristine (100) facet, which indicates (-111) is a more active facet than (100) for pristine Ni_2S_3 surfaces. Based on the calculated results of ΔG_{H^*}, it is reasonable to conclude that the ammonia treatment has not only introduced heteroatom N dopant as the additionally new active sites (such as in (100) facet), but also created new active facet (such as (-111) facet) with lower H adsorption free energy on Ni and S sites, suggesting that the increased ECSA is effective in boosting the amount of active sites (Figure 2.19a and Table 2.2). The most favorable H adsorption sites for Ni, S and N correspond to s-$Ni_{(-111)}$, p-$S_{(-111)}$ and s-$N_{(100)}$ (Figure 2.19b-d). Among those new active sites, p-$S_{(-111)}$ and s-$N_{(100)}$ represent the most favorable H adsorption sites owing to their lowest values of $|\Delta G_{H^*}|$ (0.036 eV for s-$N_{(100)}$ and 0.133 eV for p-$S_{(-111)}$), which are possibly the 'hotspots' for vigorous HER and are therefore worth the attentions for deeper analysis of the enhanced activity.

The magnitudes of ΔG_{H^*} in the Ni_3S_2 have been found to correlate with the coordination number of the S and N sites at the surface, the change of atomic charge of

the Ni neighbors of the S and N sites at the surface compared to the Ni neighbors of S in bulk, and the relative electronegativity between S and N (dopants). The correlation of H adsorption free energy ΔG_{H^*} with the coordination of the S and N sites and the charge deficiency on surface Ni are present in Table 2.3. Note we calculated atomic charges based on both the Bader charge scheme (Table 2.3),[48] and a Lowdin charge scheme (Table 2.4), and found the trend of atomic charges as a function of doping and coordination number does not depend on the choice of charge partitioning schemes. It is straightforward to see in Table 2.3 that the lower coordination number of S (bulk S has a coordination number of 6) corresponds to the lower H adsorption free energy. This is primarily because that the coordinately unsaturated S (lower coordination number than 6) possesses more dangling bonds favorable for H binding. In addition, the electronic interaction and charge distribution between Ni and S also plays important role in determining the H adsorption free energy. The change of atomic charge of the Ni neighbors of the S and N sites at the surface compared to the ones in bulk has been used to probe this interaction. The equation of ΔQ_{Ni} (average of the difference in atomic charge of the surface Ni binding to S or N, Q_{Ni}^{surf}, and the atomic charge of bulk Ni in Ni_3S_2, Q_{Ni}^{bulk}) is shown as follows (eq. 2.6):

$$\Delta Q_{Ni} = \mathrm{Avg}\left(Q_{Ni}^{surf} - Q_{Ni}^{bulk}\right)$$

Where a value of ΔQ_{Ni} above 0 is indicative of Ni being more positively charged (electron depleted) at the surface than in bulk Ni_3S_2. From the calculated results of ΔQ_{Ni} in Table 2.3, we can find that Ni binding to the S with lower coordination number has a larger value of ΔQ_{Ni} which demonstrates that coordinately unsaturated S (more

electronegative) draws more electrons from each neighboring Ni atom and thus it becomes easier for H to share electrons with S and bind to those S sites. Substitutionally doping N to the S site leads to much higher ΔQ_{Ni} (in this case Ni is neighboring to N), accompanied by lower ΔG_{H^*} as shown in Table 2.3. This is consistent with the expectation because N has a higher electronegativity than S and is believed to significantly draw electrons from Ni as well as bind H much stronger than S at the same coordination environment.[49] However, the high electronegativity of N combined with low coordination number of 3 at (-111) facet makes the N site (s-$N_{(-111)}$) bind H too strong, which is demonstrated by the large negative ΔG_{H^*} of -0.812 eV. Meanwhile in the case of s-$N_{(100)}$, a balance of the two effects of high electronegativity and high coordination number helps to generate favorable H adsorption sites, with a coordination number of 5 and almost ideal ΔG_{H^*} value of 0.036 eV.

Table 2.3 H adsorption free energies (ΔG_{H^*}) for p-S sites and s-N sites on (100) and (-111) facets along with coordination numbers of S or N and atomic charge difference between the surface and bulk Ni atoms ($\Delta Q_{Ni,}$ using Bader charge partitioning scheme). We note the correlation of ΔG_{H^*} with the coordination number of the S/N site with Ni neighbors and the average atomic charge of Ni around S/N atoms compared to bulk Ni of these sites, ΔQ_{Ni}. Lower coordination number is accompanied by higher ΔQ_{Ni} and lower H adsorption free energy, ΔG_{H^*}. "p-" denotes pristine surfaces; "s-" denotes N substitutional surfaces.

Site	Coordination	ΔQ_{Ni}	ΔG_{H^*} [eV]
p-$S_{(100)}$	5	0.008	1.086
p-$S2_{(-111)}$	4	0.135	0.434
p-$S_{(-111)}$	3	0.136	0.133
s-$N_{(100)}$	5	0.417	0.036

s-$N_{(-111)}$	3	0.483	-0.812

Table 2.4 Collection of reaction energies for p-S sites and s-N sites on (100) and (-111) facets. We note the correlation of the reaction energy with the coordination of the site with Ni neighbors and the average Lowdin charge of Ni compared to bulk Ni of these sites, ΔQ_{Ni}. Lower coordination number is accompanied by higher ΔQ_{Ni} and lower H adsorption free energy, ΔG_{H^*}.

Site	Coordination	ΔQ_{Ni}	ΔG_{H^*} [eV]
p-$S_{(100)}$	5	0.003	1.086
p-$S2_{(-111)}$	4	0.053	0.434
p-$S_{(-111)}$	3	0.067	0.133
s-$N_{(100)}$	5	0.076	0.036
s-$N_{(-111)}$	3	0.178	-0.812

To understand the effects of higher doping concentrations, we also computed the H adsorption reaction energy in the case where two N form nearby at the surface (a shortest N-N distance ~3.1 Å, with two N over every eight surface S atoms at the (-111) facet or nine S at the (100) facet) and studied the effects on H adsorption at N and nearest neighbor Ni and S (Table 2.5 and Figure 2.20). We found that the N dopants only significantly affect the activity/H adsorption energy of the directly chemical-bonded atoms at both low and high concentrations. Higher concentrations of N on the (-111) surface results in a reduced activity on this surface due to replacing active p-$S_{(-111)}$ sites with inactive s-$N_{(-111)}$ sites. On the other hand, increased N concentrations on the (100) surface is very beneficial for the catalytic activity of the surface due to higher concentrations of active s-$N_{(100)}$ with reaction energy of nearly zero (ΔG_{H^*} = -0.007, 0.101 eV) and introducing active Ni sites (ΔG_{H^*} = 0.008 eV). Note that on the (100) surface, the H adsorption energies on S are similar among the pristine surface, the

surface with one N, and with two N substitutions: ΔG_{H^*} = 1.086 eV, 0.985 eV, and 0.927 eV; respectively (this also holds for the (-111) surface), which indicates similar activity at S sites at different N concentrations.

Table 2.5 Summarized values of $\boldsymbol{\Delta G_{H^*}}$ for a surface where two substitutional N (two N every eight surface S atoms at (-111) (or nine at the (100) facet) have formed in close proximity, to simulate the effects of higher N doping concentration (considering only N and its nearest neighbors) in comparison with the results of one N substitution. Higher concentrations on the (100) can continue to lead to even better activity for HER, yet it results in a less active (-111) surface.

Facet	# of substitutional N	ΔG_{H^*} Ni [eV]	ΔG_{H^*} S [eV]	ΔG_{H^*} N [eV]
(100)	1	0.448	0.985	0.036
(-111)	1	0.264	0.133, 0.434	-0.812
(100)	2	0.008	0.927	-0.007, 0.101
(-111)	2	0.425	0.174, 0.480	-0.796, -0.719

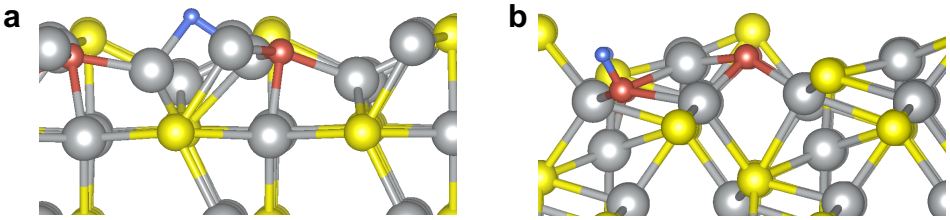

Figure 2.20 (a) Surface structure of H adsorbed to Ni on the (100) surface with a higher concentration of N. (b) Surface structure of H adsorbed to N on the (-111) surface with a higher concentration of N (grey sphere represents Ni, red sphere represents N, blue sphere represents H and yellow sphere represents S).

2.4 Conclusions

In summary, we present an effective method to activate Ni_3S_2 for HER through N doping. N doped Ni_3S_2 nanosheets exhibit a low overpotential of 155 mV at 10 mA cm^{-2} in 1.0 M KOH with an outstanding exchange current density of 0.42 mA cm^{-2}, and catalytic efficiencies (mass activity of 16.9 mA mg^{-1} and TOF of 2.4 s^{-1} at -155 mV vs. RHE). Theoretical simulation together with the experimental data concluded that the enhanced catalytic activity is due to the introduction of new active sites and more effective active facets for H adsorption. The theoretical simulation has also shown that the HER activity of Ni_3S_2 surface is highly correlated to the coordination number of surface S atoms and the charge depletion of neighbor Ni atoms, which have opposite effects on H adsorption energies (i.e. increasing the coordination number leads to higher H adsorption energies/binds H weaker, while increasing charge depletion of Ni lowers the H adsorption energies/binds H stronger). According to our calculation, the H adsorption energies were too positive at the stable pristine Ni_3S_2 surfaces, decreasing surface S coordination number through tuning elemental chemical potentials and experimental synthesis environment or atomic doping with higher electronegativity than S can potentially lead to optimal (close to zero) H adsorption energies and higher HER efficiency. These new findings not only make inexpensive Ni_3S_2 a more attractive HER catalyst, but most importantly, provide important guidance for future experimental design and synthesis of Ni_3S_2 based HER catalysts.

References

1. Li, Y.; Zhang, J. Z. *Laser Photon*. *Rev*. **2010,** *4*, 517-528.

2. Zhang, W.; Lai, W.; Cao, R. *Chem*. *Rev*. **2017,** *117*, 3717-3797.

3. Li, X.; Hao, X.; Abudula, A.; Guan, G. *J*. *Mater*. *Chem*. *A* **2016,** *4*, 11973-12000.

4. LeRoy, R. L. *Int*. *J*. *Hydrog*en *Energy* **1983,** *8*, 401-417.

5. Zeng, K.; Zhang, D. *Prog. Energy and Combust*. *Sci*. **2010,** *36*, 307-326.

6. Nørskov, J. K.; Bligaard, T.; Logadottir, A.; Kitchin, J. R.; Chen, J. G.; Pandelov, S.; Stimming, U. *J*. *Electrochem*. *Soc*. **2005,** *152*, J23-J26.

7. Xiao, P.; Chen, W.; Wang, X. *Adv*. *Energy Mater*. **2015,** *5*, 1500985.

8. Chia, X.; Eng, A. Y. S.; Ambrosi, A.; Tan, S. M.; Pumera, M. *Chem*. *Rev*. **2015,** *115*, 11941-11966.

9. Zou, X.; Zhang, Y. *Chem*. *Soc*. *Rev*. **2015,** *44*, 5148-5180.

10. Jaramillo, T. F.; Jørgensen, K. P.; Bonde, J.; Nielsen, J. H.; Horch, S. *Science* **2007,** *317*, 100-102.

11. Kong, D.; Wang, H.; Cha, J. J.; Pasta, M.; Koski, K. J.; Yao, J.; Cui, Y. *Nano Lett*. **2013,** *13*, 1341-1347.

12. Li, H.; Tsai, C.; Koh, A. L.; Cai, L.; Contryman, A. W.; Fragapane, A. H.; Zhao, J.; Han, H. S.; Manoharan, H. C.; Abild-Pedersen, F.; Nørskov, J. K.; Zheng, X. *Nat*. *Mater*. **2015,** *15*, 48.

13. Wang, H.; Kong, D.; Johanes, P.; Cha, J. J.; Zheng, G.; Yan, K.; Liu, N.; Cui, Y. *Nano Lett*. **2013,** *13*, 3426-3433.

14. Xie, J.; Zhang, H.; Li, S.; Wang, R.; Sun, X.; Zhou, M.; Zhou, J.; Lou, X. W.; Xie, Y. *Adv*. *Mat*. **2013,** *25*, 5807-5813.

15. Luo, Z.; Miao, R.; Huan, T. D.; Mosa, I. M.; Poyraz, A. S.; Zhong, W.; Cloud, J. E.; Kriz, D. A.; Thanneeru, S.; He, J.; Zhang, Y.; Ramprasad, R.; Suib, S. L. *Adv*. *Energy Mater*. **2016,** *6*, 1600528.

16. Peng, Z.; Jia, D.; Al-Enizi, A. M.; Elzatahry, A. A.; Zheng, G. *Adv*. *Energy Mater*. **2015,** *5*, 1402031.

17. Chung, D. Y.; Han, J. W.; Lim, D.-H.; Jo, J.-H.; Yoo, S. J.; Lee, H.; Sung, Y.-E. *Nanoscale* **2015,** *7*, 5157-5163.

18. Cui, Z.; Ge, Y.; Chu, H.; Baines, R.; Dong, P.; Tang, J.; Yang, Y.; Ajayan, P. M.; Ye, M.; Shen, J. *J*. *Mater*. *Chem*. *A* **2017,** *5*, 1595-1602.

19. Feng, L.-L.; Yu, G.; Wu, Y.; Li, G.-D.; Li, H.; Sun, Y.; Asefa, T.; Chen, W.; Zou, X. *J*. *Am*. *Chem*. *Soc*. **2015,** *137*, 14023-14026

20. Jiang, N.; Bogoev, L.; Popova, M.; Gul, S.; Yano, J.; Sun, Y. *J*. *Mater*. *Chem*. *A* **2014,** *2*, 19407-19414.

21. Jiang, N.; Tang, Q.; Sheng, M.; You, B.; Jiang, D.-e.; Sun, Y. *Catal*. *Sci*. *Technol*. **2016,** *6*, 1077-1084.

22. Li, J.; Shen, P. K.; Tian, Z. *Int*. *J*. *Hydrogen Energy* **2017,** *42*, 7136-7142.

23. Metcalf, P. A.; Fanwick, P.; Kąkol, Z.; Honig, J. M. *J*. *Solid State Chem*. **1993,** *104*, 81-87.

24. Ouyang, C.; Wang, X.; Wang, C.; Zhang, X.; Wu, J.; Ma, Z.; Dou, S.; Wang, S. *Electrochim*. *Acta* **2015,** *174*, 297-301.

25. Tang, C.; Pu, Z.; Liu, Q.; Asiri, A. M.; Luo, Y.; Sun, X. *Int*. *J*. *Hydrogen Energy* **2015,** *40*, 4727-4732.

26. Wu, Y.; Li, G.-D.; Liu, Y.; Yang, L.; Lian, X.; Asefa, T.; Zou, X. *Adv*. *Funct*. *Mater*. **2016,** *26*, 4839-4847.

27. Aray, Y.; Vega, D.; Rodriguez, J.; Vidal, A. B.; Grillo, M. E.; Coll, S. *J*. *Phys*. *Chem*. *B* **2009,** *113*, 3058-3070.

28. Mi, L.; Wei, W.; Huang, S.; Cui, S.; Zhang, W.; Hou, H.; Chen, W. *J*. *Mater*. *Chem*. *A* **2015,** *3*, 20973-20982.

29. Ng, K. T.; Hercules, D. M., *J*. *Phys*. *Chem*. **1976,** *80*, 2094-2102.

30. Lin, H.; Liu, F.; Wang, X.; Ai, Y.; Yao, Z.; Chu, L.; Han, S.; Zhuang, X. *Electrochim*. *Acta* **2016,** *191*, 705-715.

31. Zhu, J.; Li, Y.; Kang, S.; Wei, X.-L.; Shen, P. K. *J*. *Mater*. *Chem*. *A* **2014,** *2*, 3142-3147.

32. Wang, J.; Xu, F.; Jin, H.; Chen, Y.; Wang, Y. *Adv*. *Mater*. **2017,** *29*, 1605838.

33. Yan, M.; Pan, X.; Wang, P.; Chen, F.; He, L.; Jiang, G.; Wang, J.; Liu, J. Z.; Xu, X.; Liao, X.; Yang, J.; Mai, L. *Nano Lett*. **2017,** *17*, 4109-4115.

34. Xing, Z.; Li, Q.; Wang, D.; Yang, X.; Sun, X. *Electrochim*. *Acta* **2016,** *191*, 841-845.

35. Shalom, M.; Ressnig, D.; Yang, X.; Clavel, G.; Fellinger, T. P.; Antonietti, M. *J*. *Mater*. *Chem*. *A* **2015,** *3*, 8171-8177.

36. Chen, X.; Burda, C. *J*. *Am*. *Chem*. *Soc*. **2008,** *130*, 5018-5019.

37. Sivanantham, A.; Ganesan, P.; Shanmugam, S. *Adv*. *Funct*. *Mater*. **2016,** *26*, 4661-4672.

38. Chen, P.; Xu, K.; Tao, S.; Zhou, T.; Tong, Y.; Ding, H.; Zhang, L.; Chu, W.; Wu, C.; Xie, Y. *Adv*. *Mater*. **2016,** *28*, 7527-7532.

39. Jin, H.; Wang, J.; Su, D.; Wei, Z.; Pang, Z.; Wang, Y. *J. Am. Chem. Soc.* **2015,** *137*, 2688-2694.

40. Tian, J.; Liu, Q.; Asiri, A. M.; Sun, X. *J. Am. Chem. Soc.* **2014,** *136*, 7587-7590.

41. Lin, T.-W.; Liu, C.-J.; Dai, C.-S. *Appl. Catal. B* **2014,** *154*, 213-220.

42. Jiang, J.; Gao, M.; Sheng, W.; Yan, Y. *Angew. Chem. Int. Ed.* **2016,** *55*, 15240-15245.

43. Morales-Guio, C. G.; Thorwarth, K.; Niesen, B.; Liardet, L.; Patscheider, J.; Ballif, C.; Hu, X. *J. Am. Chem. Soc.* **2015,** *137*, 7035-7038.

44. Wu, H. B.; Xia, B. Y.; Yu, L.; Yu, X.-Y.; Lou, X. W. *Nat. Commun.* **2015,** *6*, 6512.

45. Liang, H.; Gandi, A. N.; Anjum, D. H.; Wang, X.; Schwingenschlögl, U.; Alshareef, H. N. *Nano Lett.* **2016,** *16*, 7718-7725.

46. Yan, B.; Krishnamurthy, D.; Hendon, C. H.; Deshpande, S.; Surendranath, Y.; Viswanathan, V. *Joule 1*, 600-612.

47. Ping, Y.; Nielsen, R. J.; Goddard, W. A. *J. Am. Chem. Soc.* **2017,** *139*, 149-155.

48. Yu, M.; Trinkle, D. R. *J. Chem. Phys.* **2011,** *134*, 064111.

49. Cheng, C. P.; Brown, T. L. *J. Am. Chem. Soc.* **1980,** *102*, 6418-6421.

Chapter 3

Carbon Doping Switching on the Hydrogen Adsorption Activity of NiO for Hydrogen Evolution Reaction

Abstract

Hydrogen evolution reaction (HER) is known to be more sluggish in alkaline media than in acidic media because of the additional energy required for the water dissociation step. Numerous catalysts, including NiO, that offer active sites for water dissociation have been extensively investigated for HER. Yet, the overall catalytic performance of NiO is still limited by lacking favorable H adsorption sites for hydrogen evolution. Here we demonstrate a strategy to activate NiO through carbon doping, which creates under-coordinated Ni sites. These new active sites are highly favorable for H adsorption. In addition, DFT calculations reveal that carbon dopant decreases the energy barrier of the Heyrovsky step from 1.17 eV to 0.81 eV, suggesting that the carbon also serves as a new 'hot-spot' for the dissociation of water molecule in water-alkali HER. As a result, the carbon doped NiO catalyst achieves an ultralow overpotential of 27 mV at the geometric current density of 10 mA/cm^2, and a low Tafel slope of 36 mV/dec, which represents the best performance among the state-of-the-art NiO catalysts.

3.1 Introduction

Water electrolysis represents a sustainable and environmentally friendly method to generate hydrogen fuel. Since proton rich environment is favorable for hydrogen adsorption on catalyst surface, acidic medium is preferable for hydrogen evolution reaction (HER). However, the acidic condition prohibits the use of non-platinum group

metals as catalysts. In addition, the corrosive acidic fog generated by the acidic electrolyte not only contaminates the produced hydrogen gas, but also causes severe chemical corrosion of electrolyzers.[1,2] These factors add significant cost for hydrogen generation and pose barriers for constructing large-scale electrolyzers. Alternatively, alkaline electrolytes with low vapor pressure and relatively mild chemical environment could avoid these issues. More importantly, non-platinum group metals such as Ni can be used as electrocatalyst/electrode for alkaline water electrolysis. A major challenge for alkaline water electrolysis is the requirement of an additional water dissociation step (i.e. the cleavage of the strong H-OH bond) for generating the essential H atom intermediates for HER. The high activation barrier of water dissociation makes HER very sluggish in alkaline medium.[3] For example, Pt typically exhibits two orders of magnitude lower exchange current density in alkaline solution than that in acidic solution.[4] It is therefore critical to develop alkaline HER catalysts that contain both hydrogen adsorption sites as well as water adsorption and dissociation sites.[5,6]

Transition metal oxides such as NiO are promising alkaline HER catalysts. Since Ni sites in NiO possess incompletely filled d orbitals, Ni sites was reported to serve as actives sites for water adsorption and dissociation in alkaline electrolyte.[7,8] For instance, Zhang *et al*. used NiO as a HER electrocatalyst that achieved an overpotential of 110 mV at the geometric current density (j_{geo}) of 10 mA/cm^2 (ref. [9]). Nonetheless, the performance of NiO is still not comparable to Pt based catalysts. One of the possible reasons is lack of hydrogen adsorption sites.[8] A recent effort of integrating NiO with metallic Ni, which provides hydrogen adsorption sites, has further decreased the overpotential for alkaline HER to 80 mV at j_{geo} of 10 mA/cm^2 (ref. [6]). However, the

susceptibility to oxidation of metallic Ni could affect the stability of the integrated catalyst. Moreover, given that only the Ni/NiO interface has the synergistic effect in alkaline HER, the integrated system may not be able to fully utilize the catalyst's surface area.

Alternatively, we aimed to create hydrogen adsorption sites for NiO through heteroatom doping. Herein, we report a carbon doped $Ni_{1-x}O$ that shows an impressively low overpotential of 27 mV at j_{geo} of 10 mA/cm^2 and a small Tafel slope of 36 mV/dec in KOH solution, which is comparable to the performance (14 mV at 10 mA/cm^2, 29 mV/dec) of the benchmark Pt/C catalyst. Structural analysis revealed that the carbon dopant substitutionally replaces a third-layer 6-coordinated Ni in NiO. DFT simulation further suggests that the carbon dopant distorts the local structure of NiO and decreases the coordination number of Ni. These under-coordinated Ni sites are highly favorable for hydrogen adsorption. In addition, the carbon sites serve as the "hot spots" for water dissociation with a fairly low energy barrier of 0.81 eV.

3.2 Experimental Section

Preparation of carbon doped $Ni_{1-x}O$ on NF. A piece of NF was anodized in a two-electrode system using a piece of Ni foil as the counter electrode in 0.3 M oxalic acid solution. The anodization was carried out at the temperature of -5 ^oC at a constant voltage of 50 V for 10 min. The anodized NF (nickel oxalate/NF) was then rinsed thoroughly with DI water and ethanol, successively. The anodized samples were then dried in vacuum at 100 ^oC for 1 h, and subsequently annealed in Ar atmosphere (ultrahigh purity 99.998%) at 400 ^oC for 40 min.

Structural characterizations. The morphology of $NiC_2O_4 \cdot 2H_2O$ bulk crystals and carbon doped $Ni_{1-x}O$ nanorods grown on NF were determined by scanning electron microscopy (SEM, Hitachi S-4800 II). Crystal structure and elemental mapping were characterized on the carbon doped $Ni_{1-x}O$ particle subunit through TEM (Talos F200X). The local coordination environment of C and O in carbon doped $Ni_{1-x}O$/NF was characterized by X-ray absorption spectroscopy (XAS) at the C K-edge and O K-edge, respectively. X-ray absorption spectroscopy spectra were measured on Beamline 8.0.1 at the Advanced Light Source (ALS), Lawrence Berkeley National Laboratory (LBNL). Energy resolution was set to 0.2 eV for C and O K-edge XAS spectra, respectively. All spectra were normalized to the incident photon flux with careful energy calibrations to the known reference samples. All spectra were recorded in the total electron yield (TEY) and total fluorescence yield (TEY) detection modes simultaneously in the XAS experimental chamber, which has the base pressure of better than 1.0×10^{-9} torr. In order to avoid the intensive signal interference from the NF, the powders collected from the anodization were used for XRD (Rigaku SmartLab) and XPS (Thermo Scientific ESCALAB 250Xi) analysis. Thermogravimetric analysis (TA 500 Thermoanalyze) was performed in Ar atmosphere from room temperature to 450 ^oC with a ramping rate of 10 ^oC/min.

Pt/C electrode preparation. 5 mg of the Pt/C (10 wt.% of Pt) was dispersed in the mixture of 958 μL ethanol and 20 μL of DI H_2O. 22 μL of Nafion (5 wt.%) was added as the binder. Subsequently, the mixture was sonicated for 30 min to well disperse the catalyst powders. Pt/C ink was drop cast on the glassy carbon electrode with an areal mass loading of 1 mg/cm^2 and dried in air.

Electrochemical measurement. The electrochemical performances were investigated in a three-electrode system, with Hg/HgO (1M KOH) and graphite rod as the reference electrode, and counter electrode, respectively. Before measurement, Hg/HgO reference electrode was corrected against reversible hydrogen electrode (RHE) based on the literature reported method.[10] The HER performances data were collected in nitrogen saturated 1.0 M KOH electrolyte. All of the working electrode experienced CV conditioning from 0.33 V to -0.32 V vs. RHE at a scan rate of 50 mV/s for 50 cycles to ensure the enough wetting of electrode first, followed by an LSV measurement at a scan rate of 1 mV/s. Electrochemical impedance spectroscopy (EIS) was performed at the potential of -0.15 V vs. RHE, with frequency from 100 kHz to 1 Hz and an amplitude of 5 mV. The LSV was *iR* corrected based on the EIS results. The ECSA was calculated based on a CV method. A series of CV (from 20 to 120 mV/s with an interval of 20 mV/s) were collected in a non-faradaic reaction potential window from 0.2 V to 0.1 V vs. RHE. A linear plot of the j_{anodic} - $j_{cathodic}$ versus scan rate was obtained accordingly and the slope is proportional to the ECSA. The ECSA can be calculated through the following eq. 3.1:

$$ECSA=\frac{C_{areal}\times A}{C_{ref}}$$

Where C_{areal} represents the areal capacitance (i.e. the slope of Figure 3.14), A is the geometric area of the working electrode (0.5 cm^2), and C_{ref} is the referential area capacitance of flat electrode (40 $\mu F/cm^2$).

DFT simulation. Density functional theory calculations were performed with plane-wave basis codes Quantum Espresso (QE), with exception for transition state calculations which were carried out using the plane-wave basis code Vienna Ab Initio

Simulation Package (VASP). In all calculations, Perdew-Burke-Erzenhof exchange and correlation functional with Hubbard U correction (PBE+U) was employed.[11] An effective Hubbard U value of 5.3 eV was used as reported in previous literature.[12] Ultrasoft pseudopotential from GBRV was used with a wavefunction cutoff of 40 Ry and charge density cutoff of 240 Ry.[13] In order to obtain the accurate energy barriers, Nudged Elastic Band (NEB) calculation was first performed to get the approximate saddle point, followed by the further convergence by DIMER calculation.[14, 15] The vibrational frequencies for zero point energy and entropy were computed by Density Functional Perturbation Theory (DFPT)[16] in Quantum Espresso, and an implicit solvation model[17, 18] was adopted to include the effect of solvent around solid surfaces. For the QE calculation part, ultrasoft pseudopotential with kinetic energy cutoffs of 40 Ry for wavefunction and 240 Ry for charge density is implemented. In order to capture the correct antiferromagnetic ordering of Ni along the (111) direction, a $2 \times 2 \times 2$ supercell must be used. Integration over the Brillouin zone is performed using a $4 \times 4 \times 4$ k-point mesh. In order to improve k-point integration, a cold smearing of 0.002 Ry is used. A convergence threshold of $1.0E^{-7}$ Ry on total energy is used for all self-consistency calculations. Atomic positions are relaxed until the total energy and total force converges to $1.0E^{-4}$ Ry and $1.0E^{-3}$ Ry/Bohr, respectively. The calculated lattice constant, magnetic moment and band gap are 4.22 Å, 1.64 μ_B and 2.74 eV, which agree well with previously reported theoretical values of 4.19 Å, 1.69 μ_B and 2.43 eV.[19, 20] In order to study the surface of NiO, the bulk unit cell was converted from its fcc unit cell to simple cubic unit cell, and then this cell was expanded to a $\sqrt{5} \times \sqrt{2} \times 1$ supercell for the (111) surface or a $2 \times 2 \times 1$ supercell for the (100) surface. A vacuum

region of 15 Å is added to effectively separate two adjacent slabs and avoid spurious interactions. The convergence of surface energy over the number of layers was tested and it was found that the energy difference between 5-layer slab and 7-layer slab is smaller than 1 meV/Å^2, so 5-layer slab is used. In order to mimic the properties of bulk, the bottom two layers of (111) surface were fixed with bulk positions, while the remaining structure relaxed as the surface. Due to the inversion symmetry breaking, a dipole field correction was applied along the vacuum direction. For all slab calculations, a $2 \times 2 \times 1$ k-point mesh was used with a smearing of 0.005 Ry to help the convergence. ΔG_H is the most commonly used indicator to compare the activity between different sites toward hydrogen adsorption since it correlates well with experimental exchange current densities, and an optimal hydrogen adsorption corresponds to $\Delta G_H = 0$ (too positive or negative ΔG_H leads to too weak or strong hydrogen adsorption). We calculated ΔG_H with the following eq.3.2, proposed by Nørskov et al.[21]

$$\Delta G_H = \Delta E_H + T\Delta S + \Delta ZPE + \Delta E_{solvation}$$

where, ΔE_H is the change in the total energy change after H adsorbs on the surface, $T\Delta S$ is the change of entropy, ΔZPE is the change of zero-point energy and $\Delta E_{solvation}$ is the solvation energy difference between surface with H and bare surface. The ΔG_H of all possible hydrogen adsorption sites on both surfaces have been calculated to give insights into the effect of Ni vacancy on the activity toward hydrogen adsorption. With respect to p-surface, we found that only the bridge site (i.e. H bonding with two Ni) is favorable for H adsorption with a ΔG_H value of -0.192 eV. On the other hand, for the

o-surface, in addition to Ni #1, both the exposed third layer Ni and second layer O are also possible H adsorption sites. The ΔG_H of Ni #1 exhibits a more positive value of 0.935 eV as expected as the formation of Ni vacancy ($Ni^{2+}=V_{Ni}+2h^{+}$) is accompanied with oxidization of the nearby Ni^{2+} to Ni^{3+}, making H adsorption more difficult on Ni #1. In contrast, the exposed underlayer Ni and O sites of the o-surface are more favorable for H adsorption. The hollow sites composed by three-fold third layer Ni ions give a slightly positive ΔG_H of 0.152 eV because the three-bonds configuration largely increases the interaction between Ni and H. The second layer O sites exhibit a most close to 0 value of $\Delta G_H = -0.098$ eV. However, we found that the adsorption of H_2 molecules generated in HER onto the second layer O ions are too favorable that the subsequent relax process of H_2 would cause one H strongly bonds to the O site and the other one leaves. This result suggests that the O sites could be occupied/deactivated by H_2 molecules during HER. Similar situation was not found on the Ni sites which are expected to be active during HER. Overall, o-surface doesn't increase the number of active H adsorption sites per surface area compared to that of p-surface. For the energy barrier calculation, the IS and FS for Heyrovsky step on both o-surface and C-surface were relaxed. The number of required IMs for NEB calculations was tested for the Heyrovsky reaction over o-surface and C-surface. It was found that 8 IMs and 6 IMs are enough to converge the barriers for o-surface and C-surface, respectively. After the exact saddle point was found by DIMER calculation, we did phonon calculation for all atoms in the system (except for the layers whose atoms are fixed) to check the number of imaginary frequencies in the system and confirmed there is only one imaginary

frequency, whose direction is along the reaction pathway. All these indicate that they are the real saddle points.

3.3 Results and Discussions

Hydrogen adsorption property of a HER catalyst is largely determined by its surface electronic structure and coordination geometry. Introduction of heteroatom dopant can modulate the electron density and the coordination number of active sites, and consequently adjust their hydrogen adsorption behavior. Among different dopants, carbon is particularly attractive. In a previous report of C-doped TiO_2, the addition of C dopant reduced the coordination number of Ti and increased the charge density of Ti (ref. [22]). Accordingly, we first employed density functional theory (DFT) calculations to investigate the possible impact of carbon doping on the coordination geometry of NiO. As shown in Figure 3.1, Ni is 6-coordinated in pristine NiO, whereas the C doping causes the distortion of the NiO local structure because of the mismatch of the radius and coordination number between carbon and Ni. The distortion creates enough tensile strain on the Ni-O bond and subsequently cleaves the bond. As a result, it reduces the coordination number of Ni from 6 to 3, and thus increases the charge density of Ni, where the under-coordinated Ni could potentially act as active H adsorption sites in NiO. In addition, the high affinity of carbon to oxo groups could promote water adsorption or dissociation.

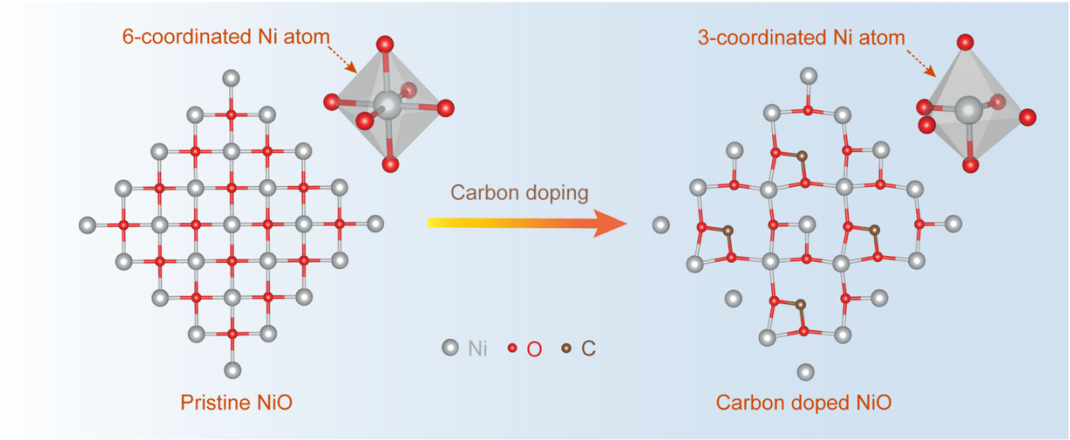

Figure 3.1 DFT calculations showing the carbon doping induced structure change of NiO (the color coding for different atoms is consistent for the whole paper).

Carbon doped NiO was prepared by a two-step process as illustrated in Figure 3.2a. Nickel oxalate dihydrate ($NiC_2O_4{\cdot}2H_2O$) bulk crystals were first uniformly grown on a Ni foam (NF) via anodization at 50 V in oxalate acid as reported elsewhere[23] (Figure 3.3). The NF coated with $NiC_2O_4{\cdot}2H_2O$ crystals was then annealed in argon ambience at 400 °C, which is considerably higher than the decomposition temperature of $NiC_2O_4 \cdot 2H_2O$ (Figure 3.4). The decomposition changed the morphology of bulk crystals to porous rod structure (Figure 3.2c and d). Transmission electron microscopy (TEM) images revealed that the rods are composed with small nanoparticle subunits (Figure 3.2e). Notably, each nanoparticle is a core-shell structure (Figure 3.2f). High resolution-TEM (HR-TEM) image collected from the edge of the nanoparticle showed lattice fringe spacings consistent with the *d*-spacings reported for (111) and (200) crystal planes of NiO (Figure 3.2g), which is also in consistency with the NiO composition in X-ray diffraction (XRD) pattern (Figure 3.4b), suggesting the shell is NiO. According to the XRD result, the core of the particle is metallic Ni. Electron energy loss spectroscopy (EELS) elemental mapping (Figure 3.2h) and line scan (inset

of Figure 3.2h) were collected from a representative nanoparticle, which also confirms the copresence of Ni and O in the nanoparticle. The intense O signal obtained at the edge of the nanoparticle again supports the proposed Ni core-NiO shell structure. Significantly, a noticeable amount of carbon signal was also present over the entire nanoparticle, indicating the successful incorporation of carbon doping.

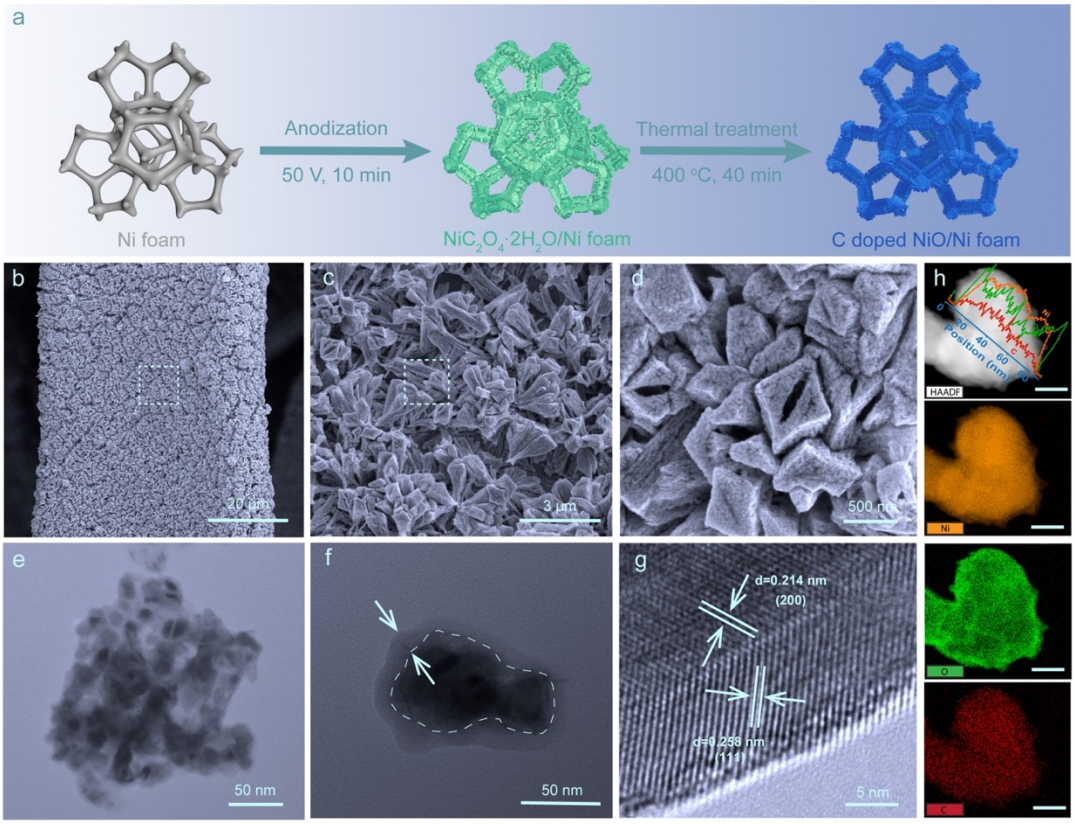

Figure 3.2 (a) Schematic illustration of the synthesis of carbon doped NiO on NF. (b-d) SEM images of the C doped NiO nanorod/NF in different magnifications. The regions highlighted by dashed boxes in (b) and (c) are magnified in (c) and (d), respectively. (e-f) TEM images of the fragments of C doped NiO nanorod/NF. (g) A HR-TEM image collected at the edge of the nanoparticle in (f). (h) High-angle annular dark field (HAADF)-TEM image of a Ni core/NiO shell particle and the corresponding EELS elemental mapping of Ni, O and C (scale bars are 20 nm).

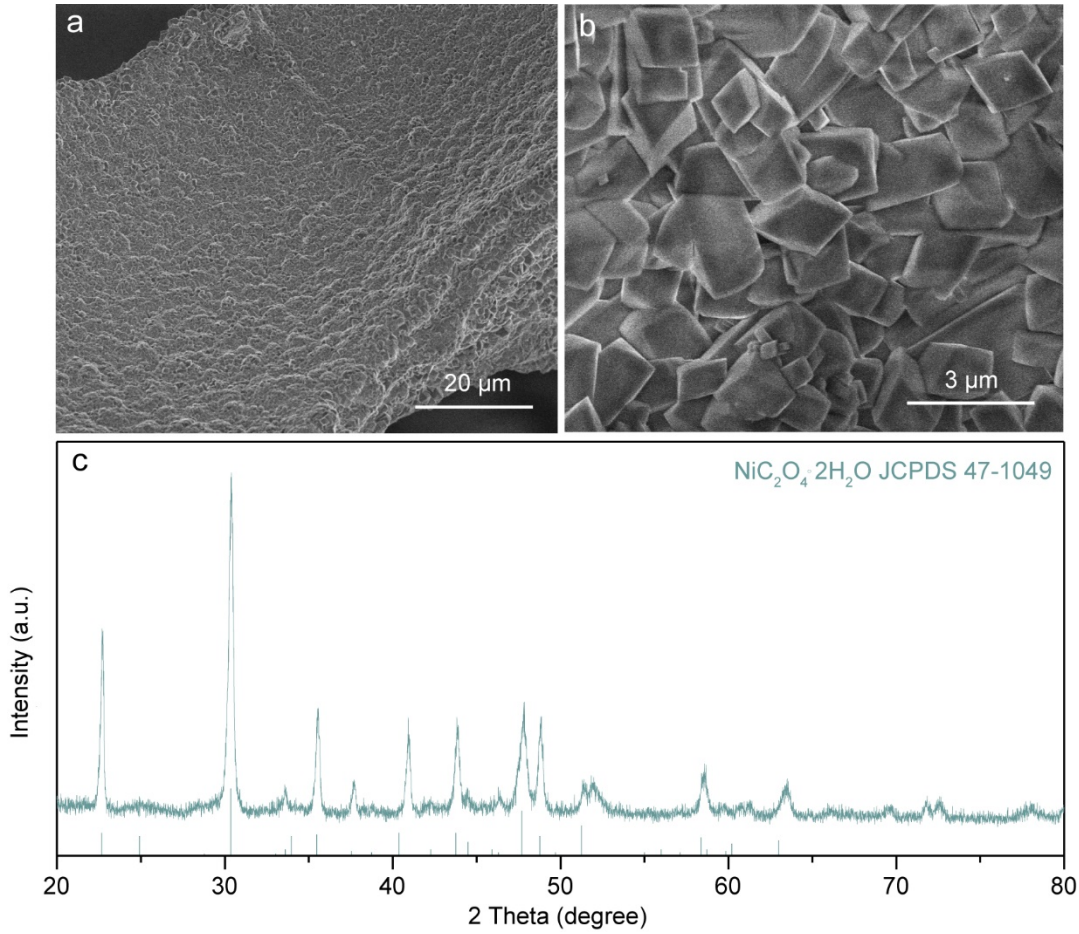

Figure 3.3 SEM images of $NiC_2O_4 \cdot 2H_2O$ grown on NF. **c**, XRD pattern of $NiC_2O_4 \cdot 2H_2O$ powder.

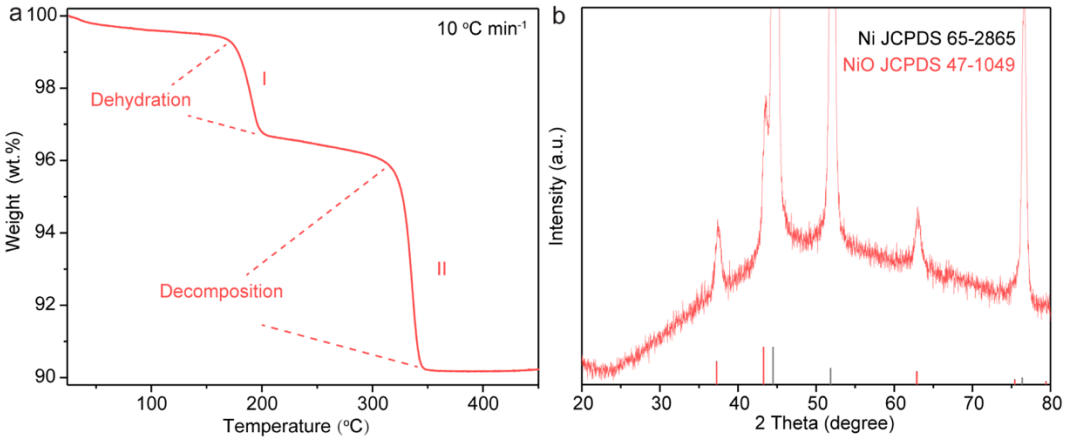

Figure 3.4 (a) Thermogravimetric analysis of the $NiC_2O_4 \cdot 2H_2O$ in argon atmosphere with a ramping rate of 10 °C/min. (b) XRD pattern obtained from the C-$Ni_{1-x}O$ powder.

X-ray photoelectron spectroscopy (XPS) measurements were performed to probe the chemical environment of each element in C doped NiO (Figure 3.5a). Ni 2p XPS spectrum exhibits two broad peaks centered at 862 (satellite peak) and 856 eV, respectively. The latter peak can be deconvoluted into three sub-peaks. The Ni 2p peak at 854.5 eV is consistent with the value reported for Ni^{2+} in NiO (ref. [24]), while the peak centered at a higher binding energy of 857.1 eV corresponds to the signal of Ni^{3+} (ref. [25,26]). It is noteworthy that we did not observe metallic Ni signal from the sample. The metallic Ni and Ni-C signals were only observed when the NiO shell was etched away by argon plasma, as evidenced by the peaks at 852.7 eV in the Ni 2p spectrum[27] and 283.3 eV in the C 1s spectrum[28] (Figure 3.6). The results are consistent with the EELS mapping and XRD results, and again confirm the Ni core/NiO shell structure. O 1s XPS spectrum also supports the presence of NiO. The deconvoluted peak located at 529.4 eV suggests O bond with Ni^{2+} (ref. [26]). In addition, the peak located at 530.9 eV is assigned to the O adjacent to Ni vacancy.[25] The presence of Ni vacancy has been reported to result in valence increase of its vicinity Ni (Ni^{3+}), which is in consistency with the peak at 857.1 eV in Ni 2p spectrum.[25] C 1s spectrum shows two peaks centered at 284.6 eV and 288.6 eV, respectively. The former peak is due to the adventitious carbon.[29] The 288.6 eV signal suggests the presence of O-C=O bond, which is in consistent with the EELS results and agrees well with the observation of the O 1s peak of O-C=O at 532.8 eV.[17] The O-C=O group creates a distinguishable coordination environment of Ni (Ni-O-C=O) in NiO, which leads to an additional signal (Ni-O-C=O) located at 855.7 eV in the Ni 2p spectrum.

We also compared the X-ray absorption near edge spectroscopy (XANES) data of NF substrate and NF decorated with thermally treated $NiC_2O_4 \cdot 2H_2O$ collected at O and C K-edge (Figure 3.5b). The O K-edge XANES of the annealed $NiC_2O_4 \cdot 2H_2O$ shows a prominent pre-peak at about 529.8 eV that corresponds to the transition between O 1s state and the hole state, which has been regarded as a characteristic signal of the Ni deficient NiO (i.e. $Ni_{1-x}O$).[30,31] The hybridization of the O 2p orbital with the Ni 4s orbital creates some unoccupied states for transitions in the NiO with energy around 537.5 eV. The presence of Ni vacancies reduces the intensity of 537.5 eV peak.[31,32] More importantly, absorption peaks between 532.7 and 535 eV (shaded region) were observed for the annealed $NiC_2O_4 \cdot 2H_2O$, which are due to the mixed transitions from O 1s to empty states of high valence Ni (Ni^{3+}), and O 1s to the $\pi^*_{C=O}$ (ref. [32,33]). NF and thermally treated $NiC_2O_4 \cdot 2H_2O$ have similar C K-edge spectra except for significantly different peak intensities at 288.6 and 290.3 eV. The carbon signals observed for NF substrate originates from adventitious carbon contamination.[34] However, the substantially higher peak intensities of the annealed $NiC_2O_4 \cdot 2H_2O$ at 288.6 and 290.3 eV are unlikely related to adventitious carbon.[35] Instead, these peaks are attributed to the transition of C 1s to π^* and σ^* state in O-C=O (ref. [36]). Taken together, the XPS and XANES results disclosed two important information. First, the NiO shell contains Ni vacancies and is Ni deficient. Second, carbon dopants are substitutionally replacing the Ni positions in $Ni_{1-x}O$. Therefore, this $NiC_2O_4 \cdot 2H_2O$ derived material is denoted as C-$Ni_{1-x}O$, and our subsequent DFT simulation was performed based on this structural model.

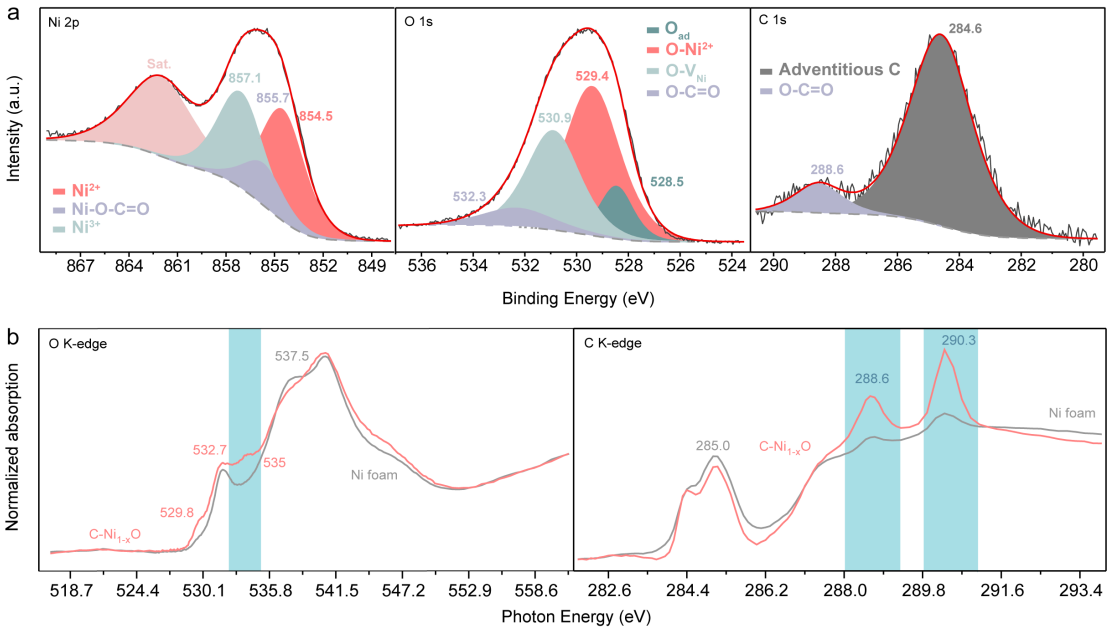

Figure 3.5 (a) Ni 2p, O 1s, and C 1s XPS spectra collected from C-$Ni_{1-x}O$ particles. The black curves are the experimental data. The red curves are the summation of the deconvoluted peaks (shaded regions). (b) O K-edge and C K-edge XANES spectra of C-$Ni_{1-x}O$ grown on NF (red curve) and NF (grey curve).

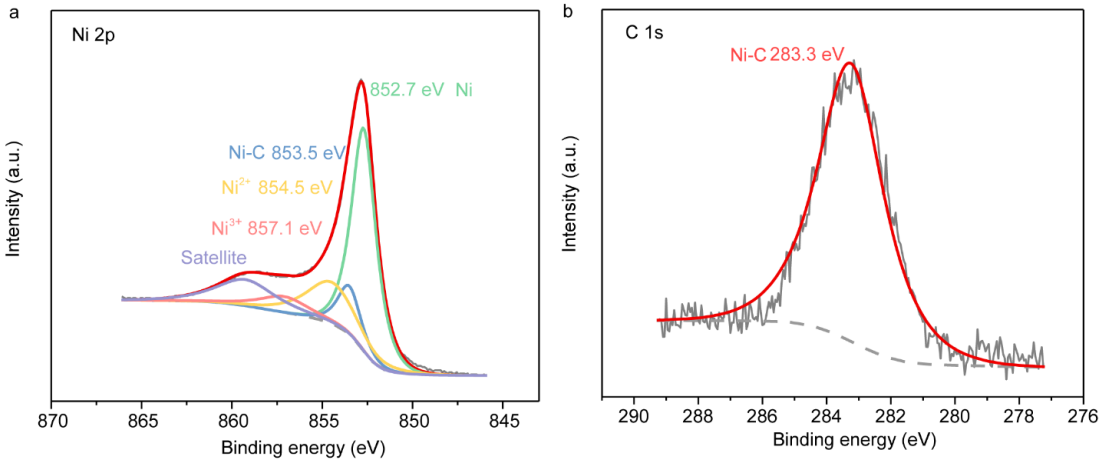

Figure 3.6 (a-b) Ni 2p and C 1s XPS of the annealed $NiC_2O_4 \cdot 2H_2O$ after argon plasma etching.

Since we observed (100) and (111) facets in the HR-TEM image collected from the $Ni_{1-x}O$ shell (Figure 3.2g), both (100) (Figure 3.7) and (111) (Figure 3.8) surface

models were built and relaxed for subsequent DFT simulation. (111) surface has two possible terminations: Ni termination and O termination. An investigation on the surface phase diagram of (111) facet shows that Ni termination is more stable than O termination in the Ni rich environment (Figure 3.9). Combined with our realistic Ni rich synthesis condition, the (111) surface should also be terminated by Ni. In addition, (111) facet tends to have surface reconstruction and the reconstructed surface is thermodynamically more stable than the pristine Ni terminated (111) (Figure 3.9). The results are consistent with the previous report on the thermodynamic stability of NiO polar (111) surface.[19] Specifically, ¾ of the outermost ions and ¼ of the second outermost ions of the pristine (111) surface (denoted as p-surface) are missing during the surface reconstruction, resulting in a new surface exposed (i.e. octopolar surface, denoted as o-surface in Figure 3.10a). Since there are more Ni ions missing compared to O ions in the surface reconstruction, Ni vacancies appear on the o-surface. As a result, high valence Ni^{3+} sites are generated to balance the charge.[25] The presence of Ni^{3+} sites is supported by XPS and XANES results. Furthermore, C substitutional doping was investigated for both (100) and o-surface. However, the only stable structure was obtained when C substitutes one third-layer 6-coordinated Ni (labeled as Ni #2 in Figure 3.10a) in o-surface. Therefore, (100) surface is not considered in further discussion. Since the bond length of C-O bond (~1.4 Å) is much shorter than that of Ni-O bond (~2.1 Å), the local structure near C substitution is strongly distorted. As a result, the O atoms that connect with C are stretched away from the corresponding top-layer Ni (labeled as Ni #1) and one Ni-O bond breaks. Consequently, the coordination number of top layer Ni decreases from 3 to 2, resulting in a new C doped surface

(denoted as C-surface, Figure 3.10b). What's interesting for the C-surface is that the three C-O bonds have the same bond length of 1.30 Å (between the bond length of C-O and C=O), the angles between three O-C=O are the same and the centered C is on the same plane with the nearby three O. The information concluded that the C forms sp^2 hybridization with three connected O, consistent with the observation of both C $1s \rightarrow \pi^*_{O-C=O}$ and $1s \rightarrow \sigma^*_{O-C=O}$ transitional signals in XANES spectra (Figure 3.5b).

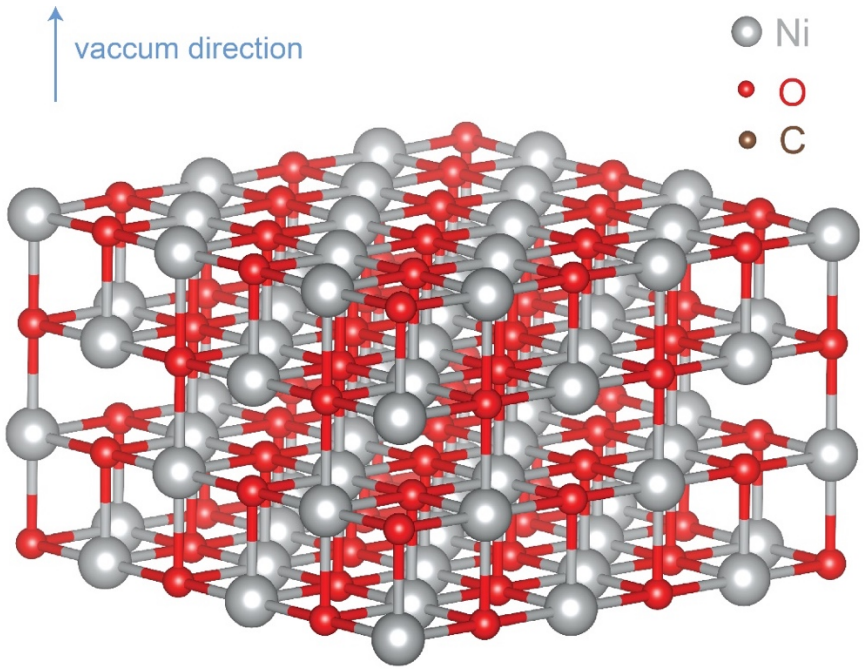

Figure 3.7 The structure of (100) surface of NiO. The vacuum's direction is given in the figure. The bottom layer is fixed (the color coding for different atoms is consistent for the whole paper).

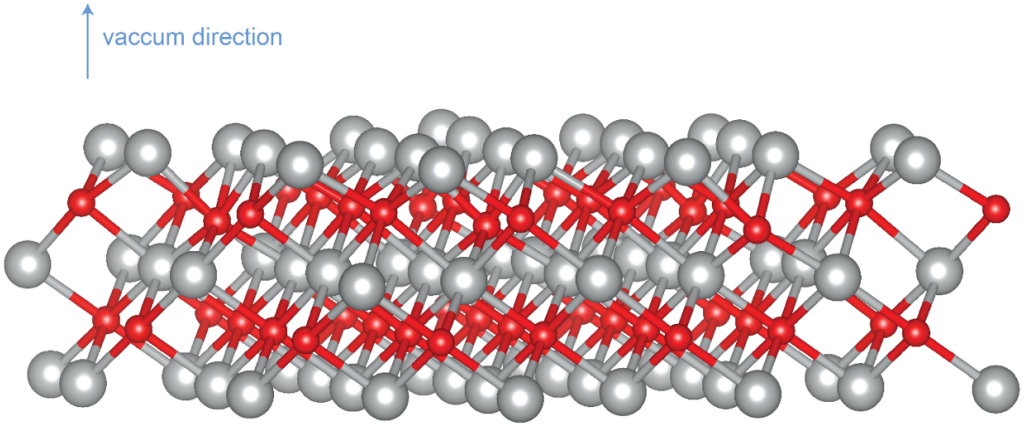

Figure 3.8 Ni terminated (111) surface of NiO. The vacuum's direction is given in the figure.

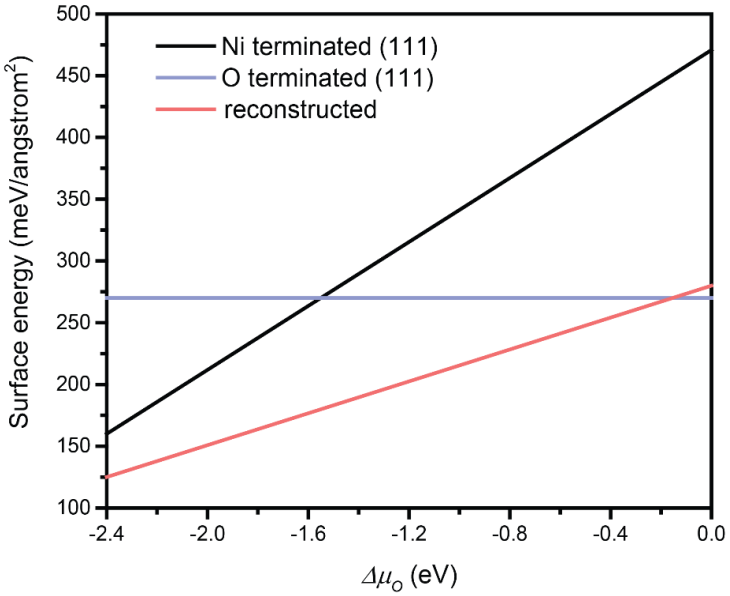

Figure 3.9 The surface phase diagram for (111) surface of NiO.

C-surface has two structural characteristics, Ni vacancy and C doping. Their effects on HER performance of NiO were studied separately. First, the investigation on Ni vacancy was made through the comparison between o-surface and p-surface, as o-surface has Ni vacancies while p-surface does not. After carefully considering all possible H adsorption sites on both surfaces, we noticed that the existence of Ni

vacancy does not increase the number of active sites toward H adsorption per unit area of the o-surface compared to p-surface (detailed information is given in SI). Then the effect of C doping was studied for both Ni vacancy resided C-surface and o-surface. It is known that the performance of catalysts is strongly related to their electronic structure, which can be tuned by dopants.[37,38] To gain an in-depth understanding of the electronic structure of C-surface, projected density of states (PDOS) of the C-surface structure were plotted, and compared to the PDOS of the o-surface (Figure 3.10c,d). The PDOS plot shows that the C doping significantly reduces the band gap from ~1.5 eV to ~0.6 eV. This indicates that the conductivity of $Ni_{1-x}O$ was improved after C doping, which is beneficial for the electron transport in HER. Further analysis revealed that the narrowed band gap is caused by the downshifting of the majority (spin up) conduction band minimum (CBM) to below the Fermi level and overlapping with valence band maximum (VBM), moving the VBM closer to the Fermi level (Figure 3.10c,d). The change of PDOS can be attributed to the C doping mediated change of the local structure of top layer Ni. One of the three Ni (#1)-O bonds in o-surface was broken owing to the strong stretch applied by the short C-O bond nearby, which endows the top layer Ni (#1') on C-surface with higher electron density, thus, upshifts the VBM. The PDOS change of the top layer Ni on o-surface (Ni #1) and C-surface (Ni #1') also confirms the effect of C doping, because the majority (spin up) CBM shifts down to below the Fermi level as well, and mixes with the VBM, resulting in the VBM upshifting to around the Fermi level (Figure 3.10e,f). The comparison of charge density mapping of the top layer Ni sites (#1 and 1') on o-surface and C-surface shows clear evidence that the electron density for the top layer Ni (#1) was largely increased after

C doping (Figure 3.10g). To quantify the charge density change of the top layer Ni (#1 and 1'), the analysis of Bader charge was performed according to the following equation (eq. 3.1)[39]

$$Q = Q_{surface} - Q_{bulk}$$

where $Q_{surface}$ is the amount of electrons carried by the surface ions, and Q_{bulk} is the amount of electrons of the corresponding ions in the bulk structure. Thus a larger Bader charge represents the higher electron density carried by the surface ion. The Bader charge for the top layer Ni (#1') from C-surface is 0.636, which is considerably larger than the value of 0.168 obtained from the Ni (#1) on o-surface, again confirming higher electron density on the top layer Ni (#1') on C-surface. The larger electron density on Ni sites is believed to be helpful for H adsorption, as Ni donates electrons to H in the Ni-H bond owing to the larger electronegativity of H (the electronegativity of Ni is 1.8, which is smaller than that of 2.1 of H).

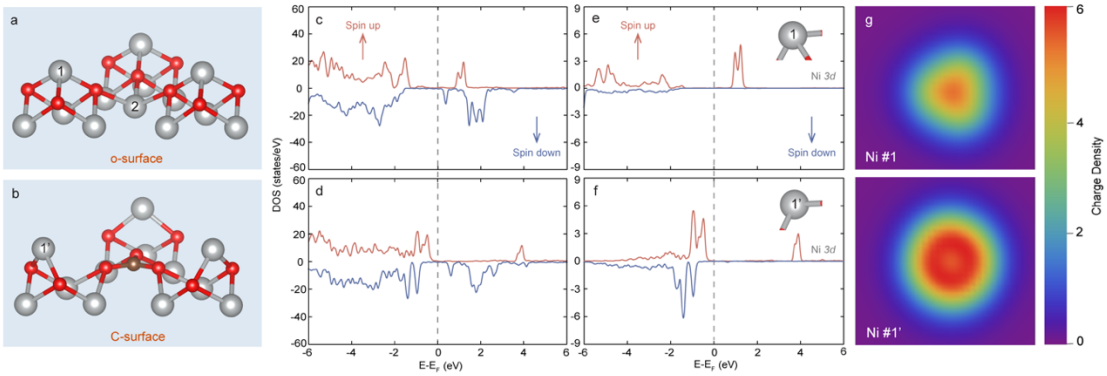

Figure 3.10 (a-b) o-surface and C-surface structures with numbers labeling different Ni sites. (c-d) PDOS plots of the Ni 3d and O 2p orbitals of the first three layers from the o-surface and C-surface. (e-f) PDOS plots of the 3d orbitals of Ni on o-surface (Ni #1) and C-surface (Ni #1'), respectively. (g) charge density mappings of the top layer Ni (#1 and 1') on o-surface (upper) and C-surface (bottom).

Compared to o-surface, carbon doping not only enhances the H adsorption activity of previously existed sites, but also exposes newly active H adsorption sites. Specifically, the improvement of H adsorption activity over old sites can be concluded by comparing the H adsorption onto single-fold sites (Ni #1 and #1') or three-fold hollow sites. For example, ΔG_H of the top layer Ni (#1') on C-surface (structure 4 in Figure 3.11) has a much smaller value of 0.282 eV than the value of 0.935 eV obtained from the identical Ni (#1) on o-surface (structure 5 in Figure 3.11), as suggested by the PDOS, the charge density mapping and Bader charge analysis. In addition, the hollow sites on C-surface (Ni # 4', 5' and 6', structure 2 in Figure 3.11) also show a smaller ΔG_H value of 0.104 eV compared to the value of 0.152 eV obtained from the identical hollow sites on o-surface (Ni # 4, 5 and 6, structure 3 in Figure 3.11). On the other hand, the newly exposed bridge sites (Ni #1' and 3', structure 1 in Figure 3.11) of the C-surface exhibit an almost thermoneutral ΔG_H value of 0.031 eV, indicating that the introduced new sites by carbon doping is favorable for the adsorption of H.

Furthermore, our analysis also showed that ΔG_H strongly depends on the Bader charge of Ni as well as the number of Ni that H bonds to. A plot of the change of ΔG_H against these two variables is depicted in Figure 3.11. The comparison between one-fold Ni sites (e.g. Ni #1' and Ni #1 in structure 4 and 5, respectively) shows that structure 4 with larger Bader charge exhibits smaller ΔG_H (0.282 eV) than structure 5 (0.935 eV). This is because the higher electron density on Ni site makes it easier for H to bind with. When the structures (e.g. structure 3 and 5) have similar Bader charges, increasing the number of Ni that H bonds to can largely shift down the ΔG_H from 0.935 eV to 0.152 eV, which is due to the stronger interaction between H and multi-fold Ni.

Similar trend was observed by comparing structure 2 with structure 5. This finding suggests that increased electron density or multi-folds of H binding sites are the underlying reasons for the easier adsorption of H on Ni sites in $Ni_{1-x}O$ system.

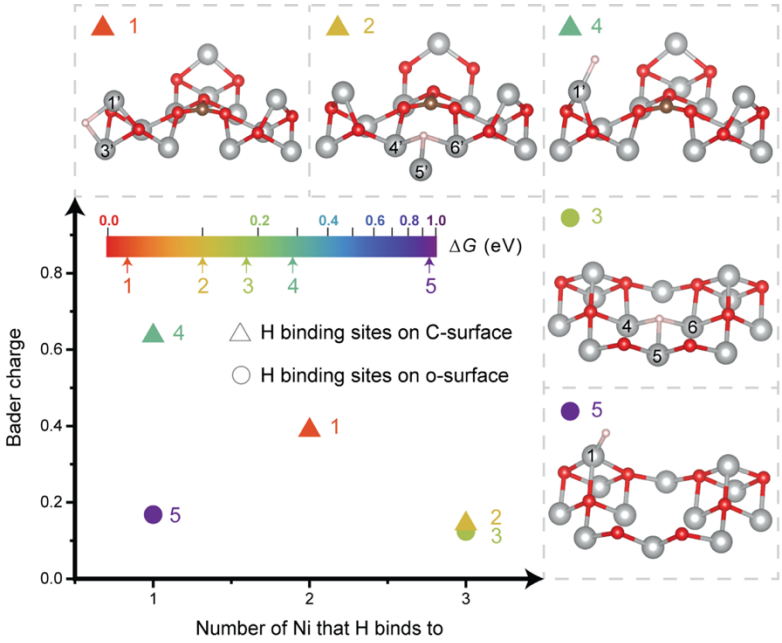

Figure 3.11 Correlation between Bader charge, number of Ni that H binds to and Gibbs free energy change of H adsorption (ΔG_H). The 5 points represent 5 different H adsorption sites on o-surface and C-surface.

The HER performances of C-$Ni_{1-x}O$ were characterized in 1.0 M KOH saturated with nitrogen through linear sweep voltammetry (LSV) at a scan rate of 1 mV/s (Figure 3.11a). NF and Pt/C (10 wt.% Pt) were also measured under the same condition for comparison. Significantly, C-$Ni_{1-x}O$ achieved an ultralow overpotential of 27 mV at the geometric current density (j_{geo}) of 10 mA/cm^2, which is comparable with the 14 mV of the benchmark Pt/C catalyst at the same current density. Figure 3.13 shows the polarization curves and statistical plot of the overpotentials obtained from 4 different

C-$Ni_{1-x}O$ samples, and they have comparable performance with an average overpotential of 29 ± 1.8 mV at j_{geo}=10 mA/cm^2. The performance comparison between NF and C-$Ni_{1-x}O$ excludes the substrate contribution to the ultralow overpotential. The total electrode activity is determined by two major factors, the intrinsic activity of the catalyst and the quantity of active sites (or the electrochemical surface area, ECSA) that is electrolyte accessible.[40] To evaluate the intrinsic activity of C-$Ni_{1-x}O$, its current was normalized to ECSA (Figure 3.12b and Figure 3.14). Importantly, C-$Ni_{1-x}O$ still showed substantially larger HER current density than that of NF at the same overpotentials. According to our DFT calculations, the excellent intrinsic activity of C-$Ni_{1-x}O$ should be a result of the improved H adsorption activity of Ni sites. In addition, Tafel plot provides important information on the rate limiting step of HER. As shown in Figure 3.12c, C-$Ni_{1-x}O$ exhibits a Tafel slope of 36 mV/dec, which is comparable with the 29 mV/dec of Pt/C but much smaller than that of NF (94 mV/dec). This small Tafel slope value suggested that the Heyrovsky step ($* H + H_2O + e^- \rightleftharpoons * H_2 + OH^-$), in which water molecules are dissociated to provide protons for the generation of dihydrogen, is the rate limiting step. The enhanced HER performances of C-$Ni_{1-x}O$ was also evidenced by the small charge transfer resistance (R_{ct}=4.03 Ω/cm^2), which is almost 27 times lower than that of NF (R_{ct}=108 Ω/cm^2), indicating the efficient electron transfer kinetics C-$Ni_{1-x}O$ during HER process (Figure 3.12d). In comparison to other Ni and NiO based HER catalysts, C-$Ni_{1-x}O$ exhibits considerably smaller overpotential (at j_{geo}=10 mA/cm^2) and Tafel slope (Figure 3.12e). Furthermore, the C-$Ni_{1-x}O$ catalyst showed excellent stability for at least 135 h (Figure 3.15). An accelerated degradation measurement was also performed through cyclic voltammetry (CV) for 10000 cycles

at a scan rate of 100 mV/s (Figure 3.12f). The total electrode activity is comparable before and after 10000 cycles, with an overpotential of 27 mV slightly increased to 32 mV at the j_{geo}=10 mA/cm^2 after the test. It is noteworthy that the intrinsic activity (j_{ECSA}) remains the same before and after the 10000 cycles (inset of Figure 3.12f).

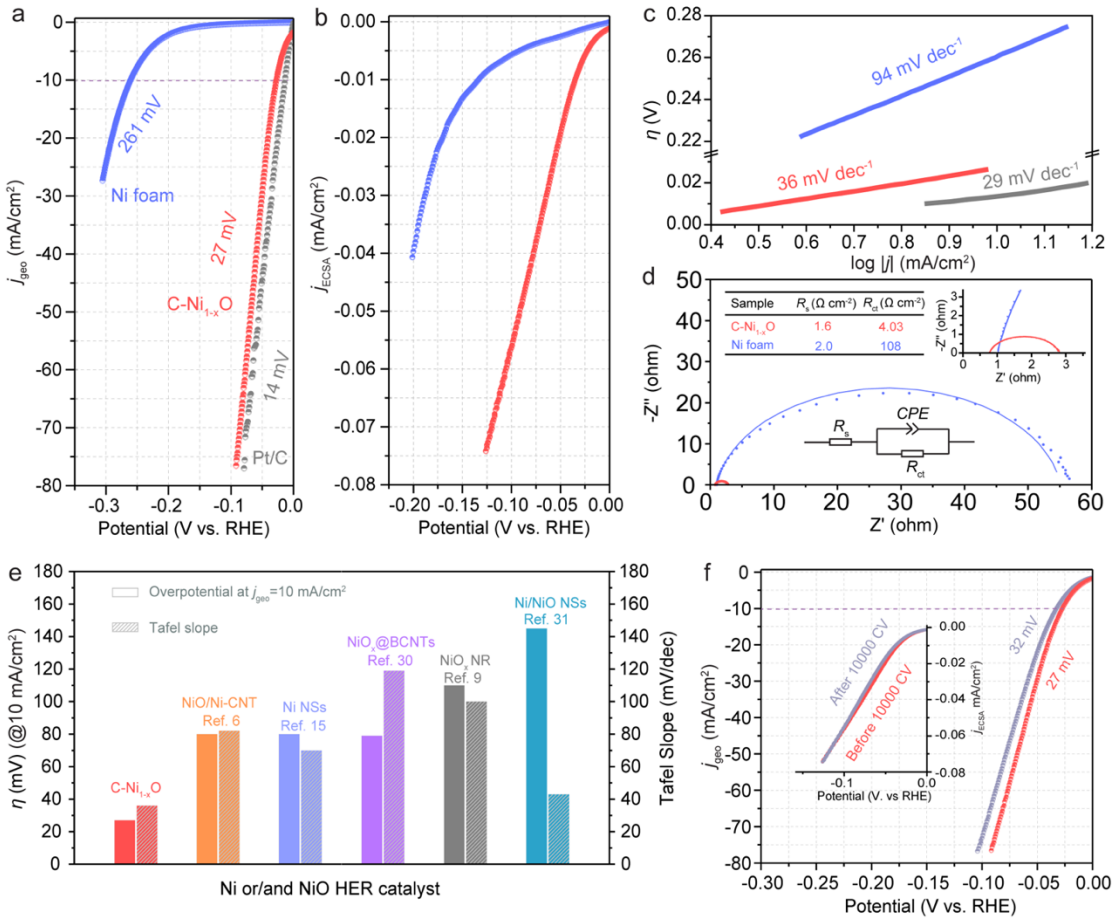

Figure 3.12 (a) HER polarization curves obtained from NF, C-Ni$_{1-x}$O and Pt/C in 1.0 M KOH saturated with nitrogen at a scan rate of 1 mV/s. (b) Polarization curves of NF and C-Ni$_{1-x}$O with current normalized to ECSA. (c) Tafel plots of the NF, C-Ni$_{1-x}$O and Pt/C. (d) Electrochemical impedance spectra of the NF and C-Ni$_{1-x}$O measured at the potential of -0.15 V vs RHE, with frequency ranging from 100 kHz to 1 Hz and an amplitude of 5 mV. Dots and solid lines are the experimental data and simulated results based on the equivalent circuit illustrated in the inset, respectively. (e) The comparison of the overpotential at 10 mA/cm^2 and Tafel slopes of C-Ni$_{1-x}$O with the reported state-of-the-art Ni and NiO based HER catalysts, including NiO/Ni-CNT[6], Ni nanosheets (NSs)[27], NiO$_x$@Bamboo-like CNTs (BCNTs)[41], NiOx nanorods (NRs)[9], and Ni/NiO NSs[42]. **f**, Polarization curves of the C-Ni$_{1-x}$O collected before and after 10000 cycles.

Inset figure shows the polarization curves with current normalized to ECSA. All of the data here are *iR* corrected.

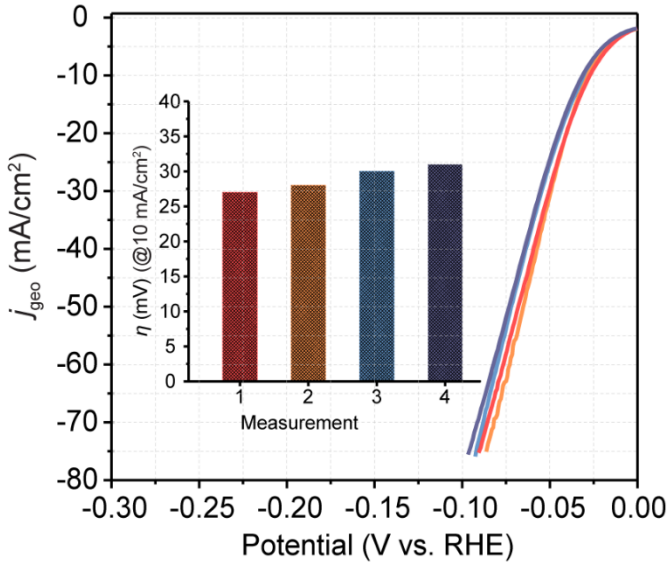

Figure 3.13 Polarization curves collected from four different C-$Ni_{1-x}O$ samples measured in the same condition at the scan rate of 1 mV/s in nitrogen saturated 1.0 M KOH (*iR* corrected). Inset is the overpotential at the j_{geo}=10 mA/cm^2 of the four samples.

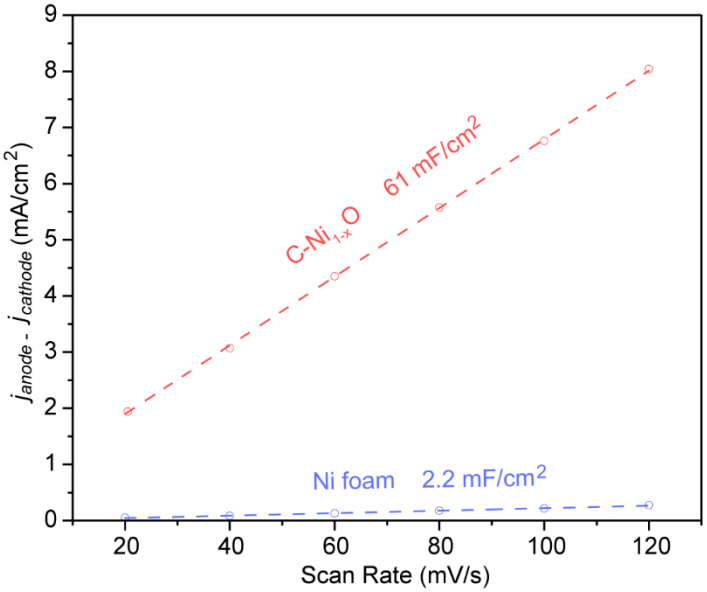

Figure 3.14 The difference of the anodic and cathodic current density difference of C-$Ni_{1-x}O$ and NF versus scan rate.

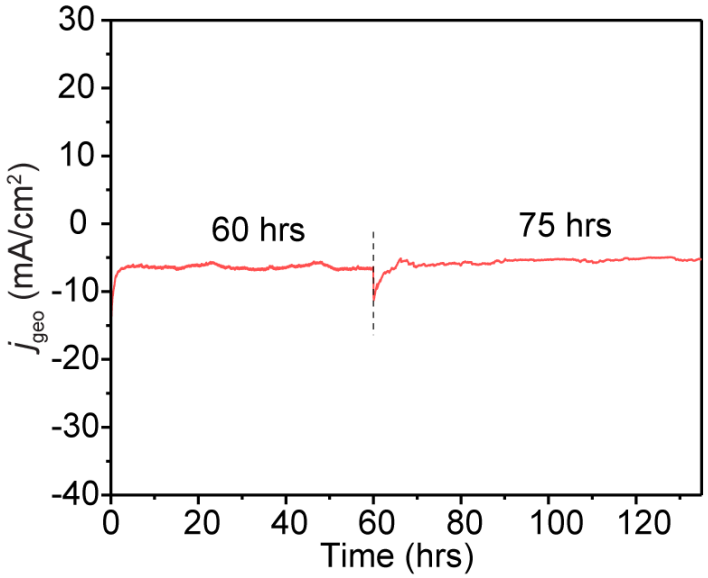

Figure 3.15 Chronoamperometry curves of the C-$Ni_{1-x}O$ samples at the potential of -32 mV vs. RHE (without *iR* correction). Dashed line represents the replacement of the electrolyte.

The Tafel plot indicates that the Heyrovsky step is the rate limiting step for C-$Ni_{1-x}O$ HER catalyst. Therefore, we performed water dissociation energy barrier calculation based on the Heyrovsky step for both o-surface and C-surface. All of the initial state (IS), transition state (TS) and final state (FS) structures for both surfaces in Heyrovsky step were shown together with their energy profile (Figure 3.16). For o-surface, initially, H_2O approached to the top layer Ni due to the Van der Waals interaction while a H atom bonds to the adsorption favorable hollow sites of the third layer Ni (Octopolar IS). Subsequently, H-OH bond was cleaved simultaneously with the formation of Ni-OH bond, which is beneficial for lowering the energy of the H_2O/o-surface system (Octopolar TS, structural details are given in Figure 3.17). The accompanied energy barrier of the Heyrovsky step on o-surface was calculated to be 1.17 eV. On the other hand, C-surface has a completely different reaction pathway. For

instance, H_2O was found to preferably stay on the top of carbon dopant through the strong affinity of carbon towards oxo groups (C doped IS). This observation is consistent with our hypothesis that carbon is a water adsorption site. H_2O was then dissociated with the assistance of the carbon dopant in the TS (structural details can be seen in Figure 3.18), which exhibits a lower activation energy barrier of 0.81 eV compared to the 1.17 eV of the o-surface. The lowered energy barrier of Heyrovsky step on C-surface could be attributed to the unique C-O3 local structure. Since the carbon dopant forms sp^2 hybridization structure with the nearby three oxygen, delocalized electrons of the π bond in this C-O3 structure increases the electron density around the carbon center. Combined with the vertical orientation characteristic of the p_z orbital of carbon dopant, it can be expected that the overlapping of the p_z orbital of carbon with the hybridized p orbital of O (in H_2O) could be facilitated, which helps form a strong C-OH bond and release more energy. This is also supported by our calculated results that the C-OH bond energy of 504 kJ/mol in TS of C-surface is higher than the 448 kJ/mol bond energy of Ni-OH in the TS of o-surface. These calculations provide important insights, for the first time, into the favorable HER reaction pathway on $Ni_{1-x}O$ and clarify that carbon dopant, due to the unique C-O3 local sp^2 hybridization structure, is the "hot-spot" for water dissociation.

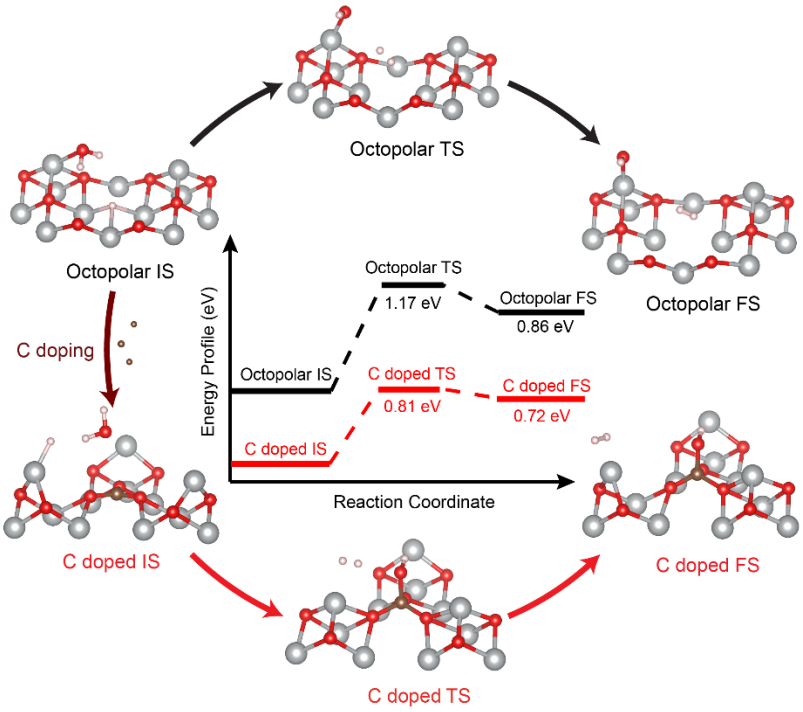

Figure 3.16 The reaction energy profile of the Heyrovsky step for o-surface and C-surface. The corresponding IS, TS and FS structures for o-surface and C-surface are listed in the surrounding circle.

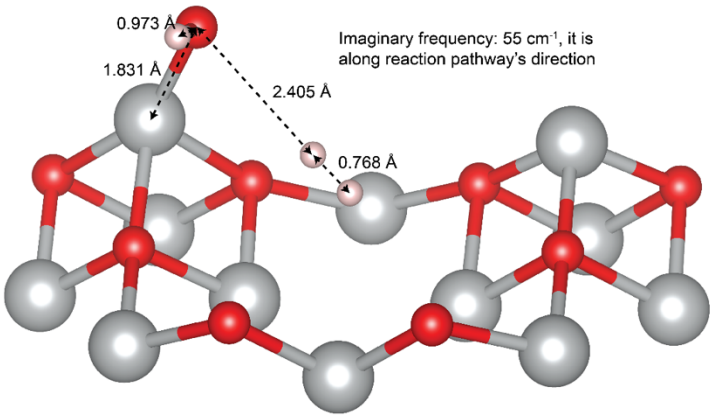

Figure 3.17 The magnified TS of o-surface. Only the first three layers' atoms are shown here.

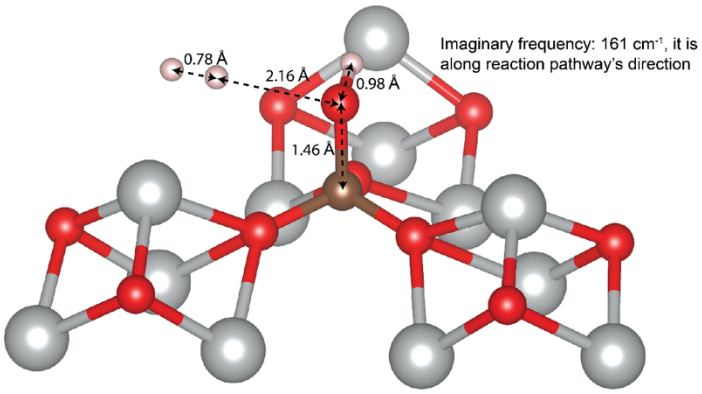

Figure 3.18 The magnified TS of C-surface. Only the first three layers' atoms are shown here.

3.4 Conclusions

In summary, we have demonstrated a new and effective NiO based catalyst for water-alkali HER. DFT simulations reveal that carbon dopant distorts the local structure of NiO and decreases the coordination number of the top layer Ni (#1). PDOS plot, charge density mapping and Bader charge analysis all indicate higher electron density around the top layer Ni (#1') on carbon doped surface, with ΔG_H calculation further confirming the top layer Ni (#1') and the nearby bridge site serving as newly exposed "hot-spots" for H adsorption. DFT calculations also showed that carbon dopant, due to the unique C-O3 local sp^2 hybridization structure, serves as an active site to facilitate the dissociation of H_2O molecule with a lower energy barrier of 0.81 eV compared to 1.17 eV of the surface without carbon doping. As a result, this carbon doped $Ni_{1-x}O$ exhibits an ultralow overpotential of 27 mV at the geometric current density of 10 mA/cm^2 and a low Tafel slope of 36 mV/dec, outperforming previously reported nickel oxide and other nickel based alkaline HER catalysts. Most importantly, this work exemplified how to activate an important water-alkali HER electrocatalyst

through rational doping. We believe these findings also provide important design guidance for other water-alkali HER electrocatalysts.

References

1. Zeng, K.; Zhang, D. *Prog*. *Energy Combust*. *Sci*. **2010,** *36*, 307-326.

2. Wang, J.; Xu, F.; Jin, H.; Chen, Y.; Wang, Y. *Adv*. *Mater*. **2017,** *29*, 1605838.

3. Trout, B. L.; Parrinello, M. *J*. *Phys*. *Chem*. *B* **1999,** *103*, 7340-7345.

4. Sheng, W.; Gasteiger, H. A.; Shao-Horn, Y. *J*. *Electrochem*. *Soc*. **2010,** *157*, B1529-B1536.

5. Gong, M.; Zhou, W.; Kenney, M. J.; Kapusta, R.; Cowley, S.; Wu, Y.; Lu, B.; Lin, M.-C.; Wang, D.-Y.; Yang, J.; Hwang, B.-J.; Dai, H. *Angew*. *Chem*. *Int*. *Ed*. **2015,** *54*, 11989-11993.

6. Gong, M.; Zhou, W.; Tsai, M.-C.; Zhou, J.; Guan, M.; Lin, M.-C.; Zhang, B.; Hu, Y.; Wang, D.-Y.; Yang, J.; Pennycook, S. J.; Hwang, B.-J.; Dai, H. *Nat*. *Commun*. **2014,** *5*, 4695.

7. Zhao, W.; Bajdich, M.; Carey, S.; Vojvodic, A.; Nørskov, J. K.; Campbell, C. T. *ACS Catal*. **2016,** *6*, 7377-7384.

8. Gong, M.; Wang, D.-Y.; Chen, C.-C.; Hwang, B.-J.; Dai, H. *Nano Res*. **2016,** *9*, 28-46.

9. Zhang, T.; Wu, M.-Y.; Yan, D.-Y.; Mao, J.; Liu, H.; Hu, W.-B.; Du, X.-W.; Ling, T.; Qiao, S.-Z. *Nano Energy* **2018,** *43*, 103-109.

10. Silva, R.; Voiry, D.; Chhowalla, M.; Asefa, T., *J*. *Am*. *Chem*. *Soci*. **2013,** *135*, 7823-7826.

11. Perdew, J. P.; Burke, K.; Ernzerhof, M. *Phys*. *Rev*. *Lett*. **1996,** *77*, 3865-3868.

12. Rohrbach, A.; Hafner, J.; Kresse, G. *Phys*. *Rev*. *B* **2004,** *69*, 075413.

13. Garrity, K. F.; Bennett, J. W.; Rabe, K. M.; Vanderbilt, D. *Comput*. *Mater*. *Sci*. **2014,** *81*, 446-452.

14. Henkelman, G.; Jónsson, H. *J*. *Chem*. *Phys*. **1999,** *111*, 7010-7022.

15. Henkelman, G.; Uberuaga, B. P.; Jónsson, H., *J*. *Chem*. *Phys*. **2000,** *113*, 9901-9904.

16. Baroni, S.; de Gironcoli, S.; Dal Corso, A.; Giannozzi, P. *Rev*. *Mod*. *Phys*. **2001,** *73*, 515-562.

17. Gunceler, D.; Letchworth-Weaver, K.; Sundararaman, R.; Schwarz, K. A.; Arias, T. A. *Model*. *Simul*. *Mater*. *Sci*. *Eng*. **2013,** *21*, 074005.

18. Ping, Y.; Nielsen, R. J.; Goddard, W. A. *J*. *Am*. *Chem*. *Soc*. **2017,** *139*, 149-155.

19. Zhang, W.-B.; Tang, B.-Y. *J*. *Chem*. *Phys*. **2008,** *128*, 124703.

20. Li, L.; Kanai, Y. *Phys*. *Rev*. *B* **2015,** *91*, 235304.

21. Nørskov, J. K.; Bligaard, T.; Logadottir, A.; Kitchin, J. R.; Chen, J. G.; Pandelov, S.; Stimming, U. *J*. *Electrochemi*. *Soc*. **2005,** *152*, J23-J26.

22. Liu, B.; Liu, L.-M.; Lang, X.-F.; Wang, H.-Y.; Lou, X. W.; Aydil, E. S. *Energy & Environ. Sci.* **2014,** *7*, 2592-2597.

23. Yang, W.; Cheng, G.; Dong, C.; Bai, Q.; Chen, X.; Peng, Z.; Zhang, Z. *J*. *Mater*. *Chem*. *A* **2014,** *2*, 20022-20029.

24. Grosvenor, A. P.; Biesinger, M. C.; Smart, R. S. C.; McIntyre, N. S. *Surf*. *Sci*. **2006,** *600*, 1771-1779.

25. Tomellini, M. *J. Chem. Soc., Faraday Trans. 1* **1988,** *84*, 3501-3510.

26. Sasi, B.; Gopchandran, K. G. *Nanotechnology* **2007,** *18*, 115613.

27. Hu, C.; Ma, Q.; Hung, S.-F.; Chen, Z.-N.; Ou, D.; Ren, B.; Chen, H. M.; Fu, G.; Zheng, N. *Chem 3*, 122-133.

28. Romanyuk, O.; Varga, M.; Tulic, S.; Izak, T.; Jiricek, P.; Kromka, A.; Skakalova, V.; Rezek, B. *J. Phys. Chem. C* **2018,** *122*, 6629-6636.

29. Marton, D.; Boyd, K. J.; Al-Bayati, A. H.; Todorov, S. S.; Rabalais, J. W. *Phys. Rev. Lett.* **1994,** *73*, 118-121.

30. Zhang, J. Y.; Li, W. W.; Hoye, R. L. Z.; MacManus-Driscoll, J. L.; Budde, M.; Bierwagen, O.; Wang, L.; Du, Y.; Wahila, M. J.; Piper, L. F. J.; Lee, T. L.; Edwards, H. J.; Dhanak, V. R.; Zhang, K. H. L. *J. Mater. Chem. C* **2018,** *6*, 2275-2282.

31. Sugiyama, I.; Shibata, N.; Wang, Z.; Kobayashi, S.; Yamamoto, T.; Ikuhara, Y. *Nat. Nanotechnol.* **2013,** *8*, 266.

32. Liu, Z.-H.; Broughton, J. *Phys. Rev. B* **1989,** *40*, 571-577.

33. Urquhart, S. G.; Ade, H. *J. Phys. Chem. B* **2002,** *106*, 8531-8538.

34. Mangolini, F.; McClimon, J. B.; Rose, F.; Carpick, R. W. *Anal. Chem.* **2014,** *86*, 12258-12265.

35. Brandes, J. A.; Wirick, S.; Jacobsen, C. *J. Synchrotron Rad.* **2010,** *17*, 676-682.

36. Kuznetsova, A.; Popova, I.; Yates, J. T.; Bronikowski, M. J.; Huffman, C. B.; Liu, J.; Smalley, R. E.; Hwu, H. H.; Chen, J. G. *J. Am. Chem. Soc.* **2001,** *123*, 10699-10704.

37. Kou, T.; Smart, T.; Yao, B.; Chen, I.; Thota, D.; Ping, Y.; Li, Y. *Adv. Energy Mater.* **2018,** *8*, 1703538.

38. Wu, Y.; Liu, X.; Han, D.; Song, X.; Shi, L.; Song, Y.; Niu, S.; Xie, Y.; Cai, J.; Wu, S.; Kang, J.; Zhou, J.; Chen, Z.; Zheng, X.; Xiao, X.; Wang, G. *Nat*. *Commun*. **2018,** *9*, 1425.

39. Henkelman, G.; Arnaldsson, A.; Jónsson, H. *Comput*. *Mater*. *Sci*. **2006,** *36*, 354-360.

40. Kou, T.; Wang, S.; Hauser, J. L.; Chen, M.; Oliver, S. R. J.; Ye, Y.; Guo, J.; Li, Y. *ACS Energy Lett*. **2019**, *4*, 622-628.

41. Wang, J.; Mao, S.; Liu, Z.; Wei, Z.; Wang, H.; Chen, Y.; Wang, Y. *ACS Appl*. *Mater*. *Interfaces* **2017,** *9*, 7139-7147.

42. Yan, X.; Tian, L.; Chen, X. *J*. *Power Sources* **2015,** *300*, 336-343.

Chapter 4

Ni Foam Supported Fe-doped β-$Ni(OH)_2$ Nanosheets Shows Ultralow Overpotential for Oxygen Evolution Reaction

Abstract

Oxygen evolution reaction (OER) involves multiple electron transfer processes, resulting in a high activation barrier. Developing catalysts with low overpotential and high intrinsic activity towards OER is critical but challenging. Here we report a major advancement in decreasing the overpotential for oxygen evolution reaction. Ni foam supported Fe-doped β-$Ni(OH)_2$ nanosheets achieve an overpotential of 219 mV at the geometric current density of 10 mA cm^{-2}. To our knowledge, it is the best value reported for Ni- or Fe hydroxide-based OER catalysts. In addition, the catalyst yields a current density of 6.25 mA cm^{-2} at the overpotential of 300 mV when it is normalized to the electrochemical surface area of the catalyst. This intrinsic catalytic activity is also better than the values reported for most of the state-of-the-art OER catalysts at the same overpotential. The good performance of the catalysts should be due to the following structural and compositional merits. For instance, the porosity of the Ni foam and nanosheets network not only increases the electrochemical surface area, but also offers oxygen gas bubble release channel to avoid the physical barrier for the electrolyte diffusion. The surface heterogeneity between amorphous and crystal structure usually makes the boundary rich of under-coordinated sites for preferential adsorption of the OER intermediates. Fe doping was proved theoretically to have electron-withdrawing effect on Ni and make Ni show an appropriate metal-OH bond strength.

4.1 Introduction

Electrolysis of water is one of most efficient and environmentally friendly methods to generate hydrogen gas, a chemical fuel with ultrahigh gravimetric energy density. High-efficiency, low-cost and stable catalysts are required for both cathode and anode to reduce the activation energy barriers for hydrogen and oxygen evolution reactions. Significant advances have been made lately in developing high-efficiency hydrogen evolution reaction (HER) catalysts, which are routinely reported to have overpotentials around or below 150 mV at j_{geo} (current density normalized to the geometric area of the electrode) of 10 mA/cm^2.[1-4] In comparison to HER that involves only two-electron transfer processes, oxygen evolution reaction (OER) taking place on the anode is a four-electron transfer process in which the multi-step elementary reactions create significant energy barriers.[5,6] As a result, most catalysts typically have high overpotentials close to or larger than 300 mV at j_{geo}=10 mA/cm^2,[5] which poses a major limitation to the overall efficiency of water electrolysis. Further reduction of OER overpotential is therefore the key to high efficiency water splitting. Constructing an efficacious OER interface through catalysts design is critical in largely boosting the reaction kinetics. Classical IrO_x and RuO_2 are the benchmark OER catalysts with decent performances with overpotential typically close to 350 mV at 10 mA/cm^2.[7-9] Yet, their scarcity and inferior stability at higher anodic potentials are the primary concerns.[10,11] Here we seek to develop an inexpensive, potent and robust OER catalysts.

First-row transition metals such as Ni and Fe are earth abundant and low cost materials. More importantly, they tend to have suitable chemical bond strength with catalytic reaction intermediates due to their unique 3d electronic structures, and thus,

appealing for heterogeneous catalytic reactions including OER.[12] Previous studies have shown that the bond strength of metal-OH is one of the key factors determine OER activity in alkaline media.[13] Either too strong or too weak bond strength results in inferior performance according to the volcano plot. Ni and Fe are located at the opposite sides of the volcano plot, and therefore the combination of Ni and Fe are anticipated to be beneficial for achieving a balanced metal-OH bond strength.[13] Enormous efforts have been devoted to developing various types of NiFe OER catalysts. For example, NiFe-layered double hydroxide with abundant oxygen vacancies was found to be effective in reducing the adsorption energy barrier of OH, and achieved a low overpotential of 250 mV at j_{geo} of 10 mA/cm^2.[14] Fe doped crystalline β-Ni(OH)$_2$ nanoparticles were able to achieve a similar overpotential at 260 mV at j_{geo} of 10 mA/cm^2, suggesting the critical role of Fe in mediating the OER activity of Ni hydroxide.[15] Albeit the enormous progress in making better OER catalysts, it is always desirable while challenging to further decrease the OER overpotential and increase the total electrode activity of inexpensive NiFe catalysts. Total electrode activity is determined by both the catalyst's intrinsic activity and electrochemical surface area (ECSA). Increasing ECSA or catalyst mass loading can often boost the total electrode activity when it is normalized to the electrode's geometric area, j_{geo}. Nevertheless, it makes difficult to compare the catalytic activity of different catalysts when they have different ECSAs and loadings. It is therefore critical to report the catalytic activity by normalizing the electrical current to ECSA (i.e., j_{ECSA}) for fair evaluation and comparison of the intrinsic activity of catalysts.[16] Total electrode activity (geometric current density, j_{geo}) should be enhanced via improving the intrinsic activities (current

density per unit of electrochemical surface area, j_{ECSA}) of catalyst, rather than increasing the mass loading of catalyst.[7,17]

Two-dimensional materials have drawn particular attention in heterogeneous catalysis owing to their large reactants accessible surface area.[18,19] Here we present a facile hydrothermal method of functionalizing Ni foam with Fe doped β-$Ni(OH)_2$ nanosheets for OER. These nanosheets achieve an outstanding overpotential of 219 mV at j_{geo} of 10 mA/cm^2, which is the best value reported for Ni hydroxide based OER catalysts at the same current density. Moreover, the j_{ECSA} of 6.25 mA/cm^2 at 300 mV obtained from the catalyst is also among the best reported values. Taken together, these results show that the incorporation of Fe is effective in improving the overpotential and the intrinsic activity of Ni based catalysts.

4.2 Experimental Section

Synthesis of Fe-incorporated β-$Ni(OH)_2$. Iron (III) nitrate nonahydrate (Strem Chemicals) was dissolved in deionized water (12 ml) under vigorous stirring until the solution became clear. Nickel foam was sonicated in acetone, 3M HCl, DI H_2O, and ethanol successively. Clean and dry nickel foam (1.5 cm × 3.0 cm) mixed with the iron nitrate solution were transferred into a Teflon-lined stainless autoclave. The hydrothermal reaction was carried out at 150 °C for 5 h. Subsequently, the autoclave was cooled down at room temperature. Vertically aligned Fe-incorporated β-$Ni(OH)_2$ nanosheets were obtained on the Ni foam substrate. The Fe-incorporated β-$Ni(OH)_2$ was rinsed with deionized water and ethanol, and dried in vacuum at room temperature. A series of Fe-doped β-$Ni(OH)_2$ samples were prepared under the same hydrothermal

conditions using different amount of iron (III) nitrate nonahydrate (0, 1.8mg, 3.6mg and 7.2 mg), they are denoted as Ni-Fe-0, Ni-Fe-1, Ni-Fe-2 and Ni-Fe-3.

Catalysts Characterizations. The phase compositions of the catalysts were characterized by x-ray diffraction (XRD, Rigaku SmartLab, operated at 40 kV and 44 mA, parallel beam mode, λ=1.54 Å, step size 0.01 degree and scan rate 1 degree/min). Morphological and crystal structures were investigated through scanning electron microscope (SEM, Hitachi S-4800 II) and transmission electron microscope (TEM, FEI Titan). To survey the local structure and surface elemental chemical valence micro-focused Ni and Fe K-edge X-ray absorption spectroscopy (XAS) data were collected in ambient conditions at ALS bending magnet beamline 10.3.2 (2.1-17 keV) with the storage ring operating at 500 mA and 1.9 GeV. Ni and Fe K-edge XAS spectra were recorded in fluorescence mode by continuously scanning the Si (111) monochromator (Quick XAS mode) from 98.93 eV below up to 771.45 eV above the Ni K-edge (8232.56-9102.94 eV, i.e., up to k = 14 $Å^{-1}$), and 22.79 eV below up to 151.62 eV above the Fe K-edge (7087.96-7262.37 eV), respectively. Fe spectra were calibrated using an Fe foil in transmission mode, with first derivative set at 7110.75 eV, Ni data were calibrated using a Ni foil in transmission mode with first derivative set at 8331.49 eV. All spectra were recorded using a beam spot size of 7 μm × 3 μm were deadtime-corrected, deglitched and calibrated using LabVIEW custom software available at the beamline. The obtained XAS data were fitted through EXAFS scattering paths simulations (Artemis Demeter version 0.9.24, with k range from 2 to 14 $Å^{-1}$, k weight of 2). Both k-space and Fourier transformed R-space data were obtained by a consistent methodology of background subtraction.

Electrochemical Measurement. The electrochemical measurements were carried out in a three-electrode system through the electrochemical workstation (CHI 660D). Hg/HgO was used as the reference electrode and carbon rod as the counter electrode. OER performances were measured through performing linear sweep voltammetry (LSV, scan rate of 1 mV s^{-1}) in O_2 saturated KOH (1.0 M) solution. All of the measured potentials (vs. Hg/HgO) were converted to the potentials against the reversible hydrogen electrode (RHE). Prior to the measurement, cyclic voltammograms (CV, -0.309 V to 0.491 V vs. RHE) were carried out at a scan rate of 20 mV s^{-1} for 20 cycles. The ECSA was characterized according to a CV method. Specifically, CV (12 to 48 mV s^{-1} at an interval of 4 mV s^{-1}) were collected in a narrow potential window of -0.717 V to -0.817 V vs RHE) where no faradaic reactions occurred. A linear relationship was obtained between J_{anodic}-$J_{cathodic}$ (at -0.767 V vs RHE) and scan rate, in which the slope is proportional to the electrochemical surface area. The ECSA was calculated according to the following eq4.1:

$$ECSA=\frac{C_{area}\times A}{C_{ref}}$$

where C_{area} is the areal capacitance obtained from the slope of Figure 4.5c, A is the geometric area of the electrode (0.35 cm^2 in our case), C_{ref} is the referential areal capacitance of flat electrode (80 μF/cm^2 is used as suggested by the ref.[20]). We have added the calculation details in the revised experimental section. Electrochemical impedance spectroscopy (EIS) was carried out at 0.6 V versus RHE with frequencies starting from 100 kHz to 1 Hz (amplitude of 5 mV). The *iR* corrections were performed based on EIS data.

4.3 Results and Discussions

The synthesis of Fe-doped β-$Ni(OH)_2$ nanosheets is illustrated in Figure 4.1a. Ni foam serves both as the substrate as well as the Ni source for the growth of $Ni(OH)_2$ nanosheets. The excellent electrical conductivity of Ni makes it a good current collector.[21] Its high porosity is also favorable for the diffusion of electrolytes and gas evolution during OER process. Ni foam hydrothermally treated in iron (III) nitrate nonahydrate for 5 hours at 150 °C results in an uniform coverage of vertically aligned nanosheets (Figure 4.1b), which are characterized to be β-$Ni(OH)_2$ (Figure 4.2). The as-synthesized nanosheets were further treated by cyclic voltammetry conditioning (experimental section) in 1.0 M KOH to improve the wetting of electrode surface. The phase and chemical composition of β-$Ni(OH)_2$ were remained unchanged after CV conditioning (Figure 4.2), while the flat nanosheets were turned into crumpled structures (Figure 4.1c-d). This morphological change is believed to be due to the intercalation/deintercalation of ions (such as K^+ in the electrolyte) into the layered β-$Ni(OH)_2$ structures during CV conditioning. Transmission electron microscopy (TEM) images revealed that the β-$Ni(OH)_2$ nanosheet is a mixture of crystallized and amorphous structure (Figure 4.1e-g). The interpenetrated crystallized and amorphous structures create kink sites enriched boundaries on which the under-coordinated atoms are generally known for facilitating adsorptions.[22,23] The inter-spacings of the observed lattice fringes are consistent with the *d*-spacing of (002) and (101) crystal planes of β-$Ni(OH)_2$. Elemental mapping data confirmed the uniform distribution of Ni, Fe and O in the entire nanosheet (Figure 4.1h), indicating the successful incorporation of Fe into the β-$Ni(OH)_2$ structures. The Fe concentration can be controlled by adjusting the

amount of Fe precursor, as shown in Table 4.1. Four Fe-doped β-$Ni(OH)_2$ samples were prepared under the same hydrothermal conditions using different amount of iron (III) nitrate nonahydrate (0 mg, 1.8 mg, 3.6 mg and 7.2 mg), they are denoted as Ni-Fe-0, Ni-Fe-1, Ni-Fe-2 and Ni-Fe-3, respectively. Notably, adjusting the amount of Fe precursor change neither the morphology nor crystal phase of β-$Ni(OH)_2$ (Figure 4.3).

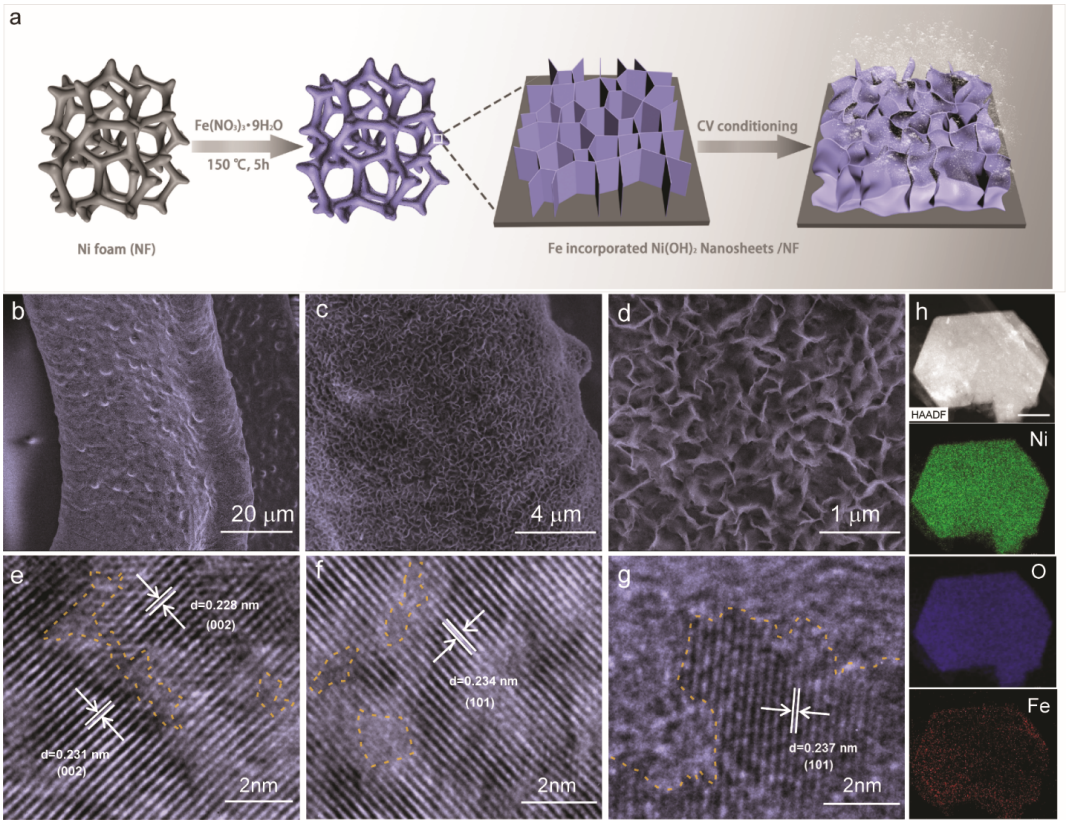

Figure 4.1 (a) Schematic illustration of the synthesis of Fe-doped $Ni(OH)_2$ nanosheets/NF. (b-d) Scanning electron microscopy (SEM) images of the Fe-$Ni(OH)_2$ nanosheets/NF. (e-g) High resolution TEM images obtained from a Fe-$Ni(OH)_2$ nanosheet. Dashed lines highlight the edge of the interrupted lattice. (h) High angle annular dark field-TEM image of a Fe-$Ni(OH)_2$ nanosheet and the corresponding elemental mapping image of Ni, Fe, and O. Scale bar is 100 nm.

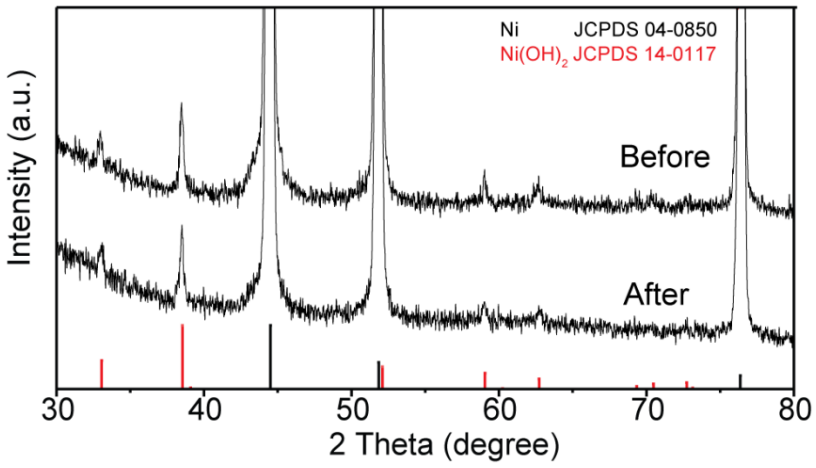

Figure 4.2 Powder X-ray diffraction (XRD) pattern collected for Fe doped β-$Ni(OH)_2$ before and after CV conditioning. The standard XRD spectra of Ni and $Ni(OH)_2$ are added for comparison.

Table 4.1 Fe concentration of Fe incorporated β-$Ni(OH)_2$ samples prepared with different amounts of iron (III) nitrate nonahydrate.

Sample	Amount of iron (III) nitrate nonahydrate (mg)	Fe Concentration (atomic %)
Ni-Fe-1	1.8	0.29
Ni-Fe-2	3.6	0.54
Ni-Fe-3	7.2	1.07

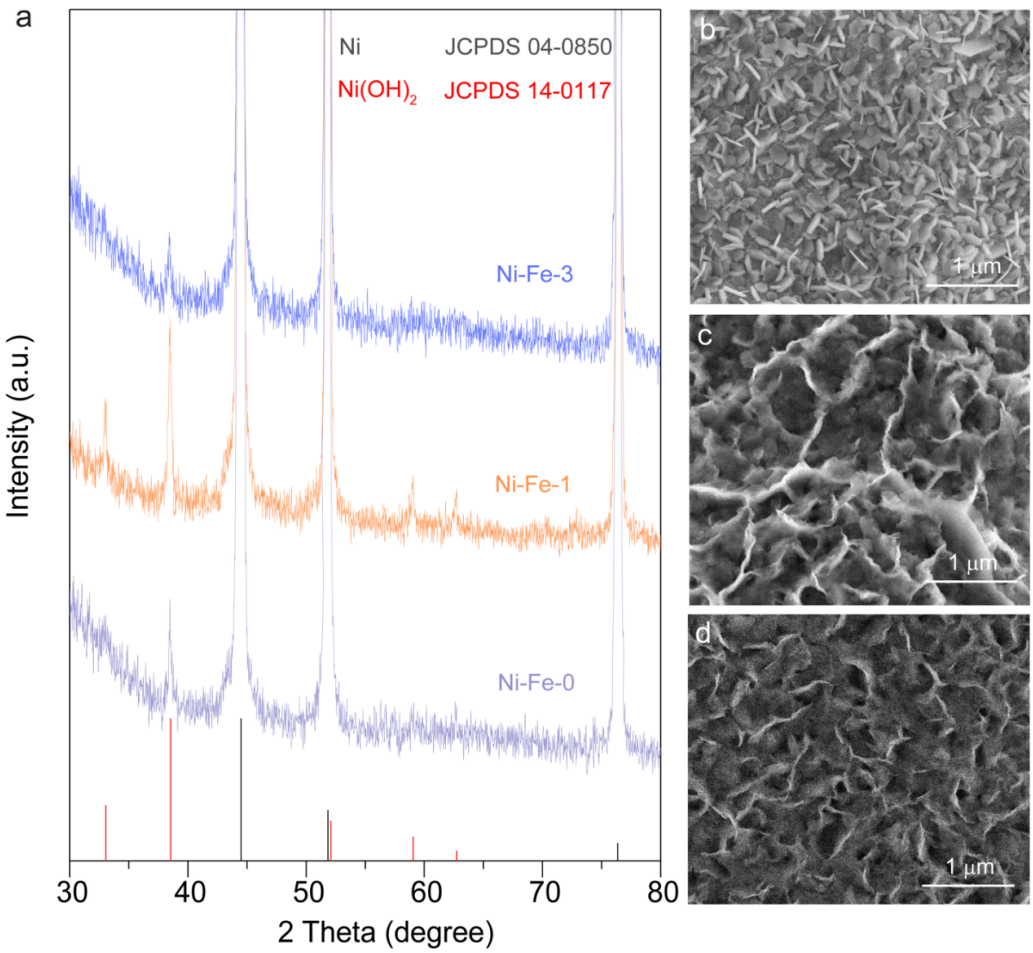

Figure 4.3 (a) X-ray diffraction patterns, and (b-d) the SEM image of (b) Ni-Fe-0, (c) Ni-Fe-1 and (d) Ni-Fe-3, respectively.

To probe the local structure and valence state of the Fe-doped β-$Ni(OH)_2$ samples, Ni and Fe K-edge X-ray absorption spectroscopy (XAS) data (Figure 4.4) were recorded at beamline 10.3.2 of the Advanced Light Source, Berkeley, Lawrence Berkeley National Laboratory, CA.[24] The white line of the Ni K-edge spectrum of Ni-Fe-2 is centered at 8350 eV (Figure 4.4), corresponding to Ni^{2+} as previously reported in the literature.[25] Ni K-edge EXAFS data evidenced an extra peak at 1.2 Å, corresponding to a Ni-O bond, when compared with the Ni foil spectrum showing only

Ni-Ni coordination. Overall Ni XAS data showed clear evidence of the successful growth of $Ni(OH)_2$ on the Ni substrate. Further, Fe K-edge XANES data on the Fe dopant in the Ni-Fe-2 sample show a white line peak at 7130.4 eV associated with the 1s to 4p dipole transition, suggesting the presence of oxidized Fe (Figure 4.4b).[26,27] The Fe XANES data could not be fitted nor the oxidation state determined due to poor signal quality. Overall, XAS results confirmed the substitutional doping of oxidized Fe in β-$Ni(OH)_2$ structures and Fe remains in oxidized form.

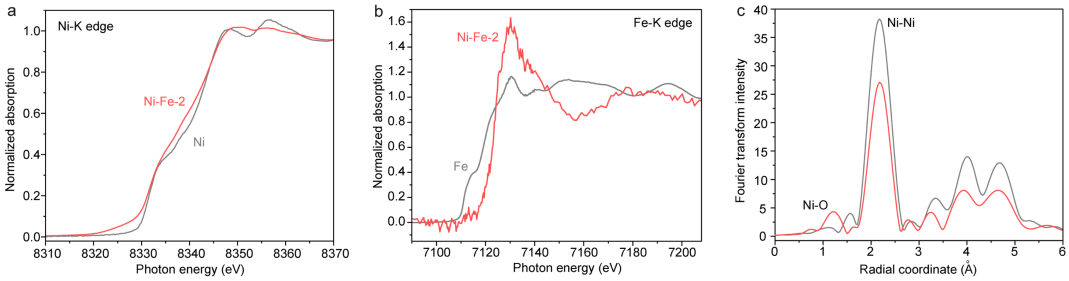

Figure 4.4 (a) Ni K-edge XANES spectra of Ni-Fe-2 and Ni foil. (b) Fe K-edge XANES spectra of Ni-Fe-2 and Fe foil. (c) Magnitude of the Fourier-transformed Ni K-edge EXAFS spectra.

The catalytic performances of the Fe doped β-$Ni(OH)_2$ nanosheets for OER were investigated through linear sweep voltammetry (Figure 4.5a) conducted in O_2 saturated 1.0 M KOH electrolyte. The anodic oxidation peaks in the polarization curves correspond to the conversion of β-$Ni(OH)_2$ to β-NiOOH, which is believed to be the active catalyst for OER.[28] Dramatically increased current after the oxidation peak indicates the rigorous OER process. Overpotentials at the geometric current density of 10 mA/cm^2 were measured for the evaluation of total electrode activity.[29] As shown in Figure 4.5a, the bare Ni foam has the largest overpotential of 305 mV at j_{geo}=10 mA/cm^2. The growth of $Ni(OH)_2$ nanosheets on Ni foam (Ni-Fe-0) significantly

reduces the overpotential and boosts the total electrode activity, as $Ni(OH)_2$ is believed to be more favorable for the adsorption of OER intermediate such as OH than Ni foam. All Fe doped β-$Ni(OH)_2$ samples show even lower overpotential than Ni-Fe-0. Among them, Ni-Fe-2 exhibits the lowest overpotential of 219 mV at j_{geo}=10 mA/cm^2, which is the best value reported for Ni or Fe hydroxide based OER catalysts (Table 4.2), obtained at the same geometric current density in the same electrolyte (1.0 M KOH). An average overpotential of 219.6 mV at 10 mA/cm^2 was obtained from four different Ni-Fe-2 samples (Figure 4.6), confirming the results are highly reproducible. All the three Fe doped β-$Ni(OH)_2$ samples have similar Tafel slopes between 53 mV/dec and 57 mV/dec, which are slightly smaller than the values obtained from β-$Ni(OH)_2$ (61 mV/dec) and bare Ni foam (64 mV/dec), as shown in Figure 4.5b. Tafel slope has been used to analyze the kinetics of OER rate-determining step.[30, 31] The Tafel slopes of 53-57 mV/dec suggests that ·OH adsorption is favorable on the surface of Fe-doped β-$Ni(OH)_2$ nanosheets, while the subsequent step with deprotonation of ∗OH (∗ is the active site) is the rate-determining step.

The total electrode activity is determined by the total number of active sites and the intrinsic activity of each individual active site. The number of active sites is typically proportional to the electrochemical surface area (ECSA). Figure 4.5c shows the plots of the difference of anodic and cathodic current density versus the scan rate, in which the slope of the curves (areal capacitance) is proportional to their ECSA. Ni-Fe-2 has the highest areal capacitance of 2.96 mF/cm^2, which are substantially higher than the other samples. The results suggest that Ni-Fe-2 has the highest number of active sites, which is expected to be determined by its compositional and structural

features such as Fe doped amorphous/crystalline interface. Furthermore, the higher number of active sites is favorable for charge transfer. Electrochemical impedance spectroscopy (EIS) studies were conducted for Fe-doped β-$Ni(OH)_2$ samples and the control samples (Figure 4.5d). The EIS results are fitted based on the equivalent circuit (Figure 4.5d inset) and the obtained solution resistance (R_s) and charge transfer resistance (R_{ct}) are summarized in Table 4.3 (Supporting Information). As expected, Ni-Fe-2 has the smallest R_{ct} of 2.971 Ω/cm^2, which is considerably smaller than the values obtained from Ni-Fe-0 (7.120 Ω/cm^2), Ni-Fe-1 (7.077 Ω/cm^2) and Ni-Fe-3 (8.120 Ω/cm^2), respectively. The Ni foam has the highest R_{ct} of 30.45 Ω/cm^2 due to the lack of OER active sites. It is also noteworthy that all Fe-doped β-$Ni(OH)_2$ samples have fairly small values of R_s that is comparable to the value of bare Ni foam, ensuring efficient charge transport.

To determine the intrinsic activity of individual active site, we normalize the OER current to ECSA (j_{ECSA}). As shown in Figure 4.5e, Ni-Fe-2 achieves j_{ECSA} of 10 mA cm^{-2} at fairly low overpotential of 316 mV. At the same overpotential, Ni-Fe-0, Ni-Fe-1 and Ni-Fe-3 exhibit significantly lower j_{ECSA} of 3.7, 7.0 and 4.5 mA cm^{-2}, respectively and the bare Ni foam has the worst j_{ECSA} of only 1.2 mA cm^{-2}. It is clear that the intrinsic activity of β-$Ni(OH)_2$ is significantly better than the Ni foam substrate, and the introduction of right amount of Fe doping can further boost its intrinsic activity towards OER. Most importantly, the results also confirmed that the excellent catalytic activity of Ni-Fe-2 is not only due to the increased ECSA but also the enhanced intrinsic activity of each active site in converting OH^- into oxygen gas. The intrinsic activity of Ni-Fe-2 is substantially better than many other state-of-the-art OER catalysts (Figure 4.5f). In

addition, the Ni-Fe-2 was able to retain almost the same OER catalytic performance after testing for 10000 cycles (Figure 4.7), showing its excellent stability.

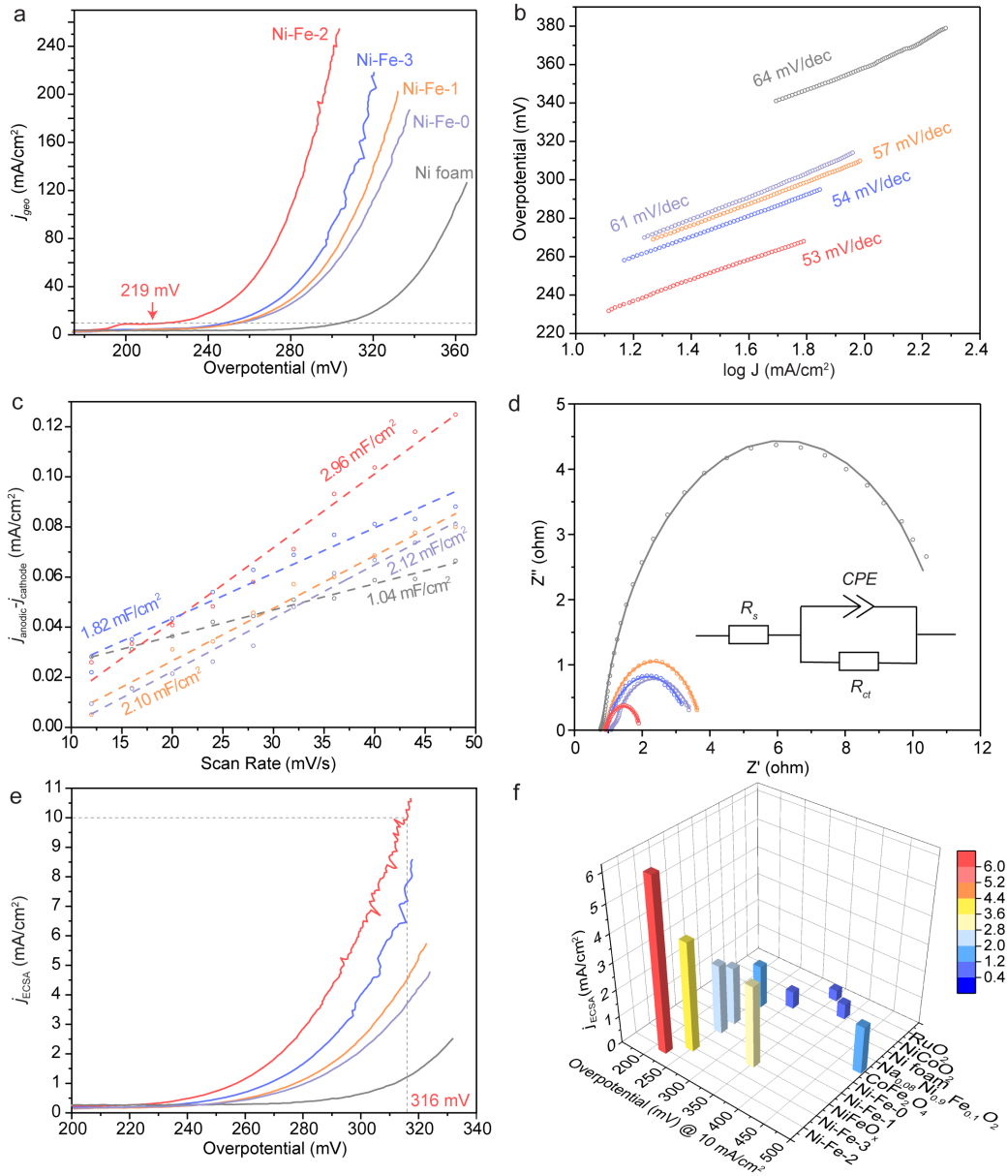

Figure 4.5 (a) OER polarization curves obtained from Ni-Fe-0, Ni-Fe-1, Ni-Fe-2, Ni-Fe-3 and Ni foam in 1.0 M KOH solution at a scan rate of 1 mV/s. Dashed line corresponding to 10 mA/cm^2. (b) Tafel plots of the samples. The values are the slope of each curves. (c) Plots of difference of anodic and cathodic current density as a function of scan rate; (d) Electrochemical impedance spectra of the samples collected at the overpotential of 291 mV, with frequency from 100 kHz to 1 Hz and amplitude

of 5 mV. Dots and lines represent the experimental and simulated data, respectively. (e) Polarization curves of the samples with current density normalized to ECSA. (f) 3D histogram compares the ECSA current densities and overpotentials at 10 mA/cm^2 of Fe-doped β-Ni(OH)$_2$ samples with other state-of-the-art OER catalysts including $NiCoO_2$,[7] $NiFeO_x$,[32] $CoFe_2O_4$,[33] $Na_{0.08}Ni_{0.9}Fe_{0.1}O_2$,[34] RuO_2,[34].

Table 4.2 Comparisons of OER performance of Ni-/Fe (oxy)hydroxide based catalysts

Catalyst	Overpotential (mV) at j_{geo}=10 mA/cm^2	Scan rate (mV/s)	References
Fe-doped β-Ni(OH)$_2$ nanosheets/Ni foam	219	1	This work
Fe-doped β-Ni(OH)$_2$ nanoparticles	260	10	15
Fe-doped β-NiOOH films	340	10	35
NiFe-LDH nanoplates array	224	10	36
NiFe-LDH nanoplates films	250	1	37
NiFe-LDH nanosheets	300	5	38
Ni nanoparticles/NiFe LDH	320	5	39
NiFe-LDH/CNT	230	5	40
$Ni_{2/3}Fe_{1/3}$-LDH/rGO	240	5	41
NiFe-LDH/graphene and CNT	350	10	42
Ni(Fe)OOH films	260	_	43

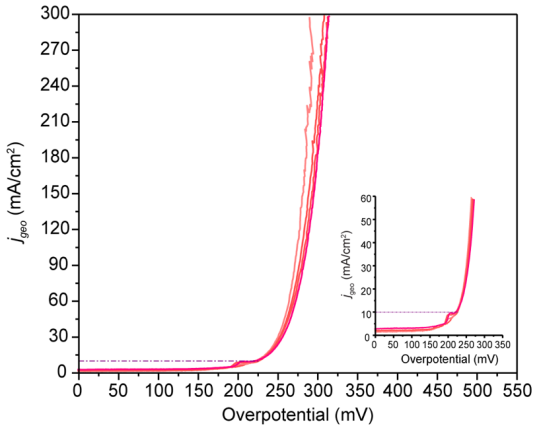

Figure 4.6 Polarization curves collected for four different Ni-Fe-2 samples at the scan rate of 1 mV/s in O_2 saturated 1.0 M KOH (*iR* corrected).

Table 4.3 The simulated equivalent circuit data of the Ni-Fe and Ni samples.

Sample	R_s [Ω cm^{-2}]	R_{ct} [Ω cm^{-2}]	CPE-T	CPE-P
Ni-Fe-0	3.223	7.120	1.903×10^{-2}	0.7160
Ni-Fe-1	2.627	8.120	9.983×10^{-3}	0.8103
Ni-Fe-2	2.649	2.971	3.293×10^{-2}	0.7877
Ni-Fe-3	2.686	7.077	1.952×10^{-2}	0.7454
Ni foam	2.306	30.45	4.270×10^{-3}	0.8847

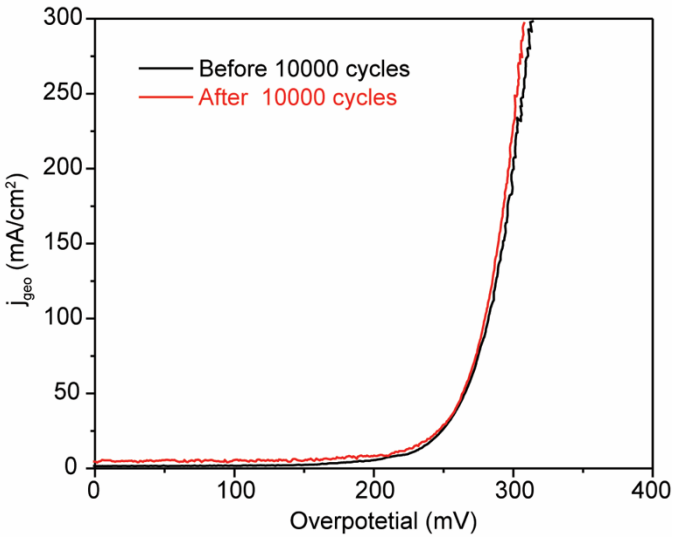

Figure 4.7 Polarization curves of Ni-Fe-2 samples obtained before and after testing for 10000 cycles at the scan rate of 1 mV/s in O_2 saturated 1.0 M KOH (*iR* corrected).

4.4 Conclusions

To summarize, the outstanding catalytic activity of Ni-Fe-2 can be attributed to several factors. First, the vertically aligned crumpled nanosheets offer large number of highly accessible active sites. Second, the good porosity of the nanosheet network allows rapid release of oxygen gas bubbles during OER, which otherwise would pose a physical barrier between the active sites and electrolytes.[44] Third, we believe that the co-existence of amorphous and crystal microstructures on the Fe-doped β-$Ni(OH)_2$ nanosheets may also contribute to the improved catalytic activity. Although amorphous structures usually have lower electrical conductivity than crystalline materials because of its long-range disorder, the surface heterogeneity would expose additional active sites for OER.[45,46] The boundaries between crystalline and amorphous structures represent the under-coordination positions and generally serve as the preferential adsorption sites towards the reactants in OER.[47] Also, recent theoretical simulations also found that the Fe dopants serve as active sites owing to its appropriate adsorption strength towards the OER intermediates, and its strong electron-withdrawing effect turns the surrounding of Ni to the 'hot-spot' for OER.[48,49] In addition, Ni foam is also believed to enhance the OER performances of Fe doped β-$Ni(OH)_2$ nanosheets in two ways. First, its highly porous structure can facilitate the diffusion of the electrolyte and oxygen gas evolution during OER. Second, Ni foam offers not only a substrate for the seamless growth of Fe doped β-$Ni(OH)_2$ nanosheets but also serves as a highly conductive current collector that allows efficient electron transfer from Fe doped β-

$Ni(OH)_2$ nanosheets to Ni foam during OER. This work demonstrates an inexpensive catalyst with ultralow overpotential and outstanding intrinsic catalyst activity. The findings also provide important guidelines for design and synthesis of Ni based OER catalysts.

References

1. Kou, T.; Smart, T.; Yao, B.; Chen, I.; Thota, D.; Ping, Y.; Li, Y. *Adv. Energy Mater.* **2018**, *8*, 1703538.

2. Wu, Y.; Liu, Y.; Li, G.-D.; Zou, X.; Lian, X.; Wang, D.; Sun, L.; Asefa, T.; Zou, X. *Nano Energy* **2017,** *35*, 161-170.

3. Yu, M.; Zhao, S.; Feng, H.; Hu, L.; Zhang, X.; Zeng, Y.; Tong, Y.; Lu, X. *ACS Energy Lett*. **2017**, *2*, 1862-1868.

4. Zhang, J.; Wang, Y.; Zhang, C.; Gao, H.; Lv, L.; Han, L.; Zhang, Z. *ACS Sustain*. *Chem*. *Eng*. **2018**, *6*, 2231-2239.

5. Tahir, M.; Pan, L.; Idrees, F.; Zhang, X.; Wang, L.; Zou, J.-J.; Wang, Z. L. *Nano Energy* **2017,** *37*, 136-157.

6. Zou, X.; Liu, Y.; Li, G.-D.; Wu, Y.; Liu, D.-P.; Li, W.; Li, H.-W.; Wang, D.; Zhang, Y.; Zou, X. *Adv. Mater.* **2017**, *29*, 1700404.

7. Jung, S.; McCrory, C. C. L.; Ferrer, I. M.; Peters, J. C.; Jaramillo, T. F. *J. Mater*. *Chem*. *A* **2016**, *4*, 3068-3076.

8. Reier, T.; Pawolek, Z.; Cherevko, S.; Bruns, M.; Jones, T.; Teschner, D.; Selve, S.; Bergmann, A.; Nong, H. N.; Schlögl, R.; Mayrhofer, K. J. J.; Strasser, P. *J. Am*. *Chem*. *Soc*. **2015**, *137*, 13031-13040.

9. Wang, A.-L.; Xu, H.; Li, G.-R. *ACS Energy Lett*. **2016**, *1*, 445-453.

10. Feng, L.-L.; Yu, G.; Wu, Y.; Li, G.-D.; Li, H.; Sun, Y.; Asefa, T.; Chen, W.; Zou, X. *J*. *Am*. *Chem*. *Soc*. **2015**, *137*, 14023-14026

11. Long, X.; Lin, H.; Zhou, D.; An, Y.; Yang, S. *ACS Energy Lett*. **2018**, *3*, 290-296.

12. Gerken, J. B.; Shaner, S. E.; Massé, R. C.; Porubsky, N. J.; Stahl, S. S. *Energy Environ. Sci.* **2014**, *7*, 2376-2382.

13. Morales-Guio, C. G.; Liardet, L.; Hu, X. *J*. *Am*. *Chem*. *Soc*. **2016**, *138*, 8946-8957.

14. Zhou, D.; Xiong, X.; Cai, Z.; Han, N.; Jia, Y.; Xie, Q.; Duan, X.; Xie, T.; Zheng, X.; Sun, X.; Duan, X. *Small Methods* **2018**, *2*, 1800083.

15. Zhu, K.; Liu, H.; Li, M.; Li, X.; Wang, J.; Zhu, X.; Yang, W. *J*. *Mater*. *Chem*. *A* **2017**, *5*, 7753-7758.

16. Voiry, D.; Chhowalla, M.; Gogotsi, Y.; Kotov, N. A.; Li, Y.; Penner, R. M.; Schaak, R. E.; Weiss, P. S. *ACS Nano* **2018**, *12*, 9635-9638.

17. McCrory, C. C. L.; Jung, S.; Ferrer, I. M.; Chatman, S. M.; Peters, J. C.; Jaramillo, T. F. *J*. *Am*. *Chem*. *Soc*. **2015**, *137*, 4347-4357.

18. Li, Z.; Yu, L.; Milligan, C.; Ma, T.; Zhou, L.; Cui, Y.; Qi, Z.; Libretto, N.; Xu, B.; Luo, J.; Shi, E.; Wu, Z.; Xin, H.; Delgass, W. N.; Miller, J. T.; Wu, Y. *Nat*. *Commun*. **2018**, *9*, 5258.

19. Zaffran, J.; Nagli, M.; Shehadeh, M.; Toroker, M. C. *Theor*. *Chem*. *Acc*. **2018,** *137*, 3.

20. Stevens, M. B.; Enman, L. J.; Batchellor, A. S.; Cosby, M. R.; Vise, A. E.; Trang, C. D. M.; Boettcher, S. W. *Chem*. *Mater*. **2017,** *29*, 120-140.

21. Zou, X.; Sun, Q.; Zhang, Y.; Li, G.-D.; Liu, Y.; Wu, Y.; Yang, L.; Zou, X. *Sci*. *Rep*. **2018**, *8*, 4478.

22. Petersen, M. A.; van den Berg, J.-A.; Ciobîcă, I. M.; van Helden, P. *ACS Catal*. **2017**, *7*, 1984-1992.

23. Fan, X.; Liu, Y.; Chen, S.; Shi, J.; Wang, J.; Fan, A.; Zan, W.; Li, S.; Goddard, W. A.; Zhang, X.-M. *Nat*. *Commun*. **2018**, *9*, 1809.

24. Marcus, M.; MacDowell, A.; Celestre, R.; Manceau, A.; Miller, T.; Padmore, H.; Sublett, R. *J. Synchrotron Radiat.* **2004**, *11*, 239-247.

25. Mansour, A. N.; Melendres, C. A. *Physica B Condens*. *Matter*. **1995**, *208-209*, 583-584.

26. Chen, C. L.; Dong, C. L.; Rao, S. M.; Chern, G.; Chen, M. C.; Wu, M. K.; Chang, C. L. *J. Phys*. *Condens*. *Matter*. **2008**, *20*, 255236.

27. Lin, K.-S.; Wang, Z.-P.; Chowdhury, S.; Adhikari, A. K. *Thin Solid Films* **2009**, *517*, 5192-5196.

28. Li, Y.-F.; Selloni, A. *ACS Catal*. **2014**, *4*, 1148-1153.

29. Luo, J.; Im, J.-H.; Mayer, M. T.; Schreier, M.; Nazeeruddin, M. K.; Park, N.-G.; Tilley, S. D.; Fan, H. J.; Grätzel, M. *Science* **2014**, *345*, 1593-1596.

30. García-Osorio, D. A.; Jaimes, R.; Vazquez-Arenas, J.; Lara, R. H.; Alvarez-Ramirez, J. *J. Electrochem*. *Soc*. **2017**, *164*, E3321-E3328.

31. Shinagawa, T.; Garcia-Esparza, A. T.; Takanabe, K. *Sci*. *Rep*. **2015**, *5*, 13801.

32. McCrory, C. C. L.; Jung, S.; Peters, J. C.; Jaramillo, T. F. *J. Am. Chem. Soc.* **2013,** *135*, 16977-16987.

33. Sagu, J. S.; Mehta, D.; Wijayantha, K. G. U. *Electrochem. Commun.* **2018,** *87*, 1-4.

34. Weng, B.; Xu, F.; Wang, C.; Meng, W.; Grice, C. R.; Yan, Y. *Energy Environ. Sci.* **2017**, *10*, 121-128.

35. Swierk, J. R.; Klaus, S.; Trotochaud, L.; Bell, A. T.; Tilley, T. D. *J. Phys. Chem. C* **2015**, *119*, 19022-19029.

36. Li, Z.; Shao, M.; An, H.; Wang, Z.; Xu, S.; Wei, M.; Evans, D. G.; Duan, X. *Chem. Sci.* **2015**, *6*, 6624-6631.

37. Lu, Z.; Xu, W.; Zhu, W.; Yang, Q.; Lei, X.; Liu, J.; Li, Y.; Sun, X.; Duan, X. *Chem. Commun.* **2014**, *50*, 6479-6482.

38. Song, F.; Hu, X. *Nat. Commun.* **2014**, *5*, 4477.

39. Gao, X.; Long, X.; Yu, H.; Pan, X.; Yi, Z. *J. Electrochem. Soc.* **2017**, *164*, H307-H310.

40. Gong, M.; Li, Y.; Wang, H.; Liang, Y.; Wu, J. Z.; Zhou, J.; Wang, J.; Regier, T.; Wei, F.; Dai, H. *J. Am. Chem. Soc.* **2013**, *135*, 8452-8455.

41. Ma, W.; Ma, R.; Wang, C.; Liang, J.; Liu, X.; Zhou, K.; Sasaki, T. *ACS Nano* **2015**, *9*, 1977-1984.

42. Zhu, X.; Tang, C.; Wang, H.-F.; Zhang, Q.; Yang, C.; Wei, F. *J. Mater. Chem. A* **2015**, *3*, 24540-24546.

43. Batchellor, A. S.; Boettcher, S. W. *ACS Catal.* **2015**, *5*, 6680-6689.

44. Chen, Y.; Yu, G.; Chen, W.; Liu, Y.; Li, G.-D.; Zhu, P.; Tao, Q.; Li, Q.; Liu, J.; Shen, X.; Li, H.; Huang, X.; Wang, D.; Asefa, T.; Zou, X. *J*. *Am*. *Chem*. *Soc*. **2017,** *139*, 12370-12373.

45. Gao, Y.; Li, H.; Yang, G. *Cryst*. *Growth Des*. **2015**, *15*, 4475-4483.

46. Smith, R. D. L.; Prévot, M. S.; Fagan, R. D.; Zhang, Z.; Sedach, P. A.; Siu, M. K. J.; Trudel, S.; Berlinguette, C. P. *Science* **2013**, *340*, 60-63.

47. Lyons, M. E. G.; Floquet, S. *Phys*. *Chem*. *Chem*. *Phys*. **2011,** *13*, 5314-5335.

48. Qi, J.; Zhang, W.; Xiang, R.; Liu, K.; Wang, H.-Y.; Chen, M.; Han, Y.; Cao, R. *Adv*. *Sci*. **2015,** *2*, 1500199.

49. Zaffran, J.; Toroker, M. C. *ChemistrySelect* **2016,** *1*, 911-916.

Chapter 5

Outlook

An efficient water splitting requires active and robust catalyst and the design of the capable catalyst is thus critically important. Nonetheless, owing to the lack of effective catalyst design principles, boosting reaction kinetics has been a long-standing challenge for our community. Most of the time, 'trial and error' is still the major method that our community employs to develop new catalysts, whereas the strategy is short of clear motivations and time-intensive. Structural and compositional design should all be considered in the development of water splitting catalysts. For example, hierarchical porous structure is expected to enhance the electrochemical surface area as well as creating mass transport channel for water splitting.[1] A reasonable composition design is equivalently significant as the active centers are deeply associated with the catalyst compositions.[2] As the water splitting reactions (either HER or OER) include multi-step elementary reactions, enriching the catalysts with synergistic active centers that targets the improvement of the rate limiting step reaction kinetics should be a rational strategy. For instance, a Ni/NiO composite that contains the hydrogen adsorption and water dissociation dual centers is helpful in enhancing the water-alkali HER kinetics, compared to the sole active site.[3]

Theoretical study such as DFT calculations is powerful in revealing the mechanism of the as-synthesized catalyst, and this technique is also employed to predict new active centers. In spite of the advantages of DFT simulations, combining DFT predictions with experimental techniques to realize the predicted active centers is still, in most of the cases, difficult. The challenges are mainly due to the tremendous gap between the

theoretical predictions and the factual active center experimentally synthesized. DFT simulations are mainly focused on atomic level whereas it is challenging for the conventional materials synthesis strategy to precisely control over the active center. It is thus significant to develop advanced materials synthesis techniques to optimize the active centers for enhanced catalytic activity.

The last aspect that has significant impact on the catalyst design is characterizing the true active centers during the water splitting. Even though tremendous efforts have been made to design different catalysts, many of the active centers suffer instability during water splitting and have the chances to evolve into different kinds of active centers or just fail to function. It is also important to study the compositionally stability of the active centers either from spent catalysts or involving operando spectroscopy including Raman, X-ray absorption, etc.[4, 5] The study of evolution of active centers during HER or OER is critical to evaluate the robustness of the catalysts and can also in turn provide the new insights in design both active and stable catalysts.

References

1. Ang, H.; Wang, H.; Li, B.; Zong, Y.; Wang, X.; Yan, Q. *Small* **2016,** *12*, 2859-2865.

2. Zou, X.; Zhang, Y. *Chem*. *Soc*. *Rev*. **2015,** *44*, 5148-5180.

3. Gong, M.; Zhou, W.; Tsai, M.-C.; Zhou, J.; Guan, M.; Lin, M.-C.; Zhang, B.; Hu, Y.; Wang, D.-Y.; Yang, J.; Pennycook, S. J.; Hwang, B.-J.; Dai, H. *Nat*. *Commun*. **2014,** *5*, 4695.

4. Yeo, B. S.; Bell, A. T. *J*. *Phys*. *Chem*. *C* **2012,** *116*, 8394-8400.

5. Cao, L.; Luo, Q.; Liu, W.; Lin, Y.; Liu, X.; Cao, Y.; Zhang, W.; Wu, Y.; Yang, J.; Yao, T.; Wei, S. *Nat*. *Catal*. **2019,** *2*, 134-141.

Bibliography

Acar, C.; Dincer, I. *Int. J. Hydrog. Energy* **2014,** *39*, 1-12.

Ang, H.; Wang, H.; Li, B.; Zong, Y.; Wang, X.; Yan, Q. *Small* **2016,** *12*, 2859-2865.

Aray, Y.; Vega, D.; Rodriguez, J.; Vidal, A. B.; Grillo, M. E.; Coll, S. *J. Phys. Chem. B* **2009,** *113*, 3058-3070.

Baroni, S.; de Gironcoli, S.; Dal Corso, A.; Giannozzi, P. *Rev. Mod. Phys.* **2001,** *73*, 515-562.

Bard, A. J., *Electrochemical methods : fundamentals and applications / Allen J. Bard, Larry R. Faulkner*. Wiley: New York, 1980.

Batchellor, A. S.; Boettcher, S. W. *ACS Catal.* **2015**, *5*, 6680-6689.

Brandes, J. A.; Wirick, S.; Jacobsen, C. *J. Synchrotron Rad.* **2010,** *17*, 676-682.

Cao, L.; Luo, Q.; Liu, W.; Lin, Y.; Liu, X.; Cao, Y.; Zhang, W.; Wu, Y.; Yang, J.; Yao, T.; Wei, S. *Nat. Catal.* **2019,** *2*, 134-141.

Chen, X.; Burda, C. *J. Am. Chem. Soc.* **2008,** *130*, 5018-5019.

Chen, P.; Xu, K.; Tao, S.; Zhou, T.; Tong, Y.; Ding, H.; Zhang, L.; Chu, W.; Wu, C.; Xie, Y. *Adv. Mater.* **2016,** *28*, 7527-7532.

Chen, C. L.; Dong, C. L.; Rao, S. M.; Chern, G.; Chen, M. C.; Wu, M. K.; Chang, C. L. *J. Phys. Condens. Matter.* **2008**, *20*, 255236.

Chen, Y.; Yu, G.; Chen, W.; Liu, Y.; Li, G.-D.; Zhu, P.; Tao, Q.; Li, Q.; Liu, J.; Shen, X.; Li, H.; Huang, X.; Wang, D.; Asefa, T.; Zou, X. *J. Am. Chem. Soc.* **2017,** *139*, 12370-12373.

Cheng, C. P.; Brown, T. L. *J. Am. Chem. Soc.* **1980,** *102*, 6418-6421.

Chia, X.; Eng, A. Y. S.; Ambrosi, A.; Tan, S. M.; Pumera, M. *Chem*. *Rev*. **2015,** *115*, 11941-11966.

Chung, D. Y.; Han, J. W.; Lim, D.-H.; Jo, J.-H.; Yoo, S. J.; Lee, H.; Sung, Y.-E. *Nanoscale* **2015,** *7*, 5157-5163.

Cui, Z.; Ge, Y.; Chu, H.; Baines, R.; Dong, P.; Tang, J.; Yang, Y.; Ajayan, P. M.; Ye, M.; Shen, J. *J*. *Mater*. *Chem*. *A* **2017,** *5*, 1595-1602.

Dau, H.; Limberg, C.; Reier, T.; Risch, M.; Roggan, S.; Strasser, P. *ChemCatChem* **2010,** *2*, 724-761.

Fan, X.; Liu, Y.; Chen, S.; Shi, J.; Wang, J.; Fan, A.; Zan, W.; Li, S.; Goddard, W. A.; Zhang, X.-M. *Nat*. *Commun*. **2018**, *9*, 1809.

Feng, L.-L.; Yu, G.; Wu, Y.; Li, G.-D.; Li, H.; Sun, Y.; Asefa, T.; Chen, W.; Zou, X. *J*. *Am*. *Chem*. *Soc*. **2015,** *137*, 14023-14026

Gao, Y.; Li, H.; Yang, G. *Cryst*. *Growth Des*. **2015**, *15*, 4475-4483.

Gao, X.; Long, X.; Yu, H.; Pan, X.; Yi, Z. *J*. *Electrochem*. *Soc*. **2017**, *164*, H307-H310.

Garrity, K. F.; Bennett, J. W.; Rabe, K. M.; Vanderbilt, D. *Comput*. *Mater*. *Sci*. **2014,** *81*, 446-452.

García-Osorio, D. A.; Jaimes, R.; Vazquez-Arenas, J.; Lara, R. H.; Alvarez-Ramirez, J. *J*. *Electrochem*. *Soc*. **2017**, *164*, E3321-E3328.

Gerken, J. B.; Shaner, S. E.; Massé, R. C.; Porubsky, N. J.; Stahl, S. S. *Energy Environ. Sci.* **2014**, *7*, 2376-2382.

Gong, M.; Wang, D.-Y.; Chen, C.-C.; Hwang, B.-J.; Dai, H. *Nano Res*. **2016,** *9*, 28-46.

Gong, M.; Zhou, W.; Kenney, M. J.; Kapusta, R.; Cowley, S.; Wu, Y.; Lu, B.; Lin, M.-C.; Wang, D.-Y.; Yang, J.; Hwang, B.-J.; Dai, H. *Angew. Chem. Int. Ed.* **2015,** *54*, 11989-11993.

Gong, M.; Zhou, W.; Tsai, M.-C.; Zhou, J.; Guan, M.; Lin, M.-C.; Zhang, B.; Hu, Y.; Wang, D.-Y.; Yang, J.; Pennycook, S. J.; Hwang, B.-J.; Dai, H. *Nat. Commun.* **2014,** *5*, 4695.

Gong, M.; Li, Y.; Wang, H.; Liang, Y.; Wu, J. Z.; Zhou, J.; Wang, J.; Regier, T.; Wei, F.; Dai, H. *J. Am. Chem. Soc.* **2013**, *135*, 8452-8455.

Gunceler, D.; Letchworth-Weaver, K.; Sundararaman, R.; Schwarz, K. A.; Arias, T. A. *Model. Simul. Mater. Sci. Eng.* **2013,** *21*, 074005.

Grosvenor, A. P.; Biesinger, M. C.; Smart, R. S. C.; McIntyre, N. S. *Surf. Sci.* **2006,** *600*, 1771-1779.

Hassan, M. H.; Kalam, M. A. *Procedia Eng.* **2013,** *56*, 39-53.

Henkelman, G.; Jónsson, H. *J. Chem. Phys.* **1999,** *111*, 7010-7022.

Henkelman, G.; Uberuaga, B. P.; Jónsson, H., *J. Chem. Phys.* **2000,** *113*, 9901-9904.

Henkelman, G.; Arnaldsson, A.; Jónsson, H. *Comput. Mater. Sci.* **2006,** *36*, 354-360.

Hu, C.; Ma, Q.; Hung, S.-F.; Chen, Z.-N.; Ou, D.; Ren, B.; Chen, H. M.; Fu, G.; Zheng, N. *Chem 3*, 122-133.

Jaramillo, T. F.; Jørgensen, K. P.; Bonde, J.; Nielsen, J. H.; Horch, S. *Science* **2007,** *317*, 100-102.

Jiang, N.; Bogoev, L.; Popova, M.; Gul, S.; Yano, J.; Sun, Y. *J. Mater. Chem. A* **2014,** *2*, 19407-19414.

Jiang, N.; Tang, Q.; Sheng, M.; You, B.; Jiang, D.-e.; Sun, Y. *Catal*. *Sci*. *Technol*. **2016,** *6*, 1077-1084.

Jiang, K.; Liu, B.; Luo, M.; Ning, S.; Peng, M.; Zhao, Y.; Lu, Y.-R.; Chan, T.-S.; de Groot, F. M. F.; Tan, Y. *Nat*. *Commun*. **2019,** *10*, 1743.

Jiang, J.; Gao, M.; Sheng, W.; Yan, Y. *Angew*. *Chem*. *Int*. *Ed*. **2016,** *55*, 15240-15245.

Jin, H.; Wang, J.; Su, D.; Wei, Z.; Pang, Z.; Wang, Y. *J*. *Am*. *Chem*. *Soc*. **2015,** *137*, 2688-2694.

Jung, S.; McCrory, C. C. L.; Ferrer, I. M.; Peters, J. C.; Jaramillo, T. F. *J*. *Mater*. *Chem*. *A* **2016**, *4*, 3068-3076.

Kou, T.; Smart, T.; Yao, B.; Chen, I.; Thota, D.; Ping, Y.; Li, Y. *Adv*. *Energy Mater*. **2018,** *8*, 1703538.

Kou, T.; Wang, S.; Hauser, J. L.; Chen, M.; Oliver, S. R. J.; Ye, Y.; Guo, J.; Li, Y. *ACS Energy Lett*. **2019**, *4*, 622-628.

Kong, D.; Wang, H.; Cha, J. J.; Pasta, M.; Koski, K. J.; Yao, J.; Cui, Y. *Nano Lett*. **2013,** *13*, 1341-1347.

Kuznetsova, A.; Popova, I.; Yates, J. T.; Bronikowski, M. J.; Huffman, C. B.; Liu, J.; Smalley, R. E.; Hwu, H. H.; Chen, J. G. *J*. *Am*. *Chem*. *Soc*. **2001,** *123*, 10699-10704.

LeRoy, R. L. *Int*. *J*. *Hydrog*en *Energy* **1983,** *8*, 401-417.

Li, L.; Kanai, Y. *Phys*. *Rev*. *B* **2015,** *91*, 235304.

Li, Z.; Shao, M.; An, H.; Wang, Z.; Xu, S.; Wei, M.; Evans, D. G.; Duan, X. *Chem*. *Sci*. **2015**, *6*, 6624-6631.

Li, Y.-F.; Selloni, A. *ACS Catal*. **2014**, *4*, 1148-1153.

Li, Y.; Zhang, J. Z. *Laser Photon*. *Rev*. **2010,** *4*, 517-528.

Li, Z.; Yu, L.; Milligan, C.; Ma, T.; Zhou, L.; Cui, Y.; Qi, Z.; Libretto, N.; Xu, B.; Luo, J.; Shi, E.; Wu, Z.; Xin, H.; Delgass, W. N.; Miller, J. T.; Wu, Y. *Nat*. *Commun*. **2018**, *9*, 5258.

Li, X.; Hao, X.; Abudula, A.; Guan, G. *J. Mater*. *Chem*. *A* **2016,** *4*, 11973-12000.

Li, H.; Tsai, C.; Koh, A. L.; Cai, L.; Contryman, A. W.; Fragapane, A. H.; Zhao, J.; Han, H. S.; Manoharan, H. C.; Abild-Pedersen, F.; Nørskov, J. K.; Zheng, X. *Nat*. *Mater*. **2015,** *15*, 48.

Li, J.; Shen, P. K.; Tian, Z. *Int*. *J*. *Hydrogen Energy* **2017,** *42*, 7136-7142.

Liang, H.; Gandi, A. N.; Anjum, D. H.; Wang, X.; Schwingenschlögl, U.; Alshareef, H. N. *Nano Lett*. **2016,** *16*, 7718-7725.

Lin, H.; Liu, F.; Wang, X.; Ai, Y.; Yao, Z.; Chu, L.; Han, S.; Zhuang, X. *Electrochim*. *Acta* **2016,** *191*, 705-715.

Lin, T.-W.; Liu, C.-J.; Dai, C.-S. *Appl*. *Catal*. *B* **2014,** *154*, 213-220.

Lin, K.-S.; Wang, Z.-P.; Chowdhury, S.; Adhikari, A. K. *Thin Solid Films* **2009**, *517*, 5192-5196.

Liu, B.; Liu, L.-M.; Lang, X.-F.; Wang, H.-Y.; Lou, X. W.; Aydil, E. S. *Energy & Environ. Sci.* **2014,** *7*, 2592-2597.

Liu, Z.-H.; Broughton, J. *Phys*. *Rev*. *B* **1989,** *40*, 571-577.

Long, X.; Lin, H.; Zhou, D.; An, Y.; Yang, S. *ACS Energy Lett*. **2018**, *3*, 290-296.

Luo, Z.; Miao, R.; Huan, T. D.; Mosa, I. M.; Poyraz, A. S.; Zhong, W.; Cloud, J. E.; Kriz, D. A.; Thanneeru, S.; He, J.; Zhang, Y.; Ramprasad, R.; Suib, S. L. *Adv*. *Energy Mater*. **2016,** *6*, 1600528.

Luo, J.; Im, J.-H.; Mayer, M. T.; Schreier, M.; Nazeeruddin, M. K.; Park, N.-G.; Tilley, S. D.; Fan, H. J.; Grätzel, M. *Science* **2014**, *345*, 1593-1596.

Lu, Z.; Xu, W.; Zhu, W.; Yang, Q.; Lei, X.; Liu, J.; Li, Y.; Sun, X.; Duan, X. *Chem*. *Commun*. **2014**, *50*, 6479-6482.

Lyons, M. E. G.; Floquet, S. *Phys*. *Chem*. *Chem*. *Phys*. **2011,** *13*, 5314-5335.

Ma, W.; Ma, R.; Wang, C.; Liang, J.; Liu, X.; Zhou, K.; Sasaki, T. *ACS Nano* **2015**, *9*, 1977-1984.

Mahmood, N.; Yao, Y.; Zhang, J.-W.; Pan, L.; Zhang, X.; Zou, J.-J. *Adv*. *Sci*. **2018,** *5*, 1700464.

Man, I. C.; Su, H.-Y.; Calle-Vallejo, F.; Hansen, H. A.; Martínez, J. I.; Inoglu, N. G.; Kitchin, J.; Jaramillo, T. F.; Nørskov, J. K.; Rossmeisl, J. *ChemCatChem* **2011,** *3*, 1159-1165.

Mansour, A. N.; Melendres, C. A. *Physica B Condens*. *Matter*. **1995**, *208-209*, 583-584.

Mangolini, F.; McClimon, J. B.; Rose, F.; Carpick, R. W. *Anal*. *Chem*. **2014,** *86*, 12258-12265.

Marcus, M.; MacDowell, A.; Celestre, R.; Manceau, A.; Miller, T.; Padmore, H.; Sublett, R. *J. Synchrotron Radiat.* **2004**, *11*, 239-247.

Marton, D.; Boyd, K. J.; Al-Bayati, A. H.; Todorov, S. S.; Rabalais, J. W. *Phys*. *Rev*. *Lett*. **1994,** *73*, 118-121.

McCrory, C. C. L.; Jung, S.; Ferrer, I. M.; Chatman, S. M.; Peters, J. C.; Jaramillo, T. F. *J*. *Am*. *Chem*. *Soc*. **2015**, *137*, 4347-4357.

McCrory, C. C. L.; Jung, S.; Peters, J. C.; Jaramillo, T. F. *J. Am. Chem. Soc*. **2013,** *135*, 16977-16987.

Metcalf, P. A.; Fanwick, P.; Kąkol, Z.; Honig, J. M. *J. Solid State Chem*. **1993,** *104*, 81-87.

Mi, L.; Wei, W.; Huang, S.; Cui, S.; Zhang, W.; Hou, H.; Chen, W. *J. Mater. Chem. A* **2015,** *3*, 20973-20982.

Morales-Guio, C. G.; Thorwarth, K.; Niesen, B.; Liardet, L.; Patscheider, J.; Ballif, C.; Hu, X. *J. Am. Chem. Soc*. **2015,** *137*, 7035-7038.

Morales-Guio, C. G.; Liardet, L.; Hu, X. *J. Am. Chem. Soc*. **2016**, *138*, 8946-8957.

Ng, K. T.; Hercules, D. M., *J. Phys. Chem*. **1976,** *80*, 2094-2102.

Nørskov, J. K.; Bligaard, T.; Logadottir, A.; Kitchin, J. R.; Chen, J. G.; Pandelov, S.; Stimming, U. *J. Electrochem. Soc*. **2005,** *152*, J23-J26.

Oh, A.; Sa, Y. J.; Hwang, H.; Baik, H.; Kim, J.; Kim, B.; Joo, S. H.; Lee, K. *Nanoscale* **2016,** *8*, 16379-16386.

Ouyang, C.; Wang, X.; Wang, C.; Zhang, X.; Wu, J.; Ma, Z.; Dou, S.; Wang, S. *Electrochim. Acta* **2015,** *174*, 297-301.

Parsons, R. *Trans. Faraday Soc*. **1958,** *54*, 1053-1063.

Peng, Z.; Jia, D.; Al-Enizi, A. M.; Elzatahry, A. A.; Zheng, G. *Adv. Energy Mater*. **2015,** *5*, 1402031.

Perdew, J. P.; Burke, K.; Ernzerhof, M. *Phys. Rev. Lett*. **1996,** *77*, 3865-3868.

Petersen, M. A.; van den Berg, J.-A.; Ciobîcă, I. M.; van Helden, P. *ACS Catal*. **2017**, *7*, 1984-1992.

Ping, Y.; Nielsen, R. J.; Goddard, W. A. *J. Am. Chem. Soc*. **2017,** *139*, 149-155.

Qi, J.; Zhang, W.; Xiang, R.; Liu, K.; Wang, H.-Y.; Chen, M.; Han, Y.; Cao, R. *Adv*. *Sci*. **2015,** *2*, 1500199.

Reier, T.; Pawolek, Z.; Cherevko, S.; Bruns, M.; Jones, T.; Teschner, D.; Selve, S.; Bergmann, A.; Nong, H. N.; Schlögl, R.; Mayrhofer, K. J. J.; Strasser, P. *J. Am*. *Chem*. *Soc*. **2015**, *137*, 13031-13040.

Rohrbach, A.; Hafner, J.; Kresse, G. *Phys*. *Rev*. *B* **2004,** *69*, 075413.

Romanyuk, O.; Varga, M.; Tulic, S.; Izak, T.; Jiricek, P.; Kromka, A.; Skakalova, V.; Rezek, B. *J*. *Phys*. *Chem*. *C* **2018,** *122*, 6629-6636.

Sagu, J. S.; Mehta, D.; Wijayantha, K. G. U. *Electrochem*. *Commun*. **2018,** *87*, 1-4.

Sasi, B.; Gopchandran, K. G. *Nanotechnology* **2007,** *18*, 115613.

Shalom, M.; Ressnig, D.; Yang, X.; Clavel, G.; Fellinger, T. P.; Antonietti, M. *J*. *Mater*. *Chem*. *A* **2015,** *3*, 8171-8177.

Sheng, W.; Gasteiger, H. A.; Shao-Horn, Y. *J*. *Electrochem*. *Soc*. **2010,** *157*, B1529-B1536.

Shinagawa, T.; Garcia-Esparza, A. T.; Takanabe, K. *Sci*. *Rep*. **2015,** *5*, 13801.

Silva, R.; Voiry, D.; Chhowalla, M.; Asefa, T., *J*. *Am*. *Chem*. *Soci*. **2013,** *135*, 7823-7826.

Smith, R. D. L.; Prévot, M. S.; Fagan, R. D.; Zhang, Z.; Sedach, P. A.; Siu, M. K. J.; Trudel, S.; Berlinguette, C. P. *Science* **2013**, *340*, 60-63.

Song, F.; Hu, X. *Nat*. *Commun*. **2014**, *5*, 4477.

Stamenkovic V. R.; Strmcnik D.; Lopes P. P.; Markovic N. M. *Nat*. *Mater*. **2016,** *16*, 57-69.

Stevens, M. B.; Enman, L. J.; Batchellor, A. S.; Cosby, M. R.; Vise, A. E.; Trang, C. D. M.; Boettcher, S. W. *Chem*. *Mater*. **2017,** *29*, 120-140.

Suen, N.-T.; Hung, S.-F.; Quan, Q.; Zhang, N.; Xu, Y.-J.; Chen, H. M. *Chem*. *Soc*. *Rev*. **2017,** *46*, 337-365.

Sugiyama, I.; Shibata, N.; Wang, Z.; Kobayashi, S.; Yamamoto, T.; Ikuhara, Y. *Nat*. *Nanotechnol*. **2013,** *8*, 266.

Svanantham, A.; Ganesan, P.; Shanmugam, S. *Adv*. *Funct*. *Mater*. **2016,** *26*, 4661-4672.

Swierk, J. R.; Klaus, S.; Trotochaud, L.; Bell, A. T.; Tilley, T. D. *J*. *Phys*. *Chem*. *C* **2015**, *119*, 19022-19029.

Tahir, M.; Pan, L.; Idrees, F.; Zhang, X.; Wang, L.; Zou, J.-J.; Wang, Z. L. *Nano Energy* **2017,** *37*, 136-157.

Tang, C.; Pu, Z.; Liu, Q.; Asiri, A. M.; Luo, Y.; Sun, X. *Int*. *J*. *Hydrogen Energy* **2015,** *40*, 4727-4732.

Tian, J.; Liu, Q.; Asiri, A. M.; Sun, X. *J*. *Am*. *Chem*. *Soc*. **2014,** *136*, 7587-7590.

Tomellini, M. *J*. *Chem*. *Soc., Faraday Trans*. *1* **1988,** *84*, 3501-3510.

Trout, B. L.; Parrinello, M. *J*. *Phys*. *Chem*. *B* **1999,** *103*, 7340-7345.

Urquhart, S. G.; Ade, H. *J*. *Phys*. *Chem*. *B* **2002,** *106*, 8531-8538.

Voiry, D.; Chhowalla, M.; Gogotsi, Y.; Kotov, N. A.; Li, Y.; Penner, R. M.; Schaak, R. E.;

Wang, H.; Kong, D.; Johanes, P.; Cha, J. J.; Zheng, G.; Yan, K.; Liu, N.; Cui, Y. *Nano Lett*. **2013,** *13*, 3426-3433.

Wang, J.; Xu, F.; Jin, H.; Chen, Y.; Wang, Y. *Adv*. *Mater*. **2017,** *29*, 1605838.

Wang, J.; Mao, S.; Liu, Z.; Wei, Z.; Wang, H.; Chen, Y.; Wang, Y. *ACS Appl. Mater. Interfaces* **2017,** *9*, 7139-7147.

Wang, A.-L.; Xu, H.; Li, G.-R. *ACS Energy Lett*. **2016**, *1*, 445-453.

Weiss, P. S. *ACS Nano* **2018**, *12*, 9635-9638.

Weng, B.; Xu, F.; Wang, C.; Meng, W.; Grice, C. R.; Yan, Y. *Energy Environ. Sci*. **2017**, *10*, 121-128.

Winchester, N.; Reilly, J. M. *Energy Econ.* **2015,** *51*, 188-203.

Wu, Y.; Liu, X.; Han, D.; Song, X.; Shi, L.; Song, Y.; Niu, S.; Xie, Y.; Cai, J.; Wu, S.; Kang, J.; Zhou, J.; Chen, Z.; Zheng, X.; Xiao, X.; Wang, G. *Nat. Commun*. **2018,** *9*, 1425.

Wu, Y.; Liu, Y.; Li, G.-D.; Zou, X.; Lian, X.; Wang, D.; Sun, L.; Asefa, T.; Zou, X. *Nano Energy* **2017,** *35*, 161-170.

Wu, Y.; Li, G.-D.; Liu, Y.; Yang, L.; Lian, X.; Asefa, T.; Zou, X. *Adv. Funct. Mater*. **2016,** *26*, 4839-4847.

Wu, H. B.; Xia, B. Y.; Yu, L.; Yu, X.-Y.; Lou, X. W. *Nat. Commun*. **2015,** *6*, 6512.

Xiao, P.; Chen, W.; Wang, X. *Adv. Energy Mater*. **2015,** *5*, 1500985.

Xie, J.; Zhang, H.; Li, S.; Wang, R.; Sun, X.; Zhou, M.; Zhou, J.; Lou, X. W.; Xie, Y. *Adv. Mat*. **2013,** *25*, 5807-5813.

Xing, Z.; Li, Q.; Wang, D.; Yang, X.; Sun, X. *Electrochim. Acta* **2016,** *191*, 841-845.

Yan, M.; Pan, X.; Wang, P.; Chen, F.; He, L.; Jiang, G.; Wang, J.; Liu, J. Z.; Xu, X.; Liao, X.; Yang, J.; Mai, L. *Nano Lett*. **2017,** *17*, 4109-4115.

Yan, X.; Tian, L.; Chen, X. *J. Power Sources* **2015,** *300*, 336-343.

Yan, B.; Krishnamurthy, D.; Hendon, C. H.; Deshpande, S.; Surendranath, Y.; Viswanathan, V. *Joule 1*, 600-612.

Yang, W.; Cheng, G.; Dong, C.; Bai, Q.; Chen, X.; Peng, Z.; Zhang, Z. *J. Mater. Chem. A* **2014,** *2*, 20022-20029.

Yeo, B. S.; Bell, A. T. *J. Phys. Chem. C* **2012,** *116*, 8394-8400.

Yu, M.; Trinkle, D. R. *J. Chem. Phys.* **2011,** *134*, 064111.

Yu, M.; Zhao, S.; Feng, H.; Hu, L.; Zhang, X.; Zeng, Y.; Tong, Y.; Lu, X. *ACS Energy Lett.* **2017**, *2*, 1862-1868.

Zaffran, J.; Toroker, M. C. *ChemistrySelect* **2016,** *1*, 911-916.

Zaffran, J.; Nagli, M.; Shehadeh, M.; Toroker, M. C. *Theor. Chem. Acc.* **2018,** *137*, 3.

Zeng, K.; Zhang, D. *Prog. Energy. Combust. Sci.* **2010,** *36*, 307-326.

Zeng, M.; Li, Y. *J.Mater. Chem. A* **2015,** *3*, 14942-14962.

Zhao, W.; Bajdich, M.; Carey, S.; Vojvodic, A.; Nørskov, J. K.; Campbell, C. T. *ACS Catal.* **2016,** *6*, 7377-7384.

Zhang, T.; Wu, M.-Y.; Yan, D.-Y.; Mao, J.; Liu, H.; Hu, W.-B.; Du, X.-W.; Ling, T.; Qiao, S.-Z. *Nano Energy* **2018,** *43*, 103-109.

Zhang, W.-B.; Tang, B.-Y. *J. Chem. Phys.* **2008,** *128*, 124703.

Zhang, J. Y.; Li, W. W.; Hoye, R. L. Z.; MacManus-Driscoll, J. L.; Budde, M.; Bierwagen, O.; Wang, L.; Du, Y.; Wahila, M. J.; Piper, L. F. J.; Lee, T. L.; Edwards, H. J.; Dhanak, V. R.; Zhang, K. H. L. *J. Mater. Chem. C* **2018,** *6*, 2275-2282.

Zhang, J.; Wang, Y.; Zhang, C.; Gao, H.; Lv, L.; Han, L.; Zhang, Z. *ACS Sustain. Chem. Eng.* **2018**, *6*, 2231-2239.

Zhang, W.; Lai, W.; Cao, R. *Chem. Rev.* **2017,** *117*, 3717-3797.

Zheng, Y.; Jiao, Y.; Jaroniec, M.; Qiao, S. Z. *Angew*. *Chem*. *Int*. *Ed*. **2015,** *54*, 52-65.

Zhu, J.; Li, Y.; Kang, S.; Wei, X.-L.; Shen, P. K. *J*. *Mater*. *Chem*. *A* **2014,** *2*, 3142-3147.

Zhu, K.; Liu, H.; Li, M.; Li, X.; Wang, J.; Zhu, X.; Yang, W. *J*. *Mater*. *Chem*. *A* **2017**, *5*, 7753-7758.

Zhu, X.; Tang, C.; Wang, H.-F.; Zhang, Q.; Yang, C.; Wei, F. *J*. *Mater*. *Chem*. *A* **2015**, *3*, 24540-24546.

Zhou, D.; Xiong, X.; Cai, Z.; Han, N.; Jia, Y.; Xie, Q.; Duan, X.; Xie, T.; Zheng, X.; Sun, X.; Duan, X. *Small Methods* **2018**, *2*, 1800083.

Zou, X.; Zhang, Y. *Chem. Soc. Rev.* **2015,** *44*, 5148-5180.

Zou, X.; Liu, Y.; Li, G.-D.; Wu, Y.; Liu, D.-P.; Li, W.; Li, H.-W.; Wang, D.; Zhang, Y.; Zou, X. *Adv. Mater.* **2017**, *29*, 1700404.

Zou, X.; Sun, Q.; Zhang, Y.; Li, G.-D.; Liu, Y.; Wu, Y.; Yang, L.; Zou, X. *Sci*. *Rep*. **2018**, *8*, 4478.